TÉCNICO LISBOA

Millimeter Wave Antenna Implementation in Smartphones for 5G Communications

Filipa Santana da Silva Fernandes

Thesis to obtain the Master of Science Degree in

Electrical and Computer Engineering

Supervisors:

Prof. António José Castelo Branco Rodrigues
Doctor Christian Rom

Examination Comittee

Chairperson:José Eduardo Charters Ribeiro da Cunha Sanguino
Supervisor: Prof. António José Castelo Branco Rodrigues
Members of the Comitee: Prof. António Manuel Restani Graça Alves Moreira

November 2018

Declaration

I declare that this document is an original work of my own authorship and that it fulfills all the requirements of the Code of Conduct and Good Practices of the Universidade de Lisboa.

Acknowledgements

Finally, my year - long journey at Intel Mobile Communications is now coming to an end and I would like to use this space to dedicate some words to everyone who made this into a wonderful experience.

First of all, I would like to thank Instituto de Telecomunicações. Also, a special word of gratitude goes out to my supervisors, Professor António Rodrigues and Professor Paula Queluz, without whom I wouldn't have had the opportunity to do this internship abroad, for the guidance and patience.

I would also like to thank everyone at Intel Aalborg for the support, hospitality and for helping me see Denmark as a home away from home. Especially to Christian Rom, Simon Svendsen and Ole Jagielski, for sharing their ideas and encouraging me to be more confident and think outside the box.

To my friend and colleague Raquel, who took on this challenge with me, I would also like to say thank you for walking besides me through this year's snowy, rainy or sunny roads. Despite our clashing personalities, it wouldn't have been half as much fun without you!

And, of course, a huge thank you to my family, for always celebrating every little one of my achievements (I'm talking to you, Mom!) and for your relentless efforts of cheering me on during bad days, even when I didn't acknowledge you. A special thank you to my father, a very silent rooter whose actions speak volumes. I will forever be grateful for the confidence you have in me and for the trails you've been leaving that led me to where I am today and, hopefully, will take me closer to where you are tomorrow.

Finally, my most sincere gratitude goes out to João, not only for being my biggest supporter but also for burning through so many data plans in hopes that video chats would shorten the 2467 km between the two of us. Thank you for giving me room to grow and for always reminding me of what really matters. I'm thankful that I was able to share seven years of my biggest victories and failures with you and I hope many more will come for us to celebrate or learn from together.

Abstract

5G is a wireless technology being currently developed to sustain the high amounts of data rate, connections, and bandwidth with low latency that come with more users, devices, and ambitious endeavors such as Smart Cities or Autonomous Vehicles. 5G will introduce a paradigm shift in the mobile phone industry regarding antenna design and implementation.

This dissertation's goal is to assess how to implement millimeter wave antennas in 5G smartphones to minimize impairments caused by high frequencies, modern mobile phone form factor constrictions and dynamic environment characteristics.

A comparison process is established using two mm-Wave antenna families to evaluate their potential and limitations when integrated into 5G smartphones: patches (PBS) and monopoles (MBS).

It involves two stages: firstly, a coverage study, to assess how well distributed in space is the power radiated by the antenna array; and secondly, a discrete geometrical MIMO channel simulator is developed to recreate the mm-Wave propagation conditions in any scenario (from rural to urban), including the effects of the real antennas, smartphone metallic chassis and user influence (body blockage and depolarization). This allows to evaluate the MIMO channel performance depending on the antenna type, polarization, scenario, and body blockage.

The study shows that very simple antennas can be used in the user terminal to cope with the challenges of mm-Wave 5G. Monopole Based Solution (MBS) antennas are perfect candidates because of their compactness, low complexity and low cost when compared to PBS.

Key-words: small antennas, 5G, MIMO, Beamforming, mm-Wave, Smartphones.

Resumo

5G é a mais recente tecnologia sem fios desenvolvida para suportar valores elevados de tráfego, de conexões e de largura de banda com baixa latência, resultantes de um aumento de utilizadores, dispositivos e iniciativas como Cidades Inteligentes ou Veículos Autónomos. 5G introduzirá uma mudança de conceitos na indústria dos telemóveis no que toca ao design e implementação de antenas.

O objectivo desta dissertação é estudar como implementar antenas milimétricas em telemóveis 5G para minimizar imparidades causadas por frequências altas, constrições de design dos telemóveis e condicões dinâmicas de ambiente.

Um processo de comparação é estabelecido usando duas famílias de antenas milimétricas para avaliar o seu potencial e limitações quando integradas em smartphones 5G: *patches* (PBS) e monopolos (MBS). Este é feito em duas fases: um estudo de cobertura que determina quão bem distribuída no espaço está a potência radiada pelas antenas, e, finalmente, um simulador de canal MIMO discreto geométrico é desenvolvido para recriar as condições de propagação de frequências milimétricas, em qualquer cenário (rural a urbano), incluindo efeitos de antenas reais, o chassis do telemóvel e o utlizador (bloqueio corporal e despolarização). Isto permite avaliar o desempenho do canal MIMO dependendo do tipo de antena, polarização, cenário e bloqueio corporal.

O estudo demonstra que antenas simples podem ser usadas no terminal do utilizador para gerir os desafios de ondas milimétricas 5G. As antenas MBS são candidatas perfeitas por serem soluções compactas, de baixa complexidade e de baixo custo em comparação com as PBS.

Palavras-chave: Antenas miniaturizadas, 5G, MIMO, *Beamforming*, Ondas milimétricas, *Smartphones*.

Contents

List of Figures

List of Tables

Acronym List

3D	three - dimensional
3G	third generation
3GPP	Third Generation Partnership Project
4G	fourth generation
5G	fifth generation
APA TBX	Antenna Pattern Analysis Toolbox
ASCII	American Standard Code for Information Interchange
BF	beamforming
BM	Browsing Mode
BS	Base Station
CAD	Computer-Aided Designs
CDF	Cumulative Distribution Function
CN	Condition Number
CS	Coverage Study
eMBB	enhanced Mobile Broadband
GCS	Global Coordinate System
GSM	Global System for Mobile Communications
GUI	Graphic User Interface
HD	High Definition
IEEE	Institute of Electrical and Electronics Engineers
IoT	Internet of Things
ITU	Internation Telecommunication Union
LCS	Local Coordinate System
LOS	Line-of-Sight
LTE	Long-Term Evolution
MBS	Monopole Based Solution
MIMO	Multiple input - Multiple output
mMTC	massive Machine Type Communications
mm-Wave	millimeter Wave
MP	Multipath
MU-MIMO	Multi-User MIMO
NLOS	No Line-of-Sight
PBS	Patch Based Solution

RAN	Radio Access Network
SA	Services and Systems Aspects
SE	Spectral Efficiency
SISO	Single-Input-Single-Output
SM	Spatial Multiplexing
SMIFA	Self-Matched Indirect Fed Array
SNR	Signal-to-Noise Ratio
SU-MIMO	Single User MIMO
SVD	Single Value Decomposition
TM	Talking Mode
UE	User Equipment
URRLC	(Ultra-Reliable and Low Latency Communications
USA	United States of America
VNI	Visual Network Index
WCS	Working Coordinate System
WiGig	Wireless Gigabit Alliance

Chapter 1

Introduction

1.1 Motivation

In recent years, wireless technology has experienced a fast growth curve and opened the way for new and creative applications that allow anyone to connect simultaneously with thousands of people across the globe (High Definition (HD) streaming), read emails or check vital signs on a smart watch (wearables), or even have an immersive experience in a tropical destination without leaving the couch (Virtual Reality). However, there is also an unavoidable drawback from this kind of progress: the copious amounts of data rate, number of connections and bandwidth that are required to make all of this possible put a serious strain on the current fourth generation (4G) wireless network, which soon might not be able to sustain the demanding user standards of Quality of Service and Experience [1]. Therefore, fifth generation (5G), the new generation of wireless systems, is currently being developed to manage this growth in data traffic that inevitably comes with more users, devices, higher data rates and ambitious endeavors such as Smart Cities or Autonomous Vehicles [2].

The development of the technology to support this innovative, but ambitious, generation of wireless systems is sparking a major paradigm shift in the mobile phone industry, especially for the antenna design and implementation. There are several challenges that must be tackled before 5G antenna technology is implementable in smartphones. In order to comply with capacity and bandwidth requirements, the only option is to produce 5G smartphone cellular antennas in the millimeter Wave (mm-Wave) band. These high frequencies provide unprecedented data rate values and better spectral efficiency but, unfortunately, they also lead to massive power losses.

Considering this new frequency spectrum territory, there are a few more design parameters that must be taken into account. Some of them include the effect of the smartphone's metallic case and the users' body blockage, both ruining the mm-Wave antennas' beamforming (BF) ability. Moreover, the user's placement of the phone also needs to be considered. According to the orientation of the phone relative to the Base Station (BS), the antennas may lose their polarization alignment with the BS, greatly affecting the Multiple input - Multiple output (MIMO) performance of the antennas, which is an indispensable functionality for 5G.

There are a lot of design parameters that are being neglected (or not properly assessed) in the currently available literature regarding mm-Wave antenna implementation in smartphones.

Therefore, this thesis aims at studying them all and proposing a method for quantifying them in accordance to 5G standards of quality. Ultimately, this process should be used to compare different types of mm-Wave antennas and evaluate which one of them better fits a particular smartphone's form factor when it comes to coverage gain and MIMO channel performance.

In order to do so, two types of antenna families are considered for testing at 39 GHz. These are a patch based solution, PBS, and a monopole based solution, MBS. The PBS is a very popular solution in current literature. Its low profile, and high gain values when used in an array configuration suggest that the PBS antenna is a good candidate for 5G smartphone implementation, not to mention its dual polarization ability. In theory, an array with two different polarizations can transmit simultaneously two data streams and double the spectral efficiency.

However, the design difficulties mentioned above might make the prediction of the antenna's radiation pattern very challenging for mm-Wave. The ideal narrow beams obtained in free space for MIMO and BF might lose their shape when realistic environment conditions come into play. If realistic radiation pattern prediction is not a reliable option, then basing an antenna's design in achieving a specific beam behavior will be a vain effort. Instead of focusing solely on gain, an alternative would be turning to average coverage and opting for an antenna that is able to radiate power in more directions, such as a MBS solution. In order to test this hypothesis, a monopole based solution was developed at Intel Aalborg, called Self-Matched Indirect Fed Array (SMIFA) [3]. If properly positioned, it has a radiation pattern wider than the patch, despite having a small difference in gain that fades away when the phone's chassis influence is considered. The SMIFA has a larger bandwidth than a standard patch, as well as a smaller size, cheaper predicted production cost and easier implementation in smartphones. It can be used in larger arrays without interfering much with sub-6 GHz legacy antennas. Table 1.1 summarizes the pros and cons between the two:

Table 1.1: Patch antenna solution vs. Monopole based solution.

	Patch	Monopole
Maximum Gain	X	
Radiation Beamwidth		X
Dual Polarization	X	
Impedance Bandwidth		X
Size		X
Design Complexity		X
Implementation within the phone		X
Cost		X

This table shows that the monopole antenna appears to be a strong contender for smartphone implementation and, consequently, worth investigating. However these are two different types of antennas and comparing them fairly is an arduous task that should be approached carefully.

This dissertation was developed under Intel Mobile Communications, in the form of an Internship on RF and signal processing in the ICDG RFSS Innovation site in Aalborg, Denmark.

1.2 Goals

This thesis sets out to identify the main challenges for mm-Wave wave antenna implementation in modern smartphones that will be used for 5G communications. The project's research question can be presented as: "How to implement mm-Wave antennas in 5G smartphones in order to minimize propagation adversities caused by high frequencies, modern smartphone form factor constrictions and dynamic environment conditions imposed by the mobile phone?".

In order to do so, two antenna families at 39 GHz, PBS and MBS, are used to establish a fair mm-Wave antenna comparison model. With that in mind, this project can be broken down into four fronts, displayed in Figure 1.1. They are: Antenna selection and design in free space, a sudy regarding Influencing factors on the antenna's behavior, a Coverage Study (CS) development and a MIMO performance study by creating a MIMO channel simulator. Naturally, each of these fronts can be subdivided into numerous but equally important tasks, listed below, that will add up to develop the comparison model for mm-Wave antennas in smartphones proposed in this thesis.

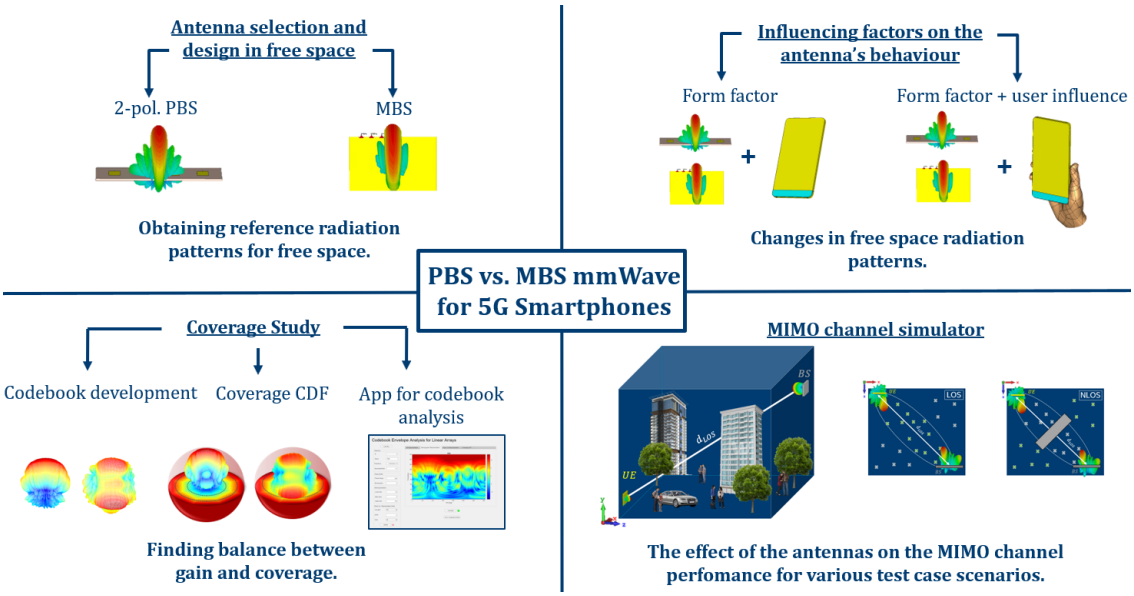

Figure 1.1: Project's main fronts

Antenna selection and design in free space: Firstly, in a free space context, PBS and MBS must be recreated into a simulation environment in order to create the test simulations. This will require:

- Design and optimization of the PBS and MBS models in CST to be used as the project's main antenna solutions.
- Simulation of the PBS and MBS in free space to obtain the reference radiation patterns.

Influencing factors on the antenna's behavior: Since free space is not a realistic scenario for smartphones, it is crucial to determine what are most influential factors to the antennas' radiation pattern and overall performance. That includes not only the phone components but also the user. To do that:

- PBS / MBS array implementation in the smartphone's form factor in CST.

- Addition of different mobile phone components that might potentially affect the antennas' performance (plastic cover, glass screen, change in bezel size).
- Include a hand grip to recreate the user's body blockage influence.
- Use the simulation results to compare with the free space ones in order to assess each element's influence on the antennas' behavior.

CS: If the antennas do not provide enough gain the antenna can not transmit the signal for too big distances. However if the gain is very high, the antenna beam is very narrow and will fail to cover some areas in space. A balance between the two sides of the scale must be obtain for optimal communications. A tool can be created for this, using the information gathered from previous steps:

- Use the data extracted from the CST simulations to create a table of predefined weights for each antenna in order to obtain a certain beam orientation and shape (automatic codebook generation process).
- Use these weights to compute a set of beams that accurately describe the range of the antenna's coverage area (to compare PBS with MBS).
- Create a function that uses the set of beams to quantify each antenna type's percentage of space covered by radiated power, while maintaining an acceptable gain value of choice.
- Develop an app that includes all these functionalities into one toolbox.

MIMO channel simulator: Before advancing to real tests, it is vital to have a model that accurately describes the behavior of the antennas and the environment, to have a reference when performing real life measurements, and to develop critical thought. The existing simulators are lacking a bit in realism. Therefore, a tool is created in this thesis to simulate any type of realistic environment conditions for evaluation of MIMO channel performance for any mm-Wave antenna. It should:

- Account for the antenna's characteristics (real radiation pattern accounting for the phone and the user's influence, coupling, antenna polarization).
- Implement the functionality of managing the amount of obstacles to recreate a range of environments from rural to dense urban regions.
- Make the environment change throughout the time of analysis.
- Enable any relative orientation of the phone relative to the BS.
- Include phone rotation.
- Develop a beam tracking algorithm.
- Calculate channel metrics to assess the MIMO quality (Condition Number (CN)), signal strength (SNR) and the overall channel performance (channel capacity).
- Create a function that describes how sensitive the channel performance is to the phone's rotation in space for each antenna type.

1.3 Context in the industry and literature review

For some years now, 5G has been the center of discussion of experts and there are many expectations from the public. This new generation of wireless systems is being brought up globally, with people from all around the world contributing to the common goal of making 5G a tangible reality. In order to make this an internationally applicable technology, a general entity is required to define standards for 5G communications. The entity responsible, Third Generation Partnership Project (3GPP), is a group collaboration of global bodies of telecommunications standards. 3GPP was first created to develop a third generation (3G) mobile phone system specification from Global System for Mobile Communications (GSM), within the scope of the International Telecommunication Union's (ITU) project, International Mobile Telecommunications-2000. Nowadays, it is responsible for setting specifications for Radio Access Network (RAN), Services and Systems Aspects (SA), and Core Network & Terminals (CT) for all generations of wireless systems. Some of their standards for 5G that have been released recently include:

- Number of connections - Nowadays, every mobile device is connected to the network. Further to the traditionally connected devices like the laptop or smartphone, a wristwatch with Internet connection, a health monitoring gadget to wear during a workout, a tracking device on a mailing package or a sensor to determine the quality of soil for farming - they all gather information and send it via the network. In order to keep up with this ever growing number of connections, using new multiplexing and coding schemes, 5G will be able to provide 100 times more connections than Long-Term Evolution (LTE) previously had available [4].
- Latency - The delay felt during a communication over the network, is a very important factor in new services such as self-driven cars or remote surgery performance. These services are time critical and not meeting the latency requirements can lead to disastrous consequences. Such small delay values are not attainable with the current 4G network, hence 5G is currently aiming for latency over air links as low as 1 ms (10 ms for device to core communications) [5].
- Capacity - Because of the exponentially larger number of users and devices, 5G system capacity is predicted to increase up to three orders of magnitude compared to LTE's (1 Tbps per km^2), by making use of strategies such as higher frequency bands, BF and massive MIMO technology [4].
- Energy Consumption - With all the developments mentioned above, it is expected that the energy-per-bit usage for 5G should be reduced by a factor of 1,000 in order to balance the increase in offer of per-link data rates [6], [7].

Although these numbers are astonishing, they should be taken as a limit reference of what the new network will be able to withstand and not as a reflection of the user's average experience in every case scenario. The 5G network is envisioned to support mobile services and applications with different performance requirements. It will be an adaptable system that accommodates efficiently each service specification (latency, peak throughput values, number of always-on users etc.), performing an intelligent resource allocation - Network slicing [7]. For example, smart sensors or text-based messaging have more relaxed latency requirements than a self-driven car in the same way that cloud storage can be performed through lower throughput values than virtual reality videos can, since they need to obtain a clear enough picture to trick the human eye.

Besides achieving system flexibility and intelligence, while maintaining an integrative approach towards previous technologies, one of the major challenges in 5G system design is optimizing spectral efficiency. Currently, there are multiple strategies in place to deal with this issue such as:

- Spectrum regulation - For 5G, the growing traffic demands led to a revision of spectrum regulation. It is essential for a 5G system to be able to use efficiently all the available spectrum, being it licensed, unlicensed, high or low band. As a result, the internationally appointed 5G spectrum is widely spread, making use of lower frequencies (low bands below 1 GHz) for long range, wide coverage communications and massive Internet of Things (IoT), mid bands (between 1 and 6 GHz) for enhanced mobile broadband and compromise between coverage and capacity, and high bands (above 24 GHz) for extreme bandwidth values [8], [9], [10]. Table 1.2 displays all frequency bands that ITU assigned for 5G.

Table 1.2: Frequency bands assigned to USA, Europe, China and South Korea as of December 2017

Countries	$<$ 1 GHz	1 GHz to 6 GHz	24 GHz to 71 GHz
USA	600 MHz	2.5 GHz 3.55 - 3.7 GHz 3.7 - 4.2 GHz 5.9 - 7.1 GHz	37 - 37.6 GHz 37.6 - 40 GHz 47.2 - 48.2 GHz 64 - 71 GHz
Europe	700 MHz	3.4 - 3.8 GHz 5.9 - 6.4 GHz	37 - 37.6 GHz 37.6 - 40 GHz 64 - 71 GHz
China	-	4.8 - 5 GHz	24.5 - 27.5 GHz 37.5 - 42.5 GHz
South Korea	-	3.4 - 3.7 GHz	26.5 - 29.5 GHz

  Frequencies above 24 GHz, like the ones mentioned above, belong to the mm-Wave spectrum and, therefore, offer large bandwidth, which is very appealing for large data transmissions. Unfortunately, its poor propagation conditions make it a difficult band to work with since, for such high frequencies, there is strong pathloss, environment absorption, and low penetration through objects, as well as little diffraction around obstacles. This means that a link could easily change from usable to unusable by simply turning a corner of a building. Because of this, for a long time, that part of the spectrum remained unexplored for new cellular technologies, merely being used for applications like secure short range communications and Line-of-Sight (LOS) satellite communications. However, nowadays, combining these frequencies with massive MIMO and BF methods makes the use of mm-Wave one of the pillars of 5G development [11].

- Massive MIMO - MIMO communications make use of multiple antennas in both the BS and the User Equipment (UE) end to improve robustness (Diversity) and/or capacity (Spatial Multiplexing (SM)) of a channel, utilizing scattering and reflections phenomena that before would constitute a nuisance for transmission [12], [13]. There are multiple variations of MIMO, like Multi-User MIMO (MU-MIMO) (when one or multiple antennas from several sets of devices are combined to communicate to each other) and Single User MIMO (SU-MIMO) (muti-antenna transmitter communicating with a multi antenna receiver). However, SU-MIMO is

always limited by the available space in the mobile device for antenna allocation. Massive MIMO comes as a solution to this problem. For massive MIMO, the number of antennas at the base station surpasses significantly the number of devices per signaling resource. This way, each BS can communicate with several users simultaneously within the same bandwidth, wich enhances immensely the spectral efficiency [14].

- BF - It is a signal processing technique that makes used of multiple antenna elements to form a shaped beam pattern tailored to the user's needs. It can be used both at the BS and UE ends to obtain high array gains that not only compensate for the high losses of mm-Wave but also increase signal-to-noise-ratio (SNR), while reducing channel interference [15]. It can also be used together with MIMO communications to further improve spectral efficiency [16].

The 5G network implementation must be able to support the three upcoming categories of 5G mobile network services defined by the International Telecommunications Union (ITU): enhanced Mobile Broadband (eMBB), massive Machine Type Communications (mMTC) and URLLC (Ultra-Reliable and Low Latency Communications). While eMBB encapsulates all services that require high bandwidth (high definition videos, virtual reality and augmented reality), mMTC offers support to IoT applications by focusing on high connection density like smart cities and smart agriculture. URLLC, on the other hand, caters to latency-dependent services, such as the previously mentioned self-driven cars and remote management [17]. Figure 1.2 shows a diagram based on [17] and [18] with some of the applications and services that these three domains support.

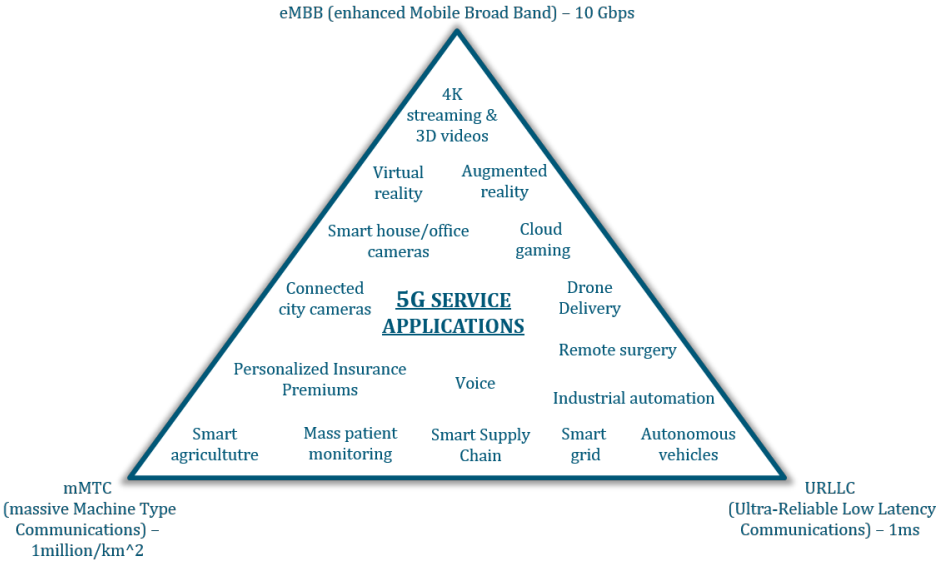

Figure 1.2: 5G three main areas of service: eMBB, mMTC and URLLC

It can not be helped but to notice that most of the 5G mobile services displayed in Figure 1.2 are housed or connected to devices such as tablets or smartphones. According to Cisco's annual visual network index (VNI), by 2021, smartphones and phablets will constitute over 50% of global devices and connections, being responsible for 86 % of global mobile data traffic [19]. It is clear, then, that mobile phones must be able to support this new technology, so that they can cater to the user's service demands. Implementing mm-Wave antennas into smartphones will allow for a

seamless transition of mobile communications to 5G. However, exploring smartphone performance enhancement to match 5G specifications entails a significant paradigm shift for the phone industry, specifically for antenna design and implementation.

The topic of 5G is still somewhat abstract when it comes to mm-Wave antenna technologies. Despite the existence of mm-Wave antennas in radio infrastructures being deployed in the near future, mm-Wave antenna technologies for 5G cellular handsets are still at their early stages. There is still no standardized method to design and implement these antennas in mobile phones due to the lack of knowledge on mm-Wave 5G wireless system benchmarks. This prevents the evaluation of the impact of design parameters such as user influence, handset effects, gain coverage and so on, since there is not a reference to compare to [20]. However, some the major challenges to the mm-Wave antenna design and implementation have been identified and in the literature there are several proposed approaches to mitigate them.

The first obstacle, which was already mentioned, is the drawback of using the mm-Wave band. The only way to counteract this is to use mm-Wave antennas in large arrays, so that the increased array gain can compensate for the huge losses. All proposed antenna solution available in the literature for mm-Wave frequencies are set in an array configuration, varying on the array size and type. In [21] a pair of patch arrays is placed on the top and bottom of the phone, each array containing 16 elements. Meanwhile [22] takes on a bolder approach, presenting 8 modules of patch arrays, each with 8 elements, distributed evenly throughout the length of the handset. This type of solution is only viable because mm-Wave frequencies lead to very small electrically sized antennas, that can fit into tight spaces such as the mobile phone. Otherwise, for the previous microwave frequencies in use, the spacing between antenna elements would be too big to be placed in a phone.

Another important topic for 5G, that also relates to the number of antenna elements present in the mobile phone, is the phone implementation of MIMO strategies. Nowadays, using MIMO in the mobile phone is not a novelty. The Samsung Galaxy S7, released on March 2016, already accommodated for 4x4 MIMO for SM. However, the introduction of mm-Wave frequencies allows for the mobile phone to accommodate more antennas. Therefore, the regular MIMO approach in the mobile phone can be subjected to a slight modification to what can be called hybrid MIMO. Hybrid MIMO is a combination of regular SM MIMO with BF [23], [15], [16]. This is only possible because of the high number of antennas in the smartphone that can be grouped into arrays, enabling BF. Naturally, SM and BF can be used separately but, for specific situations, they are stronger together.

For example, BF can be used to increase the SNR in situations were the power is limited, while at the same time making use of SM to transmit several independent data streams over the same carrier frequency, making for higher data rates. For example, in [22], the modules mentioned before are BF modules, meant to be used for transmitting 8 separate data streams. Also, when any of the modules is blocked, the modules can abandon the MIMO approach and can just be used as normal BF modules to transmit a single data stream. However, accommodating for a large number of antennas in a mobile phone is no easy task [24].

A quick look into the most popular mobile devices nowadays reveals one common problem that all smartphone companies face: lack of space for hardware in the wireless handset terminal [1]. These compact form factors, besides having to accommodate for other wireless technologies (and their antennas), need to integrate components such as battery, big screens, two (or even three)

cameras, fingerprint scanning, gyroscope, vibrator etc. to ensure that the user can enjoy the applications mentioned above in his smartphone. Therefore, it is challenging to fit the additional cellular antennas needed for 5G in the smartphone.

This issue originated a lot of articles suggesting compact and creative antenna solutions to optimize the space usage within the phone. An example is the use of dual polarized antennas. For cellular MIMO communications, the antennas, despite being very close to each other, cannot interfere with one another. In order to do so, the antennas should be orthogonal, to achieve maximum isolation. Using an array with dual polarization corresponds to using two arrays with orthogonal polarizations, which saves space while increasing the spectral efficiency, in theory [25]. In [23], two arrays are implemented in a phone with switchable polarization, reducing the number of arrays from four (two for MIMO with vertical polarization and two for MIMO horizontal polarization) to only two arrays with the same functionality. Some more ingenious ways of implementing mm-Wave antennas are also presented in [26], and [27], for example.

Another big trend in state of the art smartphones (and a big challenge for the antenna design team) the use of big display screens. This stems from the fact that people use their phones for a lot more purposes than just placing phone calls. Streaming, gaming, video-chatting are commodities that users expect to carry out comfortably in their mobile phones anywhere, anytime without straining their eyes. Most state of the art smartphones also have metallic casings. Not only do these serve an aesthetic purpose, but also provide structural sturdiness and heat dissipation. However, these design choices place another challenge for mm-Wave antenna placement, since bigger screens and metallic form factors will increase the amount of metal in proximity with the antennas. For these high frequencies, metal is responsible for the radiation pattern's dramatic loss of shape. Therefore it is vital to include the form factor in the antenna behavior studies.

Besides these design constrictions, another aspect of antenna design and placement is the user's influence in the antenna behavior, that manifests in two ways. On one hand, the human body, besides causing antenna impedance mismatch, behaves like a absorber and a reflector for mm-Wave, basically blocking any signal that comes in its direction. In [28] tests were made at 15 GHz to demonstrate the significant effects of body shadowing. The results are interpreted similarly to this thesis' CS and it shows that the body is a clear obstacle to signal propagation at 15 GHz. At 39 GHz these effects are even more pronounced [29]. Therefore, having a hand or a head held up against the phone will have major disturbances in the antennas radiation pattern. This is why having many antenna arrays in the phone is very important. If the user is blocking a certain antenna array with his hand the communications can still be carried out by the remaining array by performing beam switching and using a beam tracking algorithm.

On the other hand, it is hard to predict the relative orientation of the UE in relation to the BS. This can ruin the polarization alignment between the UE and the BS which will surely deteriorate the MIMO performance. Ultimately, this would render solutions such as the dual polarized antennas useless. Polarization alignment is pivotal for 5G communications.

Since this is a novel subject still under investigation, there are not too many articles in the literature that rigorously account for all these design and implementation requirements. Most likely, some get neglected for the sake of simplicity. For example, once again, in [22] the proposed solution seems to be a very interesting approach that appears to have some flaws in the verification process. Their solution is introduced as a way to prevent the antenna performance to get affected

by the user's hands. However, no test results were presented to prove such statement. Also, a single gain value was generalized for all the antennas in the modules, and this value was obtained from a reference which does not account for the form factor, antenna placement or hand grip chosen in the study.

The study performed in [20] fits most of the criteria listed so far. It touches all design subjects and proposes a type of dual polarized antenna for smartphones implementation. It is included in the paper a measurement set up to evaluate the MIMO performance of the link between the UE and a server. In this setup the UE is fixed and the server orientation is subjected to two changes. This rotation happens in the same plane, while still directed at the antenna arrays from the UE. This was meant to show to show that, with dual orthogonal polarization, the data rate of the channel is not as affected as it would be if it had only one polarization. Although these conclusions are correct, the study is a bit incomplete since it failed to include the results for other less favorable positions of the UE and the server. The range of motion of the server should extend to the three axis x, y and z. There are orientations that not even a dual polarization antenna might be able to salvage like, for example, if the server was rotated in 180^0, turning its back on the UE. Also, there is no mention to experiments performed at bigger distances than 2.5 meter, nor there is documented the effect of Multipath (MP), so there is no variation of the environment with time.

This stems from the fact that, for real life measurements for MIMO performance, there are some testing limitations. Often, not every test scenario can be carried out, either because it is too expensive, complex or because there is a lack of resources to conduct them all. Moreover, if the amount of real life test scenarios are limited, it is difficult to take any generalized conclusions out of it. However, the communication channel takes a big part in determining the MIMO system performance. Therefore, it is more significant to first establish an accurate and reliable channel model that recreates the environment and propagation features of mm-Wave, while incorporating all the antenna design parameters aforementioned [30]. The goal would be to use the same model to carry out any test scenario envisioned. A lot of measurements have been performed, such as in [31], to create these models, like [32], [33], [34]. However, these resort to some simplifications regarding antenna modeling and don't take some of the discussed design parameters into consideration such as the smartphone chassis or the user influence.

1.4 Thesis outline

This thesis is composed of five chapters. The first chapter is dedicated to the introduction of the dissertation's scope. This includes the motivations that fueled this thesis, as well as a review of the current state of the industry regarding the topic of implementation of mm-Wave antennas in 5G smartphones. The main challenges are listed and the current solutions and their frailties are also identified as further purpose for the thesis.

The second chapter describes the methodology developed to create a CS function and a configurable MIMO channel simulator for realistic MIMO channel performance evaluation, which are the thesis' two tools for comparing the PBS to the MBS fairly.

The results are divided between chapters three and four. Chapter three contains the results dedicated to the PBS and MBS antenna analysis. The antennas are evaluated as a single element and an array in free space. Also, it is studied their integration in the smartphone's form factor

and the hand grip influence. Lastly the CS is performed to identify the antenna type with the best coverage.

Chapter four, on the other hand, sustains all the results regarding the PBS and MBS within the form factor when introduced in a MIMO communication scenario (using the simulator developed). The MIMO channel performance criteria such as maximum channel data rate, SNR, CN and beam pair link are evaluated for several test scenarios where the UE is constantly rotating. This will lead to a cumulative study of channel performance that will show how much that antenna type is susceptible to phone rotation.

Finally, chapter five summarizes the project's conclusions on which antenna would be more indicated for smartphone implementation in this particular context and chapter six lays out the idealized future work.

Chapter 2

Methodologies

This Chapter describes the methodologies developed for this thesis, such as the design of simulation components in CST, the theory behind the antenna CS, codebook development (and the Graphic User Interface (GUI) that came out as a result of it) and the geometrical discrete MIMO channel simulator created to evaluate the antenna's influence on the quality of the MIMO channel.

As tools, this thesis relied mostly on the three - dimensional (3D) electromagnetic solver CST Microwave Studio [35] and Matlab for data processing. Lab measurements were not performed given the lack of time and resources but more on the topic will be further discussed in the Future Work section.

All the material developed in this chapter is illustrated with examples, but application of the methods for the final project goal will be presented and discussed in Chapters 3 and 4.

2.1 Simulation components

2.1.1 Smartphone form factor

Most popular mobile phones in the market nowadays have really small bezel size, so that the screen can take up most of the front of the phone, to maximize the quality of the user's experience. Also, the glass used for the phone's screen is very resistant, one example being the Gorilla Glass 5 produced by Corning [36], which is used in the Iphone X. Moreover, most phones nowadays have metal structures and either glass or plastic in the back, to allow for wireless charging.

The initial smartphone form factor available for simulation, represented in Figure 2.1, modeled a phablet developed by Intel, to which some changes were made to resemble nowadays' smartphones, such as the IphoneX and the Samsung S9. This model was mostly a compact structure made out of metal. The form factor had some hollow space in the bottom, where a dielectric was placed to accommodate the antennas. In Figure 2.1 this dielectric is not visible because the bottom area of the phone is encapsulated in a blue plastic casing.

This space was also partially occupied by the sub 6-GHz legacy antennas, as can be seen, in red boxes, in Figure 2.2 b). These legacy antennas were lumped with a 50 Ω impedance in the simulation model, so that their effect would still be accounted for without them being active (since the working frequency bandwidth is different). Although the size of this form factor was similar to

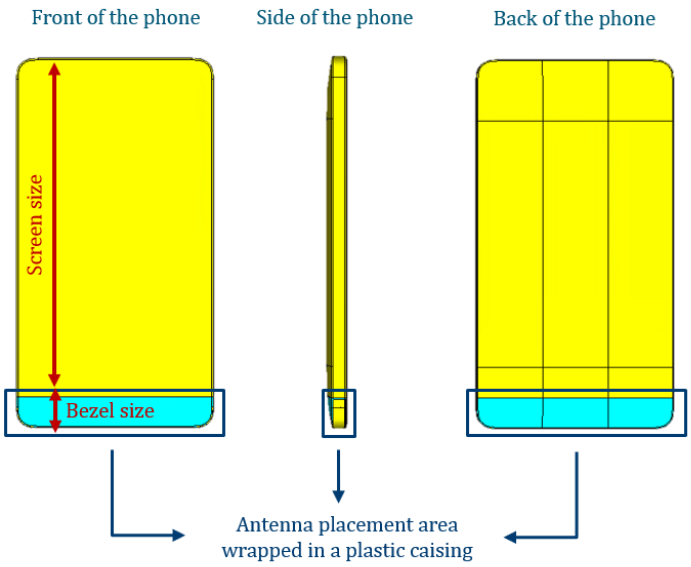

Figure 2.1: Intel's original form factor model for a phablet.

current smartphones' large dimensions, some alterations were made to the phone's bezel size and casing material in order to be used in the present thesis. The bezel size is the area of a display surrounding the screen. In Figure 2.1 the bezel size is marked just for the bottom of the phone. It corresponds to the area where there is no screen. If this bezel size decreases, the screen will be bigger, taking space away from the blue plastic casing and, therefore, the antenna placement space. Also, screen glass was added so that its influence in the antenna performance could be studied.

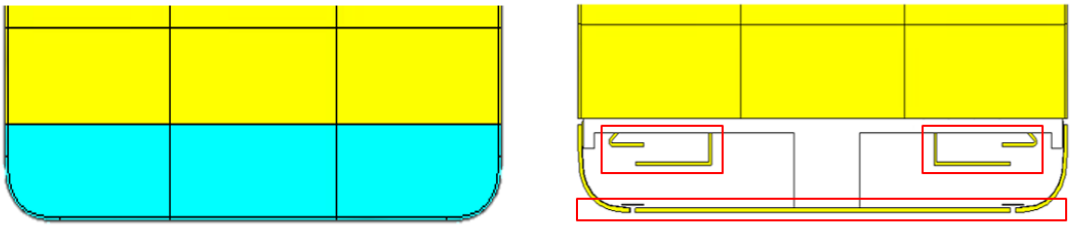

Figure 2.2: Bottom half of the back of the form factor; a) Antenna placement area with plastic casing; b) Sub-6 GHz legacy antenna integration in the antenna placement area.

2.1.2 Antenna design

One of the major factors in designing an antenna is radiation efficiency. It is usually defined as the ratio between the power delivered to the antenna port, P_{in} and the power that is actually radiated from the antenna, P_{rad}, and it is commonly designated as ϵ_R, as displayed in Equation 2.1.

$$\epsilon_R = \frac{P_{rad}}{P_{in}} \tag{2.1}$$

However, if the antenna impedance matching is not ideal, the term antenna's efficiency shifts to total efficiency, ϵ_T where the mismatch loss is also accounted for, as can be seen from Equation 2.2. The mismatch loss, M_L, dictates the quality of the impedance matching. Therefore, a low efficiency antenna either has a lot of its power absorbed as losses within the antenna, or reflected due to impedance mismatch.

$$\epsilon_T = \epsilon_R M_L \tag{2.2}$$

Regarding power absorption losses, because it is an intrinsic characteristic of the hardware, there is not much that can be done besides changing the material used (which can be expensive). However it is possible to mitigate the mismatch loss and achieve a M_L value as close to 1 as possible. In order to minimize the reflection in the antenna and maximize the power delivered to it, the antenna's impedance needs to match the transmission line's impedance. As a rule of thumb for 5G, the requirement is below -10 dB. In this project, instead of using circuitry, the impedance match was assured through manipulation of the antenna's electrical parameters, to simplify the model. Usually in mobile phone's the typical total efficiency values range from -7 to -1.5 dB.

2.1.2.1 Patch antenna (PBS)

. Figure 2.3 a) shows the patch model chosen to represent the patch antenna family, PBS. It is designed in CST to have the smallest possible dimension for the resonance frequency chosen for this study, 39 GHz. It is composed of a squared ground plane with a substrate on top, over which the patch is placed. It adopts a probe feeding approach in CST with discrete ports.

This is a dual polarized antenna - two feeding pins are placed orthogonally to provide a polarization along the y-axis and another along the x-axis, as can be seen from Figure 2.3 b). In theory, this intends to, ideally, double the channel's spectral efficiency (SE) when used in a MIMO system. The PBS antenna was used in a linear array configuration with four elements. The spacing between antenna elements, d, was determined not only by the radiation efficiency requirements but also by the requirement of providing a good isolation between adjacent elements. This imples that the transmission coefficient between the antennas,s_{ij}, is very small ($s_{ij} < -10$ dB). The PBS array was integrated in the bottom half of the phone's back, in the area reserved for antenna placement, as seen in Figure 2.5 a).

2.1.2.2 Monopole antenna (MBS)

Figure 2.4 a) illustrates the simplified version of the proposed monopole-type antenna solution, SMIFA, developed at Intel [3]. This model is a folded monopole, which is considerably smaller than the PBS, as seen in Figure 2.4 b). It is also used as a linear array with four antenna elements, with a big enough spacing, d, to reach low enough coupling levels between antenna elements ($s_{ij} < -10$ dB). Also tuned for 39 GHz and with a reflection factor lower than -10 dB, it was implemented in the bottom half of the phone's back, on top of the phone's dielectric, using the phone as a ground plane, as can be seen in Figure 2.5 b).

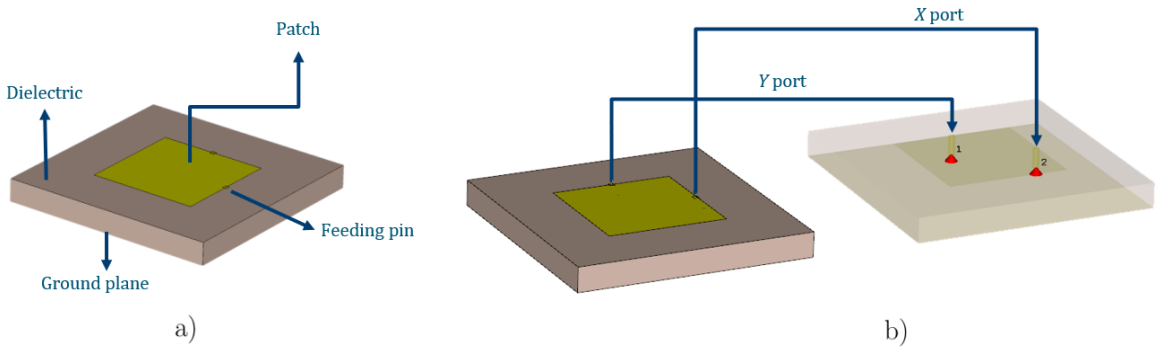

Figure 2.3: PBS antenna; a) Antenna structure; b) Antenna feeding method.

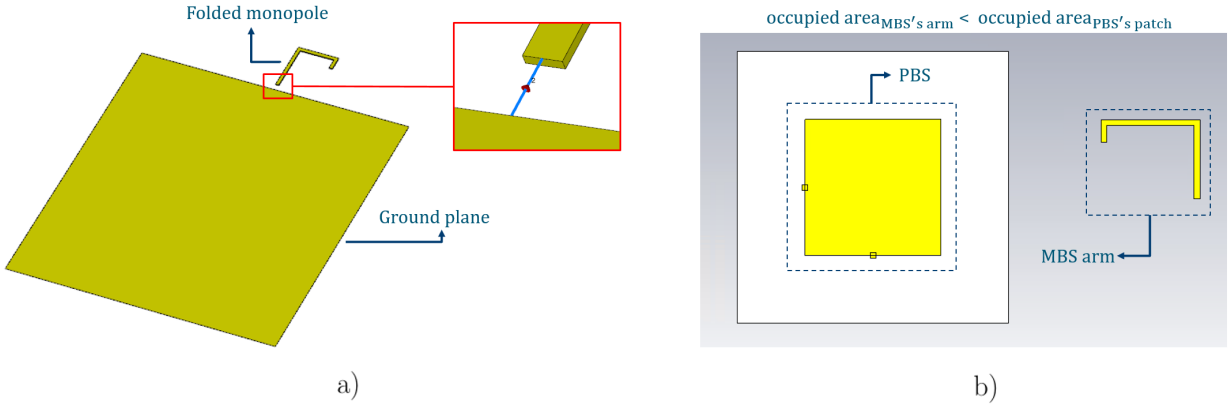

Figure 2.4: MBS antenna; a) Antenna structure; b) Size comparison between the patch and the monopole's arm.

The number of antenna elements for the linear array was not picked randomly. If the array dimension was too large, the beam would have high gain, since an array with N antenna elements has $G_{array} = G_{antenna} + 10\log(N)$. This leads to a very narrow beam shape, which is not able to cover a very large sector of space. However, if the N was too small, the array gain might not be capable of topping the propagations losses induced by mm-Wave. Besides that, the larger the N is, the larger is the phase shifter power consumption to steer the array beam. This would tend to reduce the smartphone's battery autonomy. A $N = 4$ linear array's size resulted from a compromise between securing gain and wide enough coverage.

2.1.3 User hand models

To model the user's body effect in the performance of mm-Wave antennas implemented in a mobile phone, it is necessary to pick a part of the user's body to recreate in a simulation context, in order for it to be included in the study. Therefore, the user's hand is chosen, which is a common pick, since it is always in direct contact with the phone when it is being used.

Along with the phablet model, Intel also provided a couple of 3D Computer-Aided Designs (CAD)

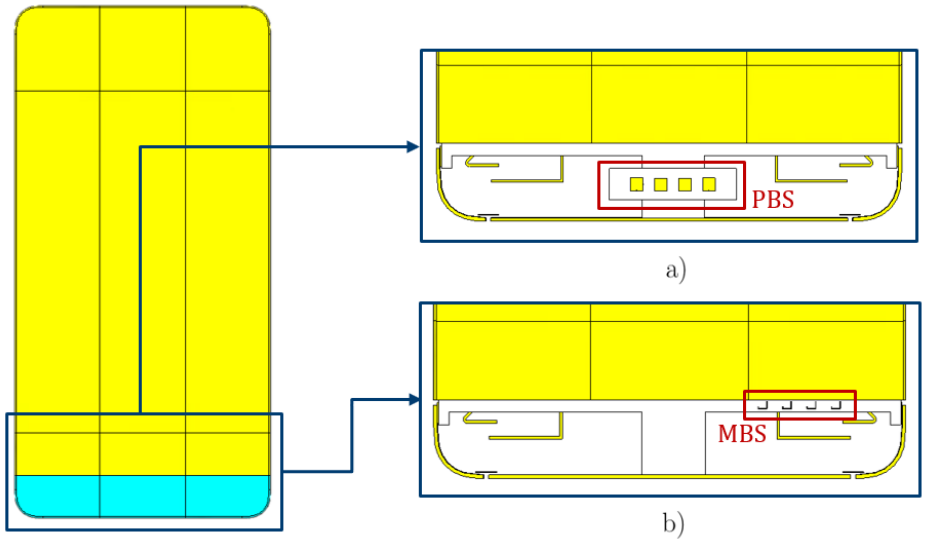

Figure 2.5: mm-Wave antenna placement in the form factor; a) PBS dual polarized array solution; b) MBS array solution.

of the hands, from older projects performed in the sub-6 GHz spectrum. These models can be integrated into the CST simulations and their grip posture is adjusted to the phablet's dimensions. Two of the most common grip postures were selected: Talk-mode (TM), seen in Figure 2.6 a), and Browsing Mode (BM), like in Figure 2.6 b). TM represents the position the user usually adopts when making a phone call, while BM mimics the way the user holds the phone when watching a video or playing a game, with the phone placed horizontally.

Originally, these CAD models were designed for sub-6 GHz frequencies. Therefore, their dielectric properties needed to be updated to mm-Wave frequencies. Although hands are an intricate part of the human body, with skin, bone, muscle and blood vessels, a simplification was made in the model to only include the muscle. The reasoning for this simplification lies on the fact that, from all the materials considered (muscle, bone and skin), the muscle had the biggest influence in the results. The muscle has the highest electrical conductivity out of all the hand components considered in [37] for 39 GHz, thus introducing a huge attenuation at mm-Wave frequencies and dominating the wave propagation behavior.

2.2 Antenna coverage study

As discussed previously, having high gain isn't the sole argument to consider when selecting a mm-Wave antenna to integrate in a 5G smartphone. There must be a balance between the array's coverage abilities and the value of gain that it can provide. Highly directive beams require beam agility to maintain the link alignment and, consequently, its quality.

Antenna arrays allow the process of beam steering, which means that one antenna array alone can provide multiple beams pointing into various directions. By employing beam steering the array's radiation pattern, besides having higher gain, can avoid obstacles that would weaken or block the

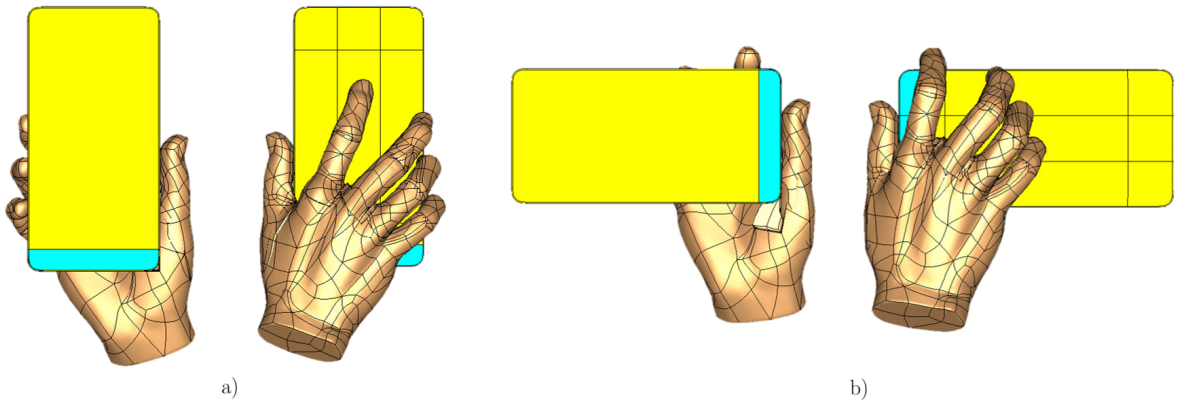

Figure 2.6: Hand grips; a) Talk mode hand grip posture; b) Browse mode hand grip posture.

signal while overall offering a bigger sweep of area coverage. To achieve a compromise between gain and coverage, a fair assessment would be to quantify the area that a set of beams sweeps without forfeiting an acceptable maximum gain value. In other words, a percentage of coverage function is obtained to identify which of the antenna families provides the best swept coverage area, for a given threshold gain value, under which wireless communications are not viable.

2.2.1 Codebook development

The first step to this study is recreating, in a simulation, the beam sweep performed by the antenna arrays. Essentially, this is achieved by computing the array's gain values for each beam in all (θ, φ) directions of observation.

The angle θ is defined by the z axis and the vector from the origin to the observation point P, varying from 0 to 180^o. The angle φ is defined by x and the projection of P in the xy plane from 0 to 360^o. Figure 2.7 shows an example of these angles highlighted in CST for a specific beam's radiation pattern.

This Figure represents one more angle, ψ, which identifies the beam. It is measured as the inclination angle between the array's axis to the beam's main lobe. If $\psi = 90^0$, as displayed in Figure, then the beam will be named ψ_{90} because it it the beam directed towards 90^o.

The proposed antennas exhibit almost 0 dB efficiency, unless the hand grips are present. In the latter case, the efficiency becomes dependent on the hands positions and the direction of the beam. A fair comparison of the antennas would imply creating and testing multiple hand grip variations. This is not feasible, considering that a number of other more important scenario conditions must be tested, increasing exponentially the number of parameter combinations. In order to keep this number compatible with simulation time of the antenna coverage, this efficiency dependence with hand grip will be ignored from this point of the investigation forward. Therefore, the total efficiency ϵ_T will be taken as 1. Considering that $G = \epsilon_T D$, realized gain and directivity become interchangeable terms. Having that in mind, the antenna gain can be calculated as seen in Equation 2.3, where $U(\theta, \varphi)$ is the antenna's radiation efficiency and P_{rad} is the power radiated

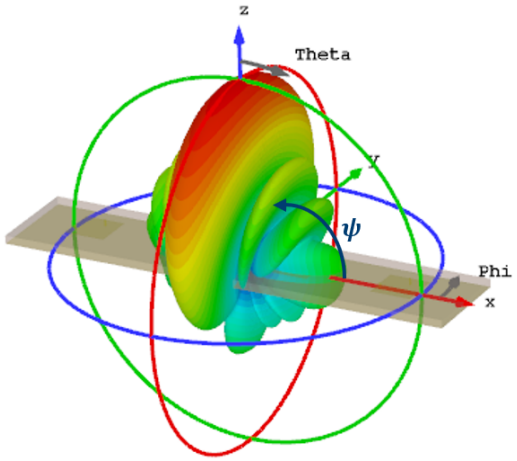

Figure 2.7: Radiation pattern for a linear, four element PBS array for beam $\psi = 90^o$ with θ, φ and ψ indicated.

through the antenna.

$$G(\theta, \varphi) = D(\theta, \varphi) = \frac{4\pi U(\theta, \varphi)}{P_{rad}}; \tag{2.3}$$

Through mathematical manipulation, this can be rewritten into Equation 2.4 that expresses the directivity in order to the electric field.

$$D(\theta, \varphi) = \frac{4\pi \left|\overline{E}\right|^2}{\int_0^{2\pi} \int_0^{\pi} \left|\overline{E}^2\right| \sin\theta d\theta d\varphi}; \tag{2.4}$$

Equation 2.5 shows the electrical field, E, that has two components, E_θ and E_φ. These components are orthogonal to each other and to the direction of propagation. It is worth mentioning that $\overline{E}$, $\overline{E}_\theta$ and $\overline{E}_\varphi$ are complex vectors, with module and phase values.

$$\overline{E}(\theta, \varphi) = \overline{E}_\theta(\theta, \varphi) + \overline{E}_\varphi(\theta, \varphi); \tag{2.5}$$

However, because this project uses linear antenna arrays, naturally, there are different $\overline{E}$ for each beam ψ, $\overline{E}_\psi$. This means that each $\overline{E}_{\theta_\psi}$ and $\overline{E}_{\varphi_\psi}$ components will be generated from the array's individual antennas $\overline{E}_\theta$ and $\overline{E}_\varphi$ components. This is where the concept of codebook comes into play.

A codebook is a set of $M \times N$ weights that are applied to the N individual antennas to generate M beams for different ψ values [38]. For a specific ψ_m, out of the M available, these N-1 weights are defined as $a(m, n)$ and are computed trough linear array theory. Because these are linear and uniform arrays, each of the antenna elements will suffer a phase shift of δ in its feeding, given by Equation 2.6, where d is the spacing between antenna elements and k is the wave number.

$$\delta_{\psi_m} = -kd\cos\psi_m; \tag{2.6}$$

The weights are then obtained through Equation 2.7 and used for $\overline{E}_{\theta_{\psi_m}}$ and $\overline{E}_{\varphi_{\psi_m}}$ calculation in Equation 2.8 and 2.9, respectively. The terms $\left|\overline{E}_\theta\right|$ and $\theta_{\overline{E}\theta}$ are, respectively, the module and phase values of the individual antenna's $\overline{E}_\theta$ component and $\left|\overline{E}_\varphi\right|$ and $\varphi_{\overline{E}\varphi}$ are, respectively, the module and phase values of the individual antenna's $\overline{E}_\varphi$ component.

$$a(m,n) = (n-1)kd\cos\psi_m; \tag{2.7}$$

$$\overline{E}_{\theta_{\psi_m}} = a(0)_{\psi_m}\left|\overline{E}_{\theta 1}\right|e^{j\theta_{\overline{E}\theta 1}} + ... + a(N-1)_{\psi_m}\left|\overline{E}_{\theta N}\right|e^{j\theta_{\overline{E}\theta N}}; \tag{2.8}$$

$$\overline{E}_{\varphi_{\psi_m}} = a(0)_{\psi_m}\left|\overline{E}_{\varphi 1}\right|e^{j\varphi_{E\varphi 1}} + ... + a(N-1)_{\psi_m}\left|\overline{E}_{\varphi N}\right|e^{j\varphi_{\overline{E}\varphi N}}; \tag{2.9}$$

Finally, with Equation 2.10, all conditions are gathered to calculate the directivity values of the array for any ψ_m out of the M available.

$$\left|\overline{E}_{\psi_m}\right|^2 = \left|\overline{E}_{\theta_{\psi_m}}\right|^2 + \left|\overline{E}_{\varphi_{\psi_m}}\right|^2; \tag{2.10}$$

CST has this functionality implemented in the post-processing tab, under the name of Combining tool. By hand typing each of the $N-1$ values of δ in the feeding of the antennas of the simulation, the beam ψ is generated. However, if the goal is to obtain a lot of beams and, therefore, a big dimensioned codebook, this can become a tedious and time consuming process, even with the help of a programmed macro.

In order to expedite the process, part of this dissertation's efforts focused on making this codebook generation and representation an automatic process. CST has an option for exporting the individual antennas' radiation pattern characteristics in the farfield region into an American Standard Code for Information Interchange (ASCII) file. Figure 2.8 is an example of a single antenna's ASCII file.

Theta [deg.]	Phi [deg.]	Abs(Dir.)[dBi]	Abs(Theta)[dBi]	Phase(Theta)[deg.]	Abs(Phi)[dBi]	Phase(Phi)[deg.]	Ax.Ratio[dB]
0.000	0.000	-2.734e+00	-2.794e+00	23.248	-2.135e+01	321.511	1.969e+01
5.000	0.000	-3.439e+00	-3.523e+00	46.294	-2.062e+01	328.519	1.730e+01
10.000	0.000	-3.196e+00	-3.285e+00	68.455	-2.011e+01	341.680	1.684e+01
15.000	0.000	-2.442e+00	-2.531e+00	85.958	-1.936e+01	359.185	1.684e+01
20.000	0.000	-1.684e+00	-1.785e+00	98.782	-1.806e+01	17.563	1.639e+01
25.000	0.000	-1.164e+00	-1.296e+00	108.302	-1.639e+01	33.513	1.542e+01
30.000	0.000	-9.397e-01	-1.128e+00	115.694	-1.466e+01	46.029	1.414e+01
35.000	0.000	-1.004e+00	-1.280e+00	121.711	-1.311e+01	55.654	1.271e+01
40.000	0.000	-1.323e+00	-1.730e+00	126.808	-1.181e+01	63.203	1.122e+01
45.000	0.000	-1.858e+00	-2.457e+00	131.256	-1.076e+01	69.304	9.705e+00
50.000	0.000	-2.566e+00	-3.443e+00	135.213	-9.944e+00	74.367	8.210e+00
55.000	0.000	-3.399e+00	-4.683e+00	138.761	-9.320e+00	78.640	6.792e+00
60.000	0.000	-4.306e+00	-6.183e+00	141.932	-8.856e+00	82.266	5.585e+00
65.000	0.000	-5.229e+00	-7.976e+00	144.713	-8.520e+00	85.320	4.911e+00
70.000	0.000	-6.106e+00	-1.015e+01	147.056	-8.285e+00	87.833	5.283e+00
75.000	0.000	-6.873e+00	-1.288e+01	148.873	-8.128e+00	89.811	7.017e+00
80.000	0.000	-7.467e+00	-1.663e+01	149.993	-8.029e+00	91.244	1.031e+01
85.000	0.000	-7.841e+00	-2.296e+01	149.785	-7.976e+00	92.119	1.653e+01
90.000	0.000	-7.960e+00	-4.691e+01	9.220	-7.961e+00	92.426	3.901e+01

Figure 2.8: Part of an ASCII file extracted from CST for one antenna of a linear four element array.

The file has 8 farfield pattern characterization parameters organized in columns:

- Theta [degrees]: θ varies with a step index of 5 degree ($d\theta = 5^o$), from 0 to 180^o.
- Phi [degrees]: φ varies with a step index of 5 degree ($d\varphi = 5^o$), from 0 to 360^o.
- Abs (Dir) [dB]: the antenna's directivity, D. Not used for this project.
- Abs (Theta) [dB]: equivalent to $|\overline{E}_\theta|$.
- Phase (Theta) [degrees]: equivalent to $\theta_{\overline{E}\theta}$.
- Abs (Phi) [dB]: equivalent to $|\overline{E}_\varphi|$.
- Phase (Phi) [degrees]: $\varphi_{\overline{E}\varphi}$.
- Ax. Ratio [dB]: This is a ratio of the E field's orthogonal components, E_θ and E_φ. If the components have the same amplitude and phase difference of 90^o (circular polarization), then the AR would be 1 (or 0 dB). For an elliptical polarization, AR would be larger than 1 (or > 0 dB). Not used for the project.

The information from these individual files was used in Equations 2.4 through 2.10 to generate a Matlab tool that, with a single simulation, generates and represents a set of beams similar to the ones that would be obtained with the Combining Tool from CST. Instead of having to calculate the δ exteriorly and typing them into CST, all that is needed is a list of desired ψ values, working frequency and antenna element spacing in the array. The script does everything else on its own.

Doing it through Matlab is not only quicker but also offers more freedom, since functionalities such as bit resolution and phase quantization can be added. For example, in this tool, an extra level of realism was added by implementing a realistic phase shifter with a bit resolution limitation. For a phase shifter with B bits there are 2^B possible phase shifts that can be provided to the antennas. Therefore, after the δ values are calculated for each ψ, the program runs through them and approximates them to the closest available phase shift. This will naturally lead to some radiation pattern recreation challenges. The beams created with this tool might be a little deviated from the original intended ψ that would be obtained in CST, where the beam combination is done under the principle of an ideal phase shifter. However, this tool method resembles real life limitations in an user terminal more than CST does. Besides, such beam deviation effect can be minimized with the increase of the bit number in the program.

Figure 2.9 a) shows the CST representation of the individual farfield radiation patterns for a linear MBS array with four elements. The array is highlighted in the blue square. The form factor is not displayed, so that the antennas could be visible. Using the ASCII file information a steering beam of $\psi = 90^o$ was created in Figure 2.9 b) using CST's combining tool and in Figure 2.9 c) with the develope Matlab tool. There is virtually no difference between the two, which validates this process.

Another very useful functionality of this tool is that it allows to visualize the representation of the codebook's envelope. This is the term used to refer to the representation of the maximum gain values of a set of beams. Using the linear four element MBS array as an example, Figure 2.10 a) shows a plane cut side (for a constant φ) view of 17 codebook beams simultaneously represented, which results in an overlap off all the radiation patterns. The 17 beams are defined from $\psi = 50^o$ to $\psi = 130^o$ with 5^o increments in inclination. The codebook envelope is the outer contour of that beam overlap, as represented in Figure 2.10 b). Figure 2.10 c) is the side view of the 3D representation of this codebook. Figure 2.10 d) represents the front and back view of the MBS

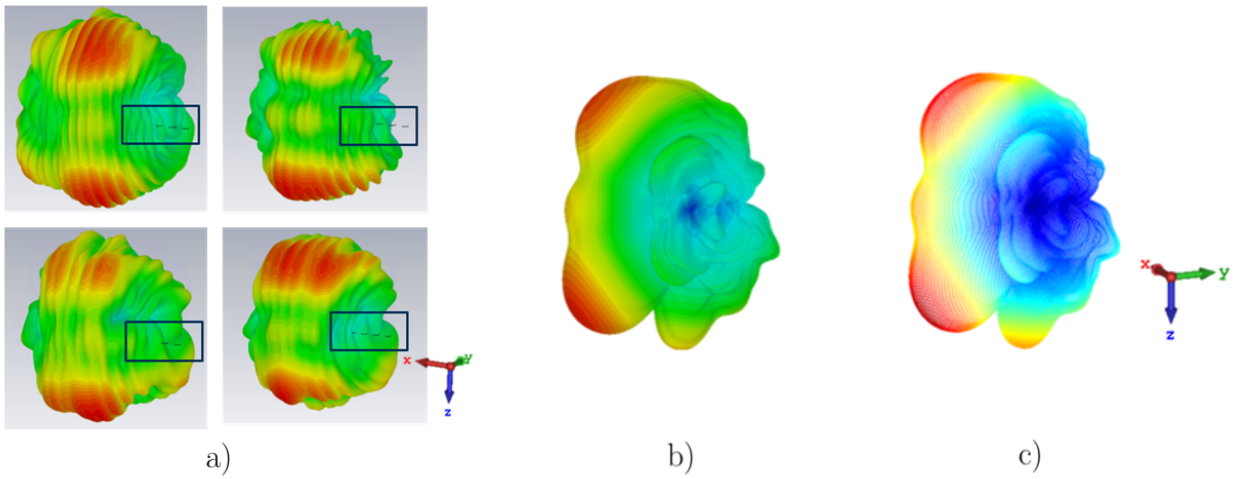

Figure 2.9: Beam process creation; a) Individual CST radiation patterns for a linear 4 element monopole array (in the blue square); b) ψ_{90} with CST's combining tool; c) ψ_{90} with Matlab tool.

codebook representation in 3D. All these images were obtained with the Matlab tool, which CST does not do. This codebook envelope will be used to construct the coverage function that the CS is based on.

2.2.2 Evaluation metric

On of the main interests of this dissertation is evaluating the antennas' coverage percentage over the solid angle. The solid angle expresses how big a section of the radiation pattern appears to be from a certain point of observation (θ, φ) and it is a function of θ, $d\Omega(\theta)$. Figure 2.11 a) represents the parametrization of a sphere using spherical coordinates, including the representation of this angle [39]. In full rigor, since θ varies from 0 to 180^o and φ) 0 to 360^o, this sphere should have 180 $\hat{\theta}$ horizontal lines and 360 $\hat{\phi}$ vertical lines traced along the sphere. However, the remaining lines are suppressed to ease visualization.

Under this principle, a coverage function was computed, to evaluate how widely in space can an antenna provide an acceptable gain value for communications. Consider a spherical representation of gain in the solid angle, as represented in Figure 2.12 a). The center corresponds to the minimum gain value of the radiation pattern, G_{min}, and the radius is the antenna's maximum gain, G_{max}, as seen in Figure 2.12 b). Figure 2.12 c) illustrates the 3D codebook envelope of a linear four element PBS array (beams between $\psi = 50^o$ and $\psi = 130^o$) delimited by the coverage sphere. Suppose that a certain gain threshold value is established, $G_{threshold}$, under which the gain is too low for the antenna to be used. The coverage function expresses the percentage of registered directions (θ,φ) of the codebook envelope that are within that gain interval, $G_{threshold} < G < G_{max}$.

Because this is an analog setup, an array cannot radiate all the beams from the codebook at once. Therefore, it could be argued that assessing the coverage of one beam at a time would make more sense than looking at the codebook as one big radiation pattern. However, using the codebook envelope allows for the assessment of the full gain coverage potentiality of the antenna solution. It

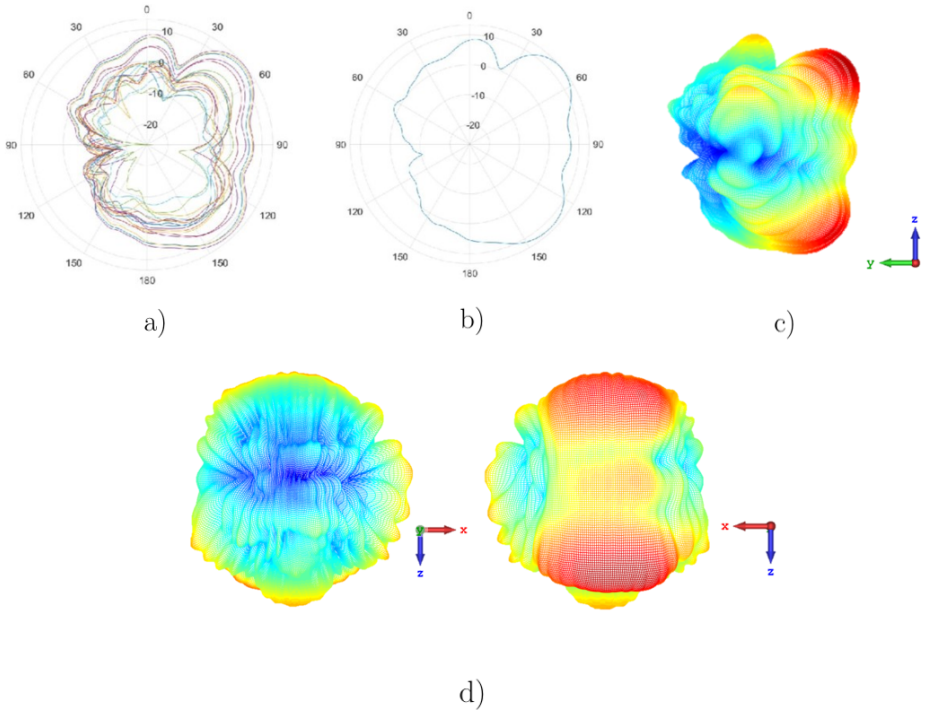

Figure 2.10: Concept of codebook envelope; a) Plane representation of superposed beams; b) Plane representation of the the codebook envelope; c) 3D representation side view of the codebook envelope; d) 3D representation back and front view of the codebook envelope.

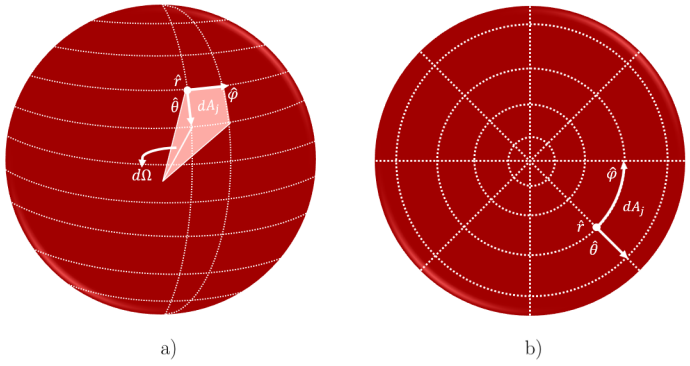

Figure 2.11: Spherical coordinates grid over a sphere; a) Top view b) Side View.

displays not only the BF ability but also the maximum achievable gain values for an antenna type, in an accurate and precise format.

However, there is on more step that needs to be performed in order to obtain the correct coverage curve. A statistical adjustment must be made that can be described as the transition of the point

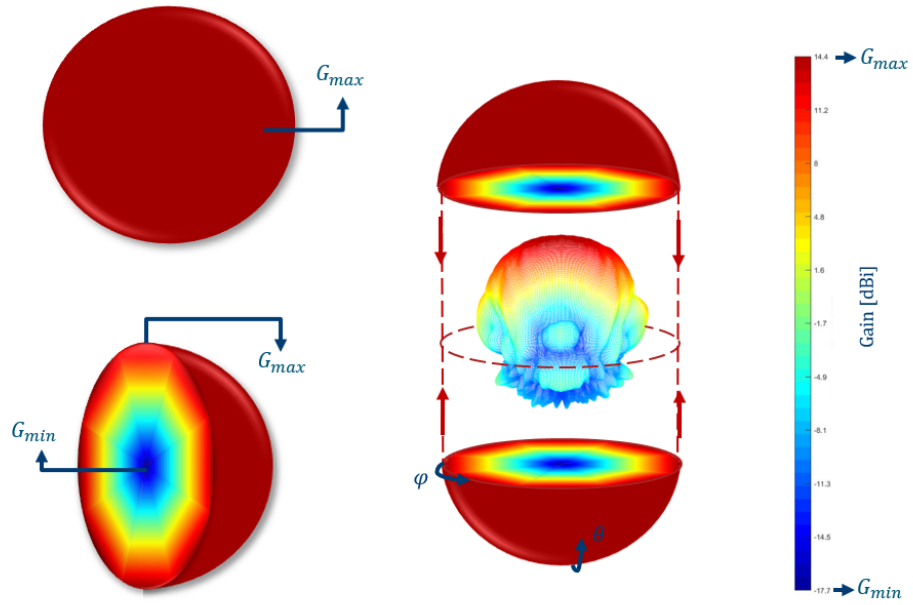

Figure 2.12: Coverage study scheme; a) Spherical representation of gain in the solid angle; b) Limits of the sphere according to the radiation pattern's gain limits; c) 1x4 linear PBS array codebook envelope delimited by the coverage sphere.

distribution in space from an uniform grid to a polar grid. When exporting data for a radiation pattern, CST samples the data for equally spaced points of the radiation pattern in $\hat{\theta}$ and $\hat{\phi}$ directions. This creates a 180×360 grid, with uniformly distributed points for each direction. However, the radiation patterns are not bi-dimensional, and this can lead to misinterpretation of the results exported.

Taking Figure 2.11 b) as an example, for each of the circles, an equal amount of points has to be captured. It is clear then that the circles vary in dimension, which leads to a discrepancy in point density along the sphere. In other words, the mapping of CST points onto the solid angle is not done uniformly. This means that the percentage of points abiding the $G_{threshold} < G < G_{max}$ condition would be dependent on how the radiation pattern would be oriented in relation to circles. The point distribution is denser when the observation point is close to $\theta = 0$ and gets sparser as it approaches $\theta = 90^o$.

As an example, Figure 2.13 a) and Figure 2.13 b) display the CST representation of the $\hat{\theta}$ and $\hat{\phi}$ lines for the radiation patterns of the PBS and MBS with the ψ_{90} beam. If the maximum of the beam was aligned with one of the smaller circles, as in Figure 2.13 a), the number of points registered would be much higher than if the radiation pattern was rotated 90^o over $\hat{\theta}$, making it coincident with the bigger circles.

Thus, to make the coverage function independent of radiation pattern orientation, a weight adjustment in the contribution of the points must be made based on their coordinates. If there

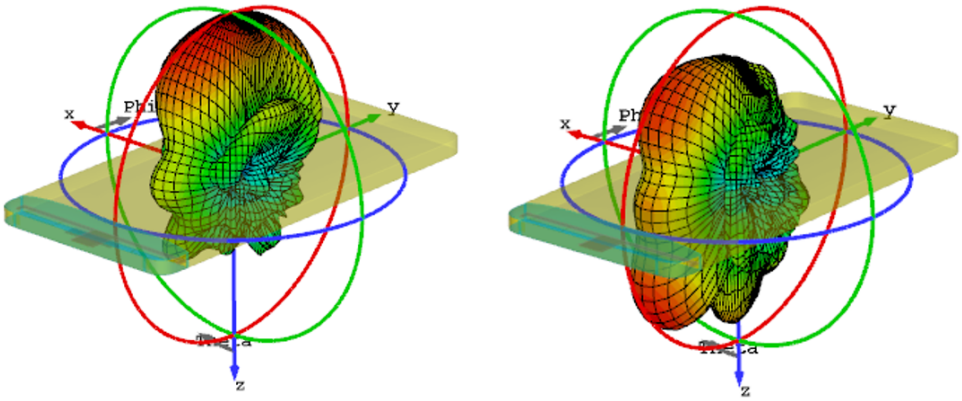

a) b)

Figure 2.13: Spherical grid applied in CST for the PBS and MBS radiation patterns implemented in the form factor for $\psi_d = 90^o$; a) PBS; b) MBS.

is a high density of points in an area, they should weight less than in areas where the points are more spaced apart. Equation 2.11 and Equation 2.12 show that the solid angle integration along the sphere is 4π.

$$d\Omega = sin\theta d\theta d\phi; \tag{2.11}$$

$$\Omega = \int_0^{2\pi} \int_0^{\pi} \sin\theta d\theta d\phi = 4\pi; \tag{2.12}$$

For an isotropic source, $d\Omega$ would give a measure of the fraction of total radiated power flowing between four adjacent points in the observation directions lattice, but in spherical coordinates this is a function of θ. This can be used to compute the weight contributions for each point, pc_w, registered for the function according to its θ value, as depicted in Equation 2.13.

$$pc_w(\theta) = \frac{d\Omega}{\Omega} = \frac{\sin\theta d\theta d\phi}{4\pi}; \tag{2.13}$$

This will then create a curve that will represent the coverage percentage, $Coverage_{\%}$, for L levels of $G_{threshold_l}$. This calculation is described in Equation 2.14, where $N_{G_{threshold_l}}$ is the number of points that are above $G_{threshold_l}$, pc_w is the corresponding weight value according to the points' θ coordinate and TP is the total number of points analyzed.

$$Coverage_{\%} = \frac{\sum_{n=1}^{N_{G_{threshold_l}}} pc_w(\theta_n)}{TP}; \tag{2.14}$$

This curve will reveal that there is a clear balance that needs to be achieved between coverage and gain, since it is not possible to have both things at the same time for 5G and, therefore, having a tool to make this analysis and establish a compromise between both is very important.

2.2.3 APA Toolbox

Since the previous envelope coverage analysis is very important, and may be equally relevant in other contexts, a Matlab toolbox was developed using Matlab App Designer. Other important functions not available in CST were developed in the tool, organized and categorized in a graphic user interface so that it could be easily accessible to everyone who would like to use it without being familiar with the code. It was named Antenna Pattern Analysis Toolbox (APA TBX).

Figure 2.14 shows that the app comprises two different tools: Codebook Analysis and a In-depth CS. With the Codebook Analysis tool, the user can load the antenna array elements individual ASCII files from CST and set the simulation parameters, such as resonance frequency, spacing between the array elements, phase shifter range, bit resolution and codebook entry selection.

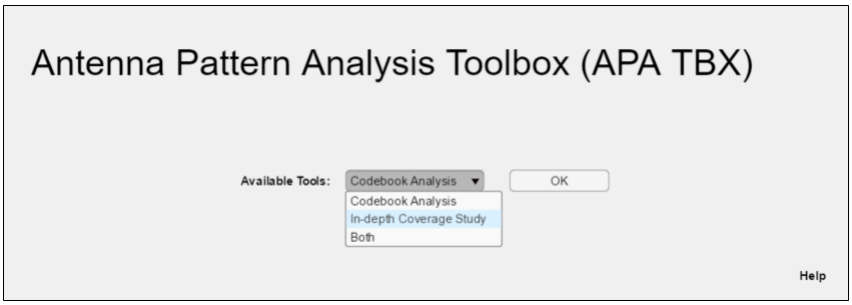

Figure 2.14: Array Pattern Analysis Toolbox (APA TBX) interface.

This tools presents the User with three different representations of the Radiation pattern in question: 3D representation , Stereographical representation and Plane Cut Representation, for any φ or θ plane cuts of choice and an option to view the codebook envelope or all entries overlapped, as well as coverage curve.

It has two modes, the first one is the Single mode, as displayed in Figure 2.15, for single array analysis. For a comparative analysis, the information of one more array is allowed for the Comparison Mode, where the analysis described above is done under the same conditions for both antenna arrays to make the comparison process fair, as seen in Figure 2.16.

If the user requires some more information specifically regarding the CS, besides the curve representation, the In depth CS tool, shown in Figure 2.17, can be used. The user selects the files for all the cases he wants to compare, and types in the simulation parameters. The tool will display the coverage curves for all the arrays entered overlapped under the same conditions, as well as the maximum gain for each array, and an information table that identifies which array reaches 50% and 100% coverage percentage first. An advantage of this tool is that there isn't a two array limitation for coverage study comparison, the user is free to compare how many antenna solutions as he desires.

2.3 MIMO Channel Simulator

For MIMO communications, a huge part of system performance evaluation revolves around the MIMO channel. Usually, MIMO system simulators simplify the antennas to be isotropic and model the channel using an adequate distribution function, according to the desired environment (Rician or

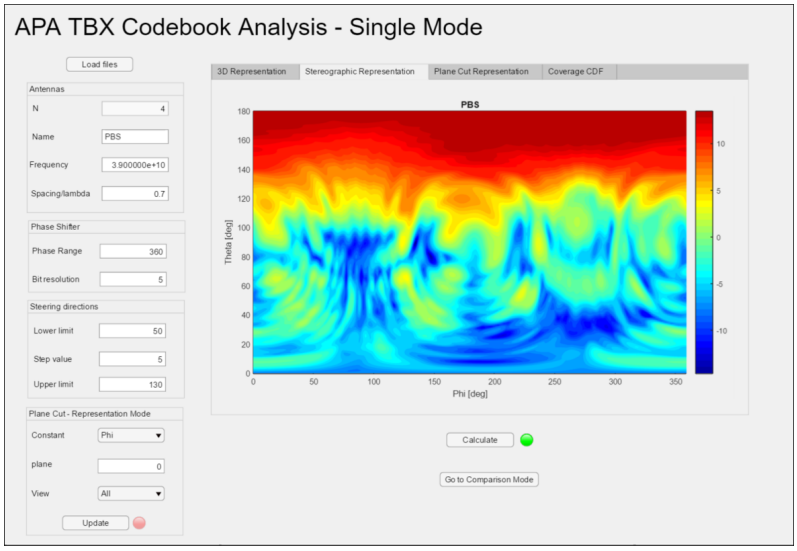

Figure 2.15: APA TBX: Stereographical representation of a linear four element PBS array's codebook in Single Mode Codebook Analysis.

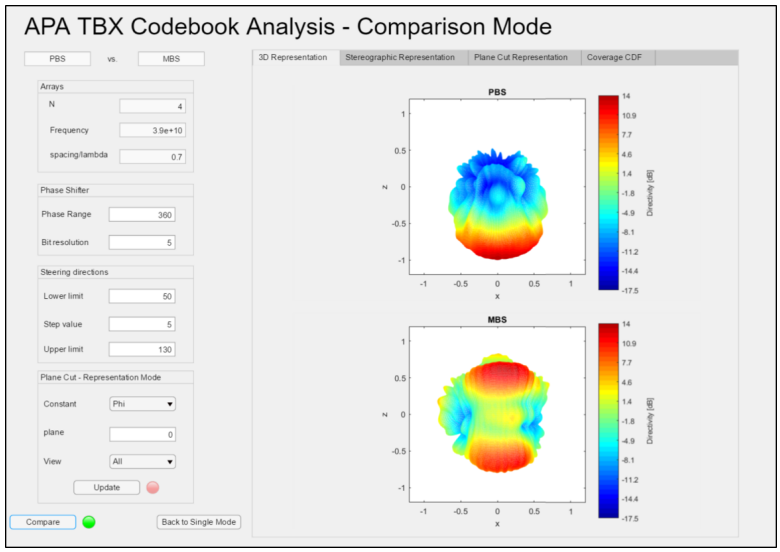

Figure 2.16: APA TBX: 3D Codebook Radiation patterns for linear four element PBS and MBS arrays in Comparison Mode Codebook Analysis.

Rayleigh, for example). However, since this dissertation focus mostly on the antenna contributions, it is only pertinent to study how the antennas influence this communication channel, since that would provide a more realistic indicator as whether these antennas would perform well in a MIMO context.

Another motivation for this particular study is the fact that the ability to perform SM is listed in the literature as one of the main arguments for using patch antenna solutions in smartphone antenna implementation. In theory, because of its simplicity to implement dual-linear orthogonal

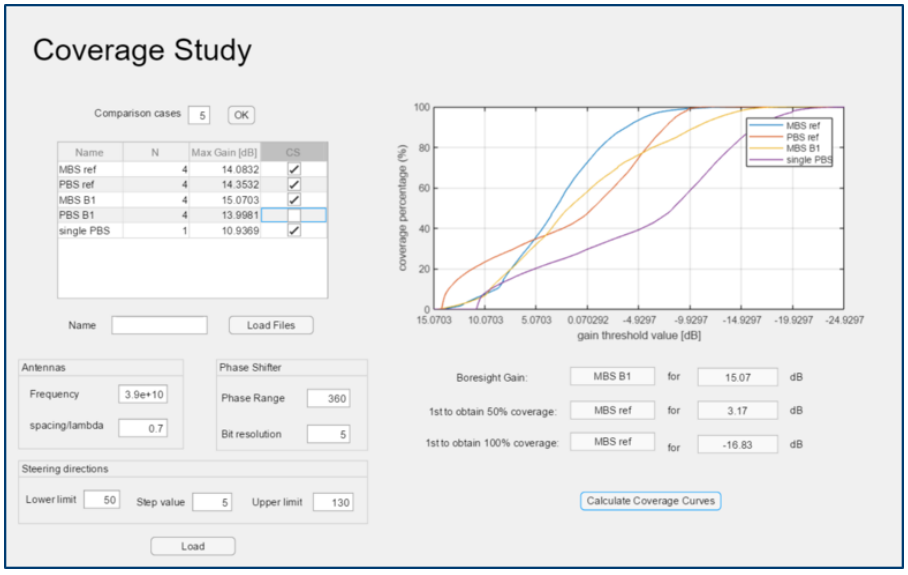

Figure 2.17: APA TBX: In-depth Coverage Study Interface.

polarizations, a patch array could transmit two different data streams simultaneously using the same frequency band. This would significantly increase the channel's spectral efficiency, not to mention that having the equivalent to two orthogonal patch arrays occupying the volume of only one array would be an attractive design for the continuously space constricted smartphones.

However, patch arrays have high gain directive beams, therefore, cover a more limited area in space than the monopoles. This might mean that, even if SM is achievable, it would only be available in a smaller range in space, neglecting all other directions and further aggravating the problem of sudden loss of communication, which may be frequent in mm-Wave. Therefore, it is also crucial to the antenna comparison process to check if this statement is true, since SM isn't so easily achievable with monopole antennas.

Due to space limitations, if a second MBS array were to be added in this project, it could only fit in the symmetrical position of the first MBS array, which would mean the two arrays would share the same polarization. This array configuration is believed to deteriorate MIMO performance, since the arrays are parallel to each other instead of orthogonal, which is the best antenna placement method to achieve polarization isolation.

An interesting approach would be, depending on the surrounding environment, to switch the MBS arrays transmission technique between MIMO and SISO depending on which of the two would provide the best throughput. If the environment was invariant in time, like a LOS environment, the SISO approach would be indicated. In order to prevent cross polarization, only one of the UE arrays would be selected, based on a discriminating criteria, to carry out the signal transmission. The array would then perform communications using the beam that would provide the best quality of communication. The spectral efficiency would not be as high as the PBS's, but it might still be able to provide a stable and uniform data rate distribution over space, which is important for communication reliability.

On the other hand, in a more urban environment, with a lot of reflections, a common phenomenon

experienced is the signal's loss of polarization. Depolarization would be an advantage for MIMO using MBS arrays since it woud create, for each array, different signal propagations, preventing cross polarization. This way, the MBS could rival the PBS not only in gain coverage but also in data rate.

This comparison might eventually come down to a decision between achieving higher values of data rates, securing a stable data rate threshold for all directions in space or maybe a compromise between both.

Therefore, in order to evaluate the antenna influence in the MIMO channel and further consolidate the antenna comparison process, a geometric discrete scattering channel model is developed to evaluate the MIMO channel performance for any type of environment scenario that the user desires to test.

Regarding the antenna contribution, this model considers pertinent antenna characteristics such as radiation patterns, coupling and antenna polarization. The model also incorporates the studies made in previous Chapters on the effects of the form factor and the user influence (both human body blockage and UE involuntary rotation) in the antenna performance, reinforcing the results obtained from the coverage study. Also, the environment conditions implemented can either be static or have time-varying elements that produce Rayleigh fading (which is commonly accepted as a fair model of fading in urban areas), depending on the type of environment chosen for testing.

This implies that the channel characteristics will be antenna dependent, therefore the PBS and MBS can, in fact, be compared to each other in another category: MIMO channel performance.

In other words, for each antenna family, the MIMO channel performance will be evaluated for 18 different UE-BS orientations in different test scenarios. This will allow to quantify, for each antenna family, how sensitive the MIMO channel performance is to the phone's range of motions. Ideally, the chosen antenna family should be able to provide good MIMO communications for all user defined UE positions. The goal will be to create several different scenarios within the modeled environment and see how the channel reacts, creating a learning process on the behavior of the channel for each of the antenna families.

When compared to pure statistical models used in the literature, the hybrid deterministic/statistical MIMO channel simulator created for this project is an accurate and reliable (as far as simulators go) tool to recreate realistic test scenarios for channel assessment. The advantages are:

- Instead of considering isotropic antennas or an approximate gain value to characterize the antenna's gain, this simulator uses realistic antenna patterns obtained from simulations and specific antenna characteristics such as polarization and coupling, not only for the direct path, but also for all individual scatterers according to its position in space.
- It includes a BF functionality with editable phase shifter characteristics such as phase shifter range and bit resolution.
- The smartphone's effect, with its metallic elements, is included in the simulations.
- The user's influence is also accounted for. Not only regarding the smartphone rotation around the x, y and z axis, but also the human body blockage effects that seriously deteriorate the antennas performance but are often absent in these models.
- Implementation of a beam pair link selection criteria to chose for both the UE and the BS,

the most indicated beam to use for the environment conditions, which contributes for the realism of the process.

- Freedom in the scenario characterization, since the relative position between the UE and the BS in the global coordinate system is customizable.
- Scatterer definition is, indubitably, one of the major contributions for the versatility of this simulator. The randomness in scatterer space distribution and range of motion per time slot contributes to recreate a truly dynamic urban environment, depicted in Figure 2.18.

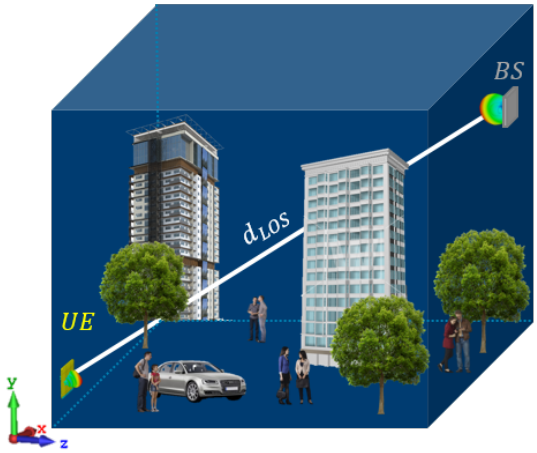

Figure 2.18: Representation of the MIMO channel simulator.

- Adjustable number of scatterers, which generates different types of fading. By having fewer scatterers, there will be an inevitable dominant LOS component, which will be fitting to Rician's fading distribution. On the other hand, a higher number of scatterers will create a rich MP environment, thus mimicking Rayleigh fading.
- When producing Rayleigh fading, pure statistical simulators use a combination of already defined gaussian distributions to define the channel state matrix, H, whereas in this simulator the Rayleigh fading is created naturally by adding up all propagation influencing components to the H matrix calculation. This allows for an unprecedented control over the characteristics of reflection and depolarization of the scatterers, that is not possible when defining fading by the use of statistical models.
- Finally, the channel capacity calculation is based on a link budget analysis, instead of the statistical model typical approach of defining a fixed value for the signal to noise ratio (SNR).

Nonetheless, performing real life measurements would provide more reliable data, since many other unforeseen factors would also be taken into account. However, this kind of measurement endeavors can turn out to be very complex and expensive. For this thesis' specific case, mm-Wave antennas are very small and their production and form factor integration in lab facilities can be challenging. Also, hand models for such high frequencies are yet to be available in the market. Another disadvantage is that the number of scenarios that can be tested in practice are limited for practical reasons. In simulations, it is much easier to perform several test conditions than doing it experimentally, allowing for much more detailed and extensive studies.

2.3.1 MIMO channel model

The channel model was idealized for a hybrid MIMO + BF scenario, like the one in Figure 2.19. The UE has two arrays in the bottom back of the phone, A_{UE1} and A_{UE2}, and two arrays in the BS, A_{BS1} and A_{BS2}, This is a very common approach in 5G MIMO strategies where MIMO is combined with BF to boost not only gain (using a high number of array elements) but also to improve power consumption and coverage. The two pairs of arrays create four individual transmission paths, each one of them with a complex transmission coefficient, h_{11}, h_{12}, h_{21} and h_{22}. Once put together, these coefficients form a 2x2 channel matrix H that summarizes in matrix form the current channel state in response to the environment.

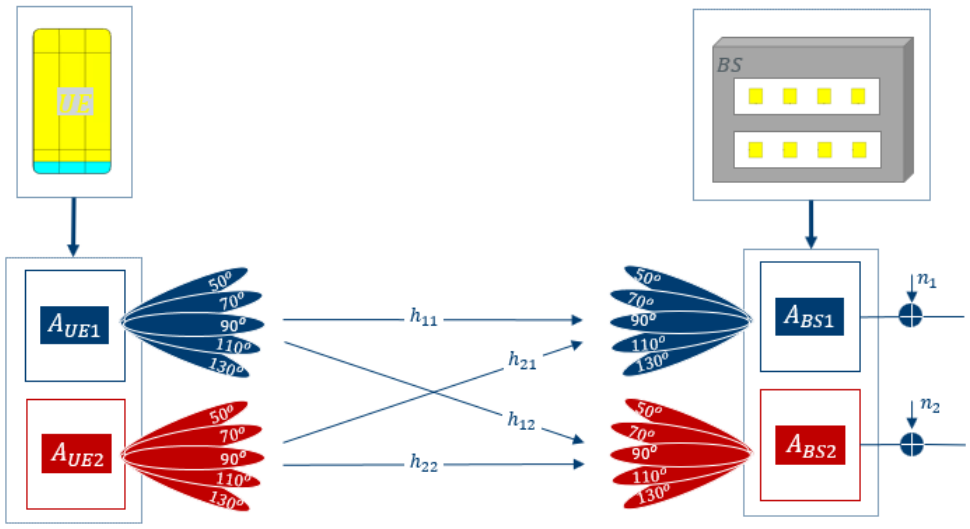

Figure 2.19: MIMO channnel diagram representation.

The BS's two arrays, A_{BS1} and A_{BS2}, are two linear, four element PBS arrays with orthogonal polarizations, one over x axis, and another over the y axis. They are spaced by a 2.5 cm gap. The UE's two arrays, A_{UE1} and A_{UE2}, are integrated in the back of phone. These UE arrays can belong to two types of antenna families.

If the antenna type being evaluated is the PBS, then the arrays will be condensed into one linear, four element, dual polarized PBS array, where SM is performed. It is a 2x2 MIMO + BF transmission mode. The two UE arrays transmit simultaneously two streams, s_1 and s_2, over two of the four channels available, which are received by the two BS arrays that have some additive noise to them, as can be seen from Figure 2.20.

However, for the MBS family, two arrays are placed symmetrically in the mobile phone, horizontally and with the same orientation. Because of the way the arrays are implemented, two transmission modes are anticipated.

In a predominantly LOS environment, the chosen mode is a 1x1 MIMO + BF transmission model (or a SISO + BF mode), depicted in Figure 2.21. One of the UE arrays sends a single stream of information, s_1 , through one of the four channels to one of the BS arrays (that adds

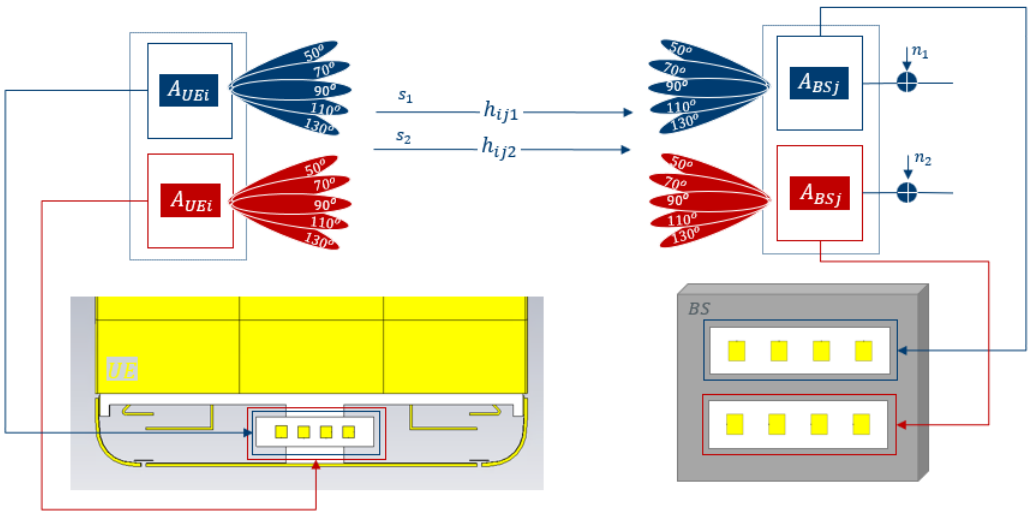

Figure 2.20: 2x2 MIMO channel representation for PBS.

some noise).This is because the two arrays in the UE present the same polarization and, therefore, are expected to interfere and perform poorly in MIMO communications.

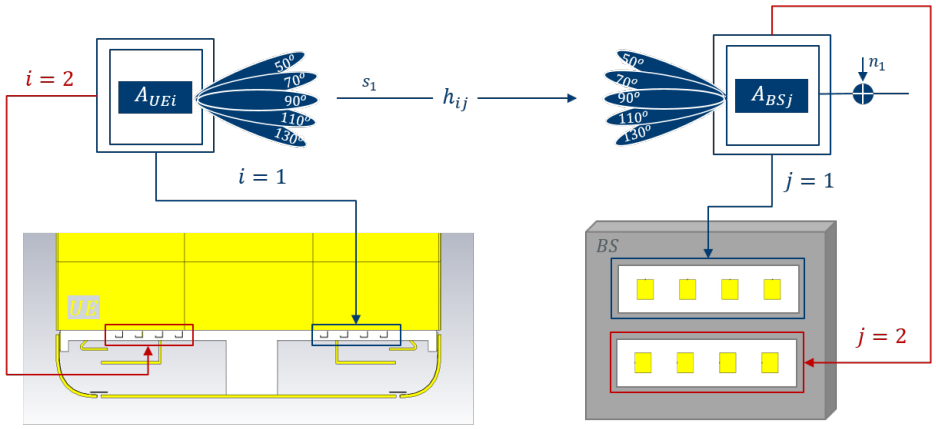

Figure 2.21: SISO channel representation for MBS.

On the other hand, in an environment with enough reflections, the transmission mode will be, similarly to the PBS, a 2x2 MIMO + BF transmission mode, like the one depicted in Figure 2.22.

Regarding the UE and the BS array's BF ability, the number of beams generated has been set to five codebook entries, $b = 5$. These are $\psi = 50^o$, $\psi = 70^o$, $\psi = 90^o$, $\psi = 110^o$, $\psi = 130^o$. These entries are enough to cover well the solid angle without raising too much the simulator's computation time.

The corresponding 3D channel model representation can be found in Figure 2.23, where it is introduced the schematic representation of the scatterers (trees, buildings, people, passing cars) as grey cross marks. For a clearer picture, the xy plane and the xz plane representation of the 3D

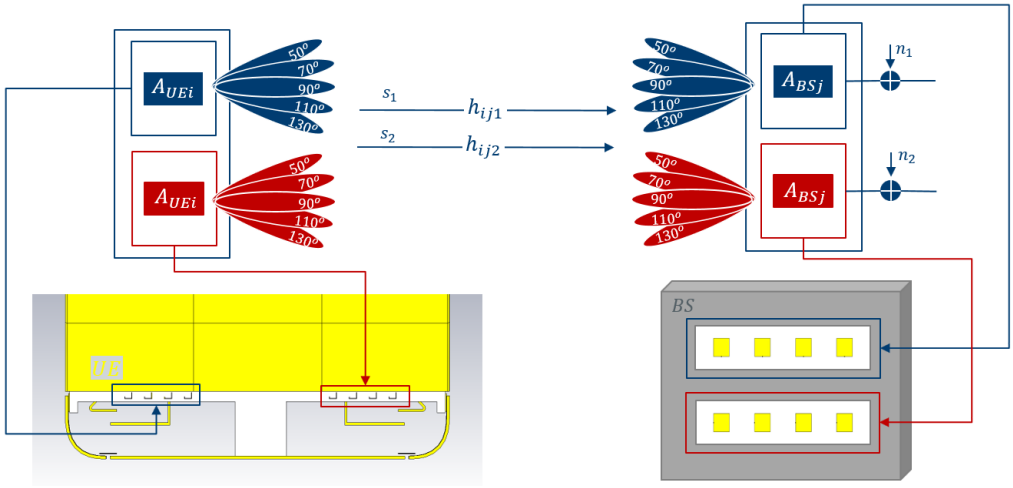

Figure 2.22: 2x2 MIMO channel representation for MBS.

model are also represented. The UE end is located in the xy plane for $z = 0$ and the BS is also located in the xy but distanced from the UE along z.

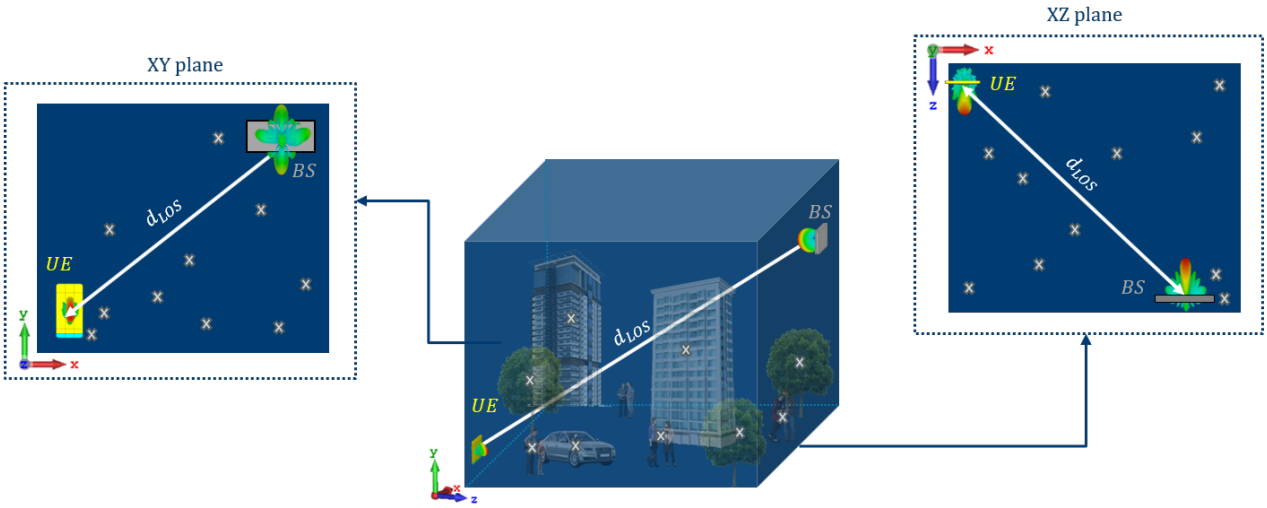

Figure 2.23: Scatterer representation in the channel model.

The UE and BS are separated by a distance $d_{LOS_{UE,BS}}$ and, between them, S obstacles are distributed randomly over a confined space. These scatterers, that mimic every day obstacles in an urban area, move randomly along the x axis over time. They will be responsible for creating enough reflections of the signal (MP) to allow for the MIMO channel to be successfully created. Therefore, the H matrix will be created for a specific set of environment conditions during a large number T of time slots, in order to create a fading distribution that can be evaluated. Because all beam combinations between the BS array and the UE array, C, will be taken into consideration, the H matrix will be calculated $T \times C$ times, thus becoming a 3-dimensional matrix. Because of this, it is

crucial to have an algorithm to select the best beam pair link combination C_k. The corresponding H matrix will then be put through the channel assessment metrics that will decide on the channel's performance using a specific antenna family. This is detailed in the next section.

2.3.2 H matrix calculation

In a typical urban environment there are two signal propagation types. On one hand, there is the direct line of sight path (LOS), when the transmitter and the receiver have an unobstructed path between them. On the other hand, there is also propagation through MP, where the signal is reflected and scattered into multiple directions only to arrive at the receiver trough several different paths and with different phase shifts. So, in order to obtain the channel state matrix, both types of components must be considered into the calculations.

2.3.2.1 LOS component

In a LOS scenario, shown in Figure 2.24 a), there are no sources of signal reflection and the h_{LOS} parameters from the channel matrix H can be simply described in Equation 2.15. In this equation, G_i is the UE array antenna gain and G_j is the BS array antenna gain. Also, $d_{ij_{LOS}}$ is the distance between the UE array i and the BS array j, represented in Figure 2.24 b).

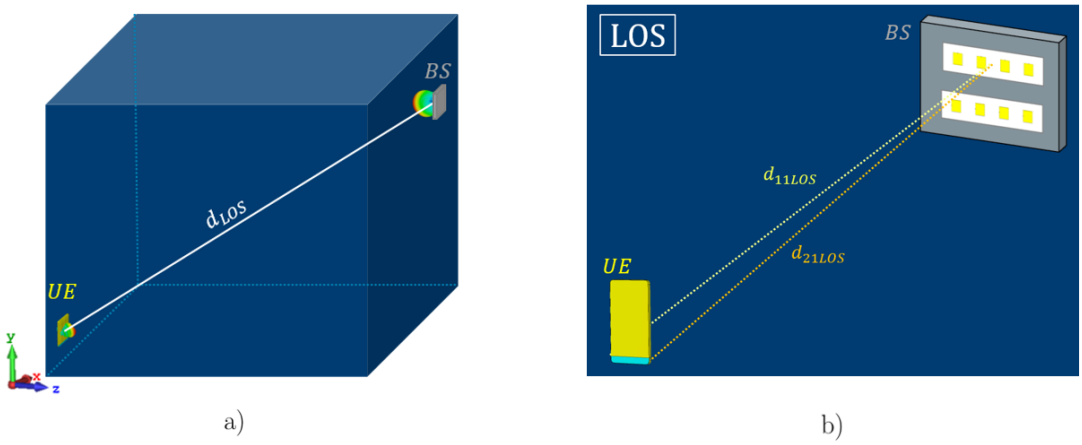

Figure 2.24: LOS scenario; a) Representation of LOS scenario in 3D; b) Calculation of $d_{ij_{LOS}}$.

$$h_{ij_{LOS}} = \sqrt{G_i(\theta^{UE}, \varphi^{UE}) G_j(\theta^{BS}, \varphi^{BS})} \frac{e^{-jkd_{ij_{LOS}}}}{d_{ij_{LOS}}}; \tag{2.15}$$

Finally, θ^{UE} and φ^{UE} are the θ and φ directions in which the UE sees the BS, while θ^{BS} and φ^{BS} are the θ and φ directions in which the BS sees the UE. Figure 2.25 is a schematic representation on how to define this directions in the model's global coordinate system. In full rigor, there should be a set of (θ, φ) drections that described how each array of the UE see each of the BS arrays, and vice versa. However, because the arrays are so close together in the UE and in the BS, these observation pairs end up blending into two single pairs: $(\theta^{UE}, \varphi^{UE})$ and $(\theta^{BS}, \varphi^{BS})$.

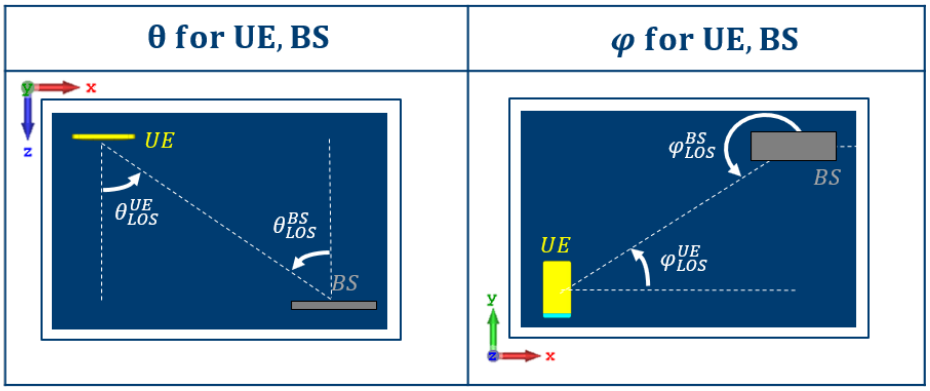

Figure 2.25: Measurement notation in space of $(\theta^{UE}, \varphi^{UE})$ and $(\theta^{BS}, \varphi^{BS})$.

The next step is to obtain the UE's and the BS's radiation patterns, in order to compute $G_i(\theta^{UE}, \varphi^{UE})$ and $G_j(\theta^{BS}, \varphi^{BS})$. Since the number of entries is small, CST's combining tool in the Post-Processing tab was used to create the 20 radiation patterns, since each of the four arrays, $A_{UE1}, A_{UE2}, A_{BS1}, A_{BS1}$, has 5 beams available. Therefore, the E_θ and the E_φ values are extracted from CST for both the UE's radiation pattern and the BS radiation pattern.

A notation was defined for the UE and the BS's arrays based on their polarization. For the case of the PBS, the first array in the UE, A_{UE1}, oriented along y-xis, is said to be vertically polarized, V. Therefore, the second array of the UE, A_{UE2}, oriented along the x-axis, will have horizontal polarization, H. In the the MBS's case, the arrays can't be distinguished using polarization, since they share the same orientation. However, these arrays, unlike the PBS, differ in location on the phone. So, there's the right hand side array, R and the left hand side array, L. These more loose terms of array nomenclature were defined because the UE can rotate in space, so it wouldn't be accurate to describe all possible orientations as simply x or y. On the contrary, the BS is fixed so the polarizations for A_{BS1} and A_{BS2} are called, respectively, Y and X.

The E-field components obtained are called, for the PBS, E_θ^V and E_φ^V for A_{UE1} , E_θ^H and E_φ^H for A_{UE2}; for the MBS, E_θ^R and E_φ^R for A_{UE1} , E_θ^L and E_φ^L for A_{UE2}; E_θ^Y and E_φ^Y for A_{BS1} , E_θ^X and E_φ^X for A_{BS2};

However these are expressed in polar coordinates. Because the complexity of the scenario with scatters and depolarization effects, it is wise to convert the fields to Cartesian coordinates. Therefore, this system is being defined with Cartesian coordinates. It is then required a transformation from (θ, φ) to (x, y), as depicted in Equation 2.16 to Equation 2.19, where the cartesian E-field components E_{0x} and E_{0y} are obtained.

$$E_{0x}^{V/H/R/L} = E_\theta^{V/H/R/L} \cos\theta^{UE} \cos\varphi^{UE} - E_\varphi^{V/H/R/L} \sin\varphi^{UE}; \tag{2.16}$$

$$E_{0y}^{V/H/R/L} = E_\theta^{V/H/R/L} \cos\theta^{UE} \sin\varphi^{UE} + E_\varphi^{V/H/R/L} \cos\varphi^{UE}; \tag{2.17}$$

$$E_{0x}^{Y/X} = E_\theta^{Y/X} \cos\theta^{BS} \cos\varphi^{BS} - E_\varphi^{Y/X} \sin\varphi^{BS}; \tag{2.18}$$

$$E_{0y}^{Y/X} = E_{\theta}^{Y/X} \cos\theta^{BS} \sin\varphi^{BS} + E_{\varphi}^{Y/X} \cos\varphi^{BS}; \tag{2.19}$$

Using these components, it is now possible to particularize the H matrix calculation to obtain the numeric values of $h_{11_{LOS}}$, $h_{21_{LOS}}$, $h_{12_{LOS}}$, $h_{22_{LOS}}$, as can be seen from Equation 2.20 to Figure 2.23.

$$h_{11_{LOS}} = E_{0y}^{V}(\theta_{LOS}^{UE}, \varphi_{LOS}^{UE}) E_{0y}^{Y}(\theta_{LOS}^{BS}, \varphi_{LOS}^{BS}) \frac{e^{-jkd_{11_{LOS}}}}{d_{11_{LOS}}}; \tag{2.20}$$

$$h_{21_{LOS}} = E_{0x}^{V}(\theta_{LOS}^{UE}, \varphi_{LOS}^{UE}) E_{0x}^{X}(\theta_{LOS}^{BS}, \varphi_{LOS}^{BS}) \frac{e^{-jkd_{21_{LOS}}}}{d_{21_{LOS}}}; \tag{2.21}$$

$$h_{12_{LOS}} = E_{0y}^{H}(\theta_{LOS}^{UE}, \varphi_{LOS}^{UE}) E_{0y}^{Y}(\theta_{LOS}^{BS}, \varphi_{LOS}^{BS}) \frac{e^{-jkd_{12_{LOS}}}}{d_{12_{LOS}}}; \tag{2.22}$$

$$h_{22_{LOS}} = E_{0x}^{H}(\theta_{LOS}^{UE}, \varphi_{LOS}^{UE}) E_{0x}^{X}(\theta_{LOS}^{BS}, \varphi_{LOS}^{BS}) \frac{e^{-jkd_{22_{LOS}}}}{d_{22_{LOS}}}; \tag{2.23}$$

It is important to mention that the LOS component of the H matrix will not change with the time slot progression. If the environment conditions are stable, then the h parameters depend solely on the antennas' characteristics of propagation distance and, therefore, will not change over time. This in not the case with the MP component of the H matrix that will be explained in detail below.

2.3.2.2 MP component

MP is the propagation phenomenon that allows for a transmitted signal to reach a receiving antenna through numerous paths caused by reflections and diffraction from obstacles. Consequently, the received signal is a combination of the LOS component and the MP components. It is thanks to these MP components that MIMO processes are possible, since MIMO gain heavily relies on the multiple propagation paths caused by obstacle filled environments. If it were not for these fortuitous scatterers there would not be a possibility to send multiple simultaneous streams, because the signals would all propagate in the same direction and would end up getting mixed with the others. An ideal environment to implement MIMO is the urban environment, a city with tall buildings, such as the one replicated with this simulator, represented in Figure 2.26 a).

For this simulator, S scatterers are spread randomly within a rectangular limit from the UE to the BS, regardless of the relative position of the UE and the BS, as can be seen from Figure 2.27. The size of the rectangle stems from the assumption that a scatterer's contribution is only relevant if it is within a certain range from the direct LOS component. Here, the range chosen was about 6 meters. It is also assumed that these scatterers move only in the x axis and their range of motion over T time slots does not exceed 2 meters (from -1 meter to +1 meter).

Naturally, if a No Line-of-Sight (NLOS) scenario were to be considered, then these scatterers within the rectangle would not contribute to the results (because their path would be blocked) and some other set of scatterers would be generated, for a wider rectangle, to recreate the concept of using further away sources of MP to still ensure some sort of communication in the case of

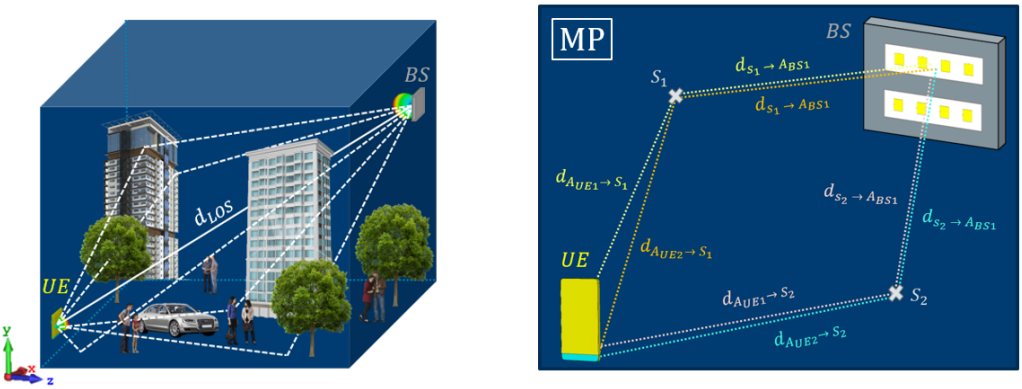

a) b)

Figure 2.26: MP scenario; a) Representation of MP scenario in 3D; b) Calculation of $d_{ij_{MP}}$.

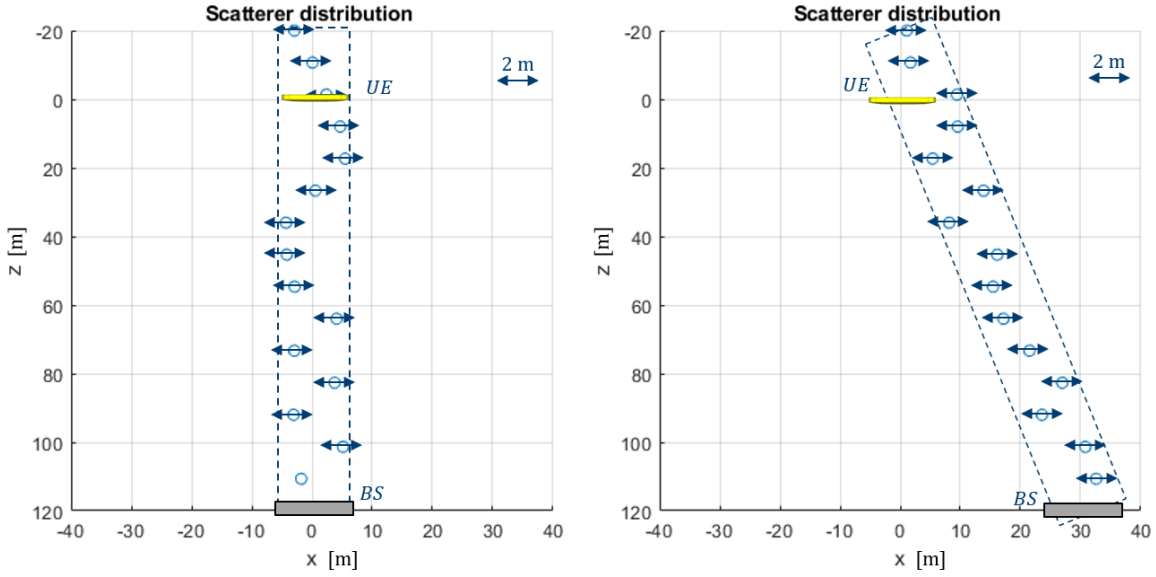

a) b)

Figure 2.27: Scatterer distribution over T time slots; a) UE and BS aligned; b) UE and BS misaligned.

LOS obstruction. The number of scatterers was carefully used so that there would be enough MP to recreate Rayleigh fading. In full rigor, both LOS and NLOS sets of scatterers should always be present. But because that would increase the computation time to calculate what would end up being a very small contribution to each other's results, these two scenarios ended up being differentiated.

In a scenario including MP, there is a criteria to pick the number of scatterers, S to obtain

Rayleigh fading. Figure 2.28 shows the comparison between a theoretical Rayleigh distribution (in red) and the fading distribution obtained from the simulator for a different number of S analyzed over $T = 1000$ time slots. The more scatterers were used to add to the LOS component, the more the two curves matched. They stabilize between $S = 10$ and $S = 15$. Any more scatterers would only add computation time and would not affect the overall outcome of the distribution. Therefore, the number of scatterers for the MP simulations was settled at 15.

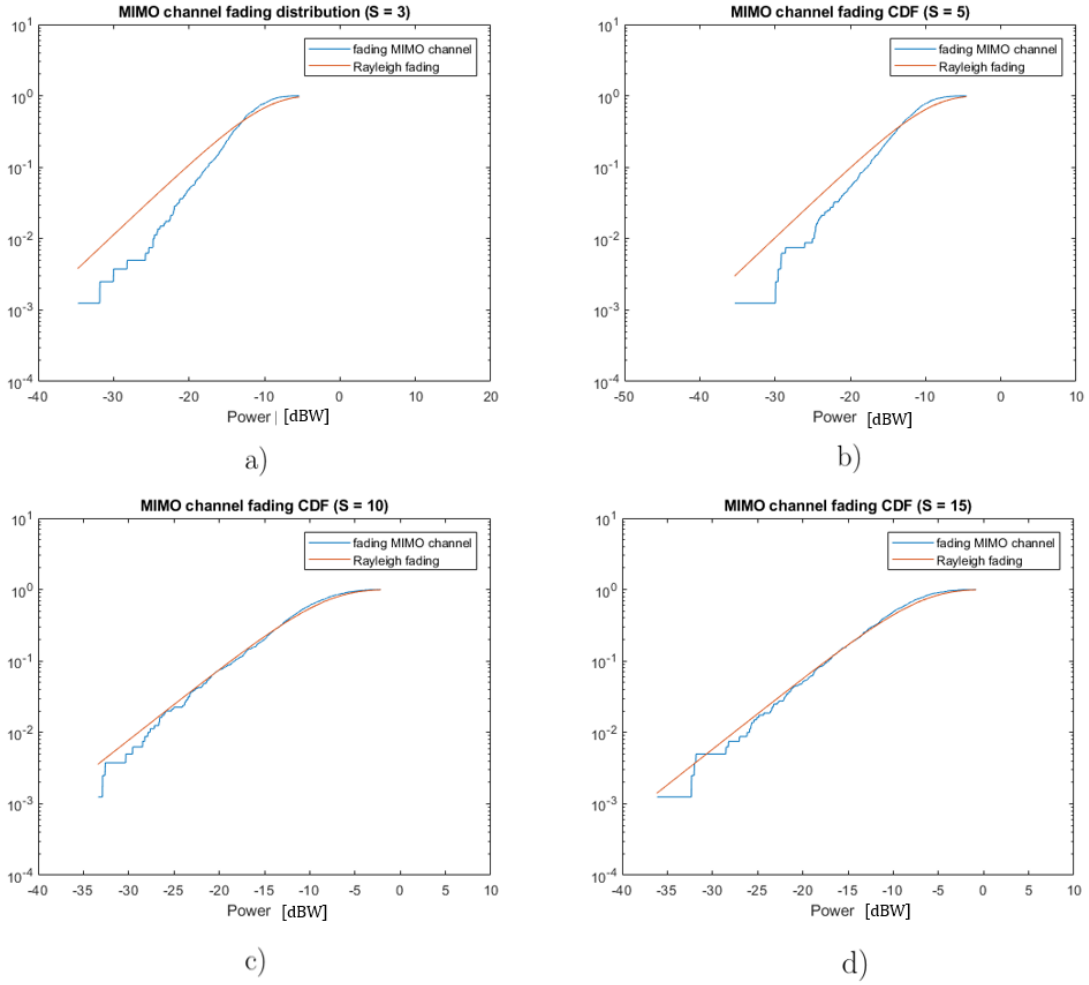

Figure 2.28: CDF representation of h_{11} over T=1000 time slots for different number S of scatterers; a) S=3; b) S=5; c) S=10; d) S=15.

The scatterers characteristics of this simulator can be adjusted to mimic a more or less MP rich environment. Besides being able to place and move the scatterers randomly across space, this allows for the scatterers to have reflection coefficient parameters, Γ_x and Γ_y, to dictate how reflective its surface is in the x and y polarizations, respectively. The smaller the reflection coefficients, the less reflections there are and the MP component gets smaller.

Similarly, another scatterer variable was implemented to describe the depolarization that occurs

in a signal reflection. When a signal gets reflected by a scatterer, its polarization can shift, affecting its original polarization. This will influence the amount of information the receiving array captures. So, two angles were defined, β and γ, to set the depolarization angles induced by the scatterers for x and y polarization incident waves.

For a more realistic dynamic environment, these scatterers' position, reflection and depolarization characteristics change over each time slot according to adequate probability distributions functions with specific reference values. The MP in this simulator is meant to create a fading effect similar to Rayleigh fading. Rayleigh fading's amplitude, by definition, follows a Gaussian distribution and its phase values follow an uniform distribution. Therefore, the reflection coefficients of the scatterers are modeled after a Gaussian distribution with a certain average value and a standard deviation of choice. Consequently, the scatterers' movement, that dictates the fading's phase values, follows an uniform distribution, with a particular amplitude of motion. The depolarization angles also follow a Gaussian distribution for a specific average value and standard deviation, changing within time slots for each scatterer.

The expression for calculating the $h_{ij_{MP}}$ component of the H matrix for a particular scatterer s is presented in Equations 2.24 to 2.27. In structure it is similar to the LOS calculation but it adds the time varying components mentioned above and also, to obtain the full value of $h_{ij_{MP}}$, the contributions of all S scatterers must be sumed.

$$\begin{aligned} h_{11_{MP}}(t,S) = \Gamma_y(t,S) E_{0y}^{V}(\theta_{MP}^{UE}, \varphi_{MP}^{UE}) E_{0y}^{Y}(\theta_{MP}^{BS}, \varphi_{MP}^{BS}) \cos\gamma(t,S) \frac{e^{-jkd_{11_{MP}}(t,S)}}{d_{11_{MP}}(t,S)} + \\ \Gamma_x(t,S) E_{0x}^{V}(\theta_{MP}^{UE}, \varphi_{MP}^{UE}) E_{0y}^{Y}(\theta_{MP}^{BS}, \varphi_{MP}^{BS}) \sin\beta(t,S) \frac{e^{-jkd_{11_{MP}}(t,S)}}{d_{11_{MP}}(t,S)}; \end{aligned} \tag{2.24}$$

$$\begin{aligned} h_{21_{MP}}(t,S) = \Gamma_x(t,S) E_{0x}^{V}(\theta_{MP}^{UE}, \varphi_{MP}^{UE}) E_{0x}^{X}(\theta_{MP}^{BS}, \varphi_{MP}^{BS}) \cos\beta(t,S) \frac{e^{-jkd_{21_{MP}}(t,S)}}{d_{21_{MP}}(t,S)} + \\ \Gamma_y(t,S) E_{0y}^{V}(\theta_{MP}^{UE}, \varphi_{MP}^{UE}) E_{0x}^{X}(\theta_{MP}^{BS}, \varphi_{MP}^{BS}) \sin\gamma(t,S) \frac{e^{-jkd_{21_{MP}}(t,S)}}{d_{21_{MP}}(t,S)}; \end{aligned} \tag{2.25}$$

$$\begin{aligned} h_{12_{MP}}(t,S) = \Gamma_y(t,S) E_{0y}^{H}(\theta_{MP}^{UE}, \varphi_{MP}^{UE}) E_{0y}^{Y}(\theta_{MP}^{BS}, \varphi_{MP}^{BS}) \cos\gamma(t,S) \frac{e^{-jkd_{12_{MP}}(t,S)}}{d_{12_{MP}}(t,S)} + \\ \Gamma_x(t,S) E_{0x}^{H}(\theta_{MP}^{UE}, \varphi_{MP}^{UE}) E_{0y}^{Y}(\theta_{MP}^{BS}, \varphi_{MP}^{BS}) \sin\beta(t,S) \frac{e^{-jkd_{12_{MP}}(t,S)}}{d_{12_{MP}}(t,S)}; \end{aligned} \tag{2.26}$$

$$\begin{aligned} h_{22_{MP}}(t,S) = \Gamma_x(t,S) E_{0x}^{H}(\theta_{MP}^{UE}, \varphi_{MP}^{UE}) E_{0x}^{X}(\theta_{MP}^{BS}, \varphi_{MP}^{BS}) \cos\beta(t,S) \frac{e^{-jkd_{22_{MP}}(t,S)}}{d_{22_{MP}}(t,S)} + \\ \Gamma_y(t,S) E_{0y}^{H}(\theta_{MP}^{UE}, \varphi_{MP}^{UE}) E_{0x}^{X}(\theta_{MP}^{BS}, \varphi_{MP}^{BS}) \sin\gamma(t,S) \frac{e^{-jkd_{22_{MP}}(t,S)}}{d_{22_{MP}}(t,S)}; \end{aligned} \tag{2.27}$$

When considering MP, the distance between the UE and the BS through scatterer S ($1 < S < 15$), $d_{ij_{MP|S}}$, represented in Figure 2.26 b), is defined as the sum of distances A_{UEi} to S and S to A_{BSj},

as seen in Equation 2.28. Also, the definition of the observation angle changes when scatterers are involved. As represented in Figure 2.29, from the UE perspective, θ_{MP}^{UE} and φ_{MP}^{UE} are the directions in which the UE sees S, while from the BS perspective, θ_{MP}^{BS} and φ_{MP}^{BS} are the directions in which the BS sees S.

$$d_{ij_{MP|S}} = d_{A_{UEi} \to S} + d_{S \to A_{BSj}}; \tag{2.28}$$

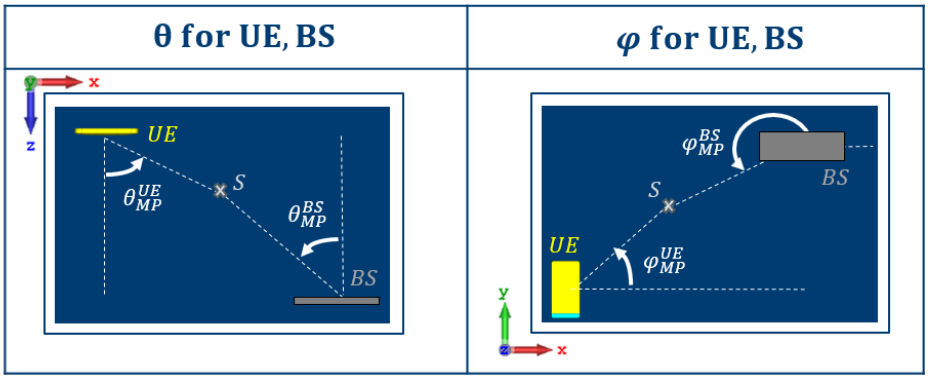

Figure 2.29: Measurement notation in space of $(\theta^{UE}, \varphi^{UE})$ and $(\theta^{BS}, \varphi^{BS})$ for MP.

Once both the LOS and MP components are defined, the channel matrix is obtained by summing both $h_{ij_{LOS}}$ and $h_{ij_{MP}}$ into the final parameter h_{ij}, as represented in Equation 2.29.

$$\left[H\right] = \begin{bmatrix} h_{11_{LOS}} + h_{11_{MP}} & h_{21_{LOS}} + h_{21_{MP}} \\ h_{12_{LOS}} + h_{12_{MP}} & h_{22_{LOS}} + h_{22_{MP}} \end{bmatrix} \tag{2.29}$$

2.3.3 Phone rotation

Phone rotation is a major factor that affects the MIMO channel performance, since it directly influences the gain values used in the H matrix calculation. While using the phone, the user will change its orientation relative to the base station. By rotating the phone, its original vertical V or horizontal H polarization will change. Let's say that the phone is in its initial position, in the xy plane but tilted 45^o. Before, the polarization of A_{UE1} was orthogonal to the polarization of A_{BS2}. However, when the tilting occurs, the A_{UE1}'s polarization will be closer to the A_{BS2} and, therefore, some of the signal transmitted by A_{UE1} will now be received by A_{BS2} as well. Depending on how much the phone is rotated, this effect can be minimized or maximized, affecting the MIMO channel's performance.

Therefore, in order to grasp the full effect of UE rotation in the MIMO channel, it is important to observe the rotation in all 3 axis, x, y and z. To mimic that behaviour, a rotation motion was added to the phone, using CST, to create its own Local Coordinate System (LCS) that differs from the Global Coordinate System (GCS) dictated by the base station, that is static in time. CST's Farfield plot properties allow for LCS selection (also called Working Coordinate System in CST, or WCS) for radiation pattern observation. This means that using one radiation pattern calculation,

it is possible to mimic another phone position with respect to the reference axis frame and extract the corresponding E-field data to use in the simulator for the H matrix construction.

For example, Figure 2.30 shows the radiation pattern calculation for $\psi = 90^o$ farfield plot of a linear four element PBS array integrated in the form factor represented in the global coordinate system. However, according the simulator's GCS, the radiation pattern maximum gain is initially directed to +z axis, the opposite direction of the maximum in the original radiation pattern simulated in CST. By selecting the (x', y', z') coordinate system from Figure 2.31 a) it is possible to obtain the radiation pattern information of the phone with z' pointing to the base station direction. This eliminates the need to repeat the simulation for different phone orientations.

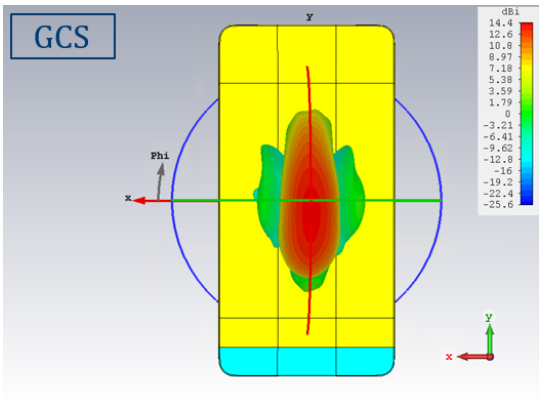

Figure 2.30: Global coordinate system established in the CST simulation.

The same process can be applied to perform phone tilting in any direction. For example, Figure 2.31 b) represents the WCS to be used in order to recreate a 45^o tilt in the xy plane.

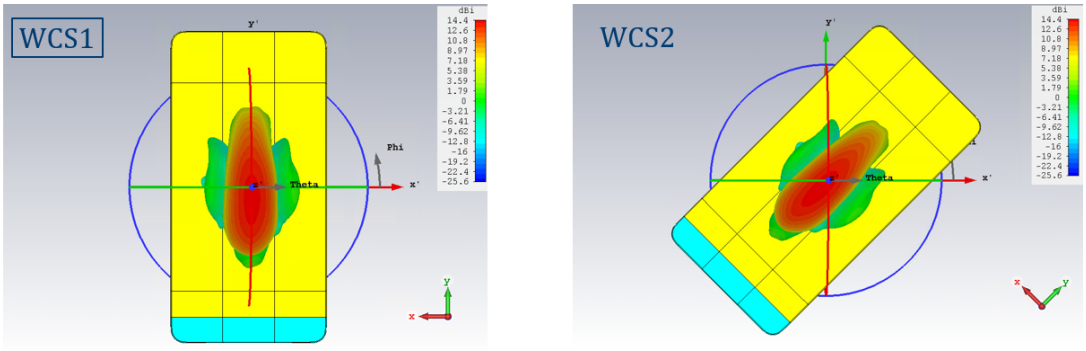

a) b)

Figure 2.31: Working coordinate systems; a) WCS 1 - 180^o rotation in zx plane; b) WCS 2 - 45^o tilt in the xy plane.

Therefore, 18 phone positions were chosen, separated by a 45^o rotation motion in all three axis. These positions are meant to represent the range of motion of the mobile phone, both for the phone alone and the phone with the user's hand included, as can be seen from Figure 2.32. The sphere

over which the positions are spread over is merely representative, so that the the orientations of each UE position were clear. Actually, the phone center remains in the same coordinates (x, y, z)=(0,0,0) but rotates around the three axis as can be seen from Figures 2.33 a) and 2.33 b).

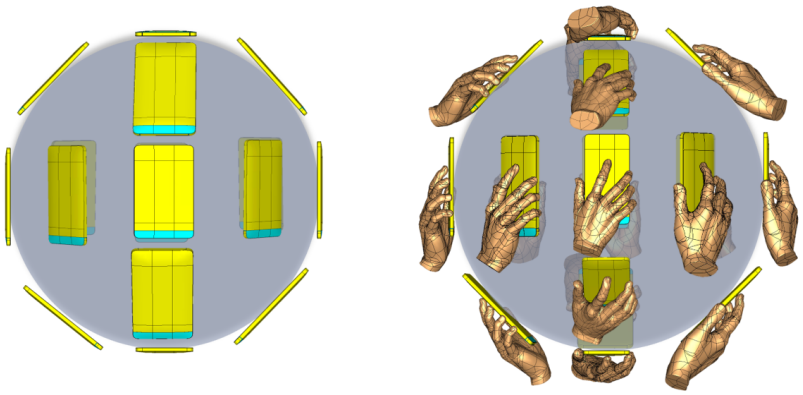

Figure 2.32: Eighteen different phone orientations without and with the User's hand for the UE coordinate (0,0,0); a)Antennas implemented in the form factor; b) Antennas implemented in the form factor with a TM grip.

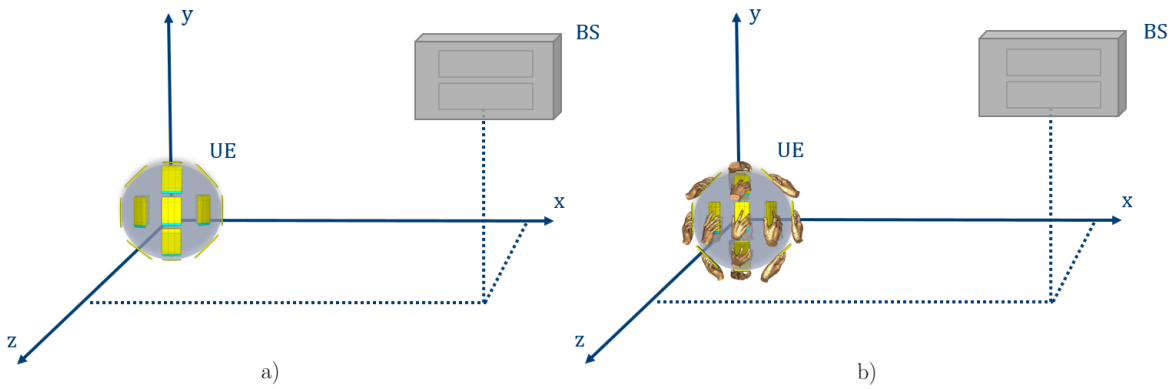

Figure 2.33: Eighteen different phone orientations relative to the BS for the same UE coordinate (0,0,0); a) Antennas integrated in the form factor; b) Antennas integrated in the form factor and gripped by a hand.

2.3.4 Antenna array coupling

Another potential influencing factor on the MIMO channel performance is the array coupling between arrays in the same device (within the UE or within the BS). By definition, antenna coupling describes the process by which an antenna will absorb part of the energy and interact with a nearby antenna. If the coupling between the two arrays is high that means that the arrays are too close and

there is energy waste that could be applied into transmitting the signals. Even more important, if part of an array's energy goes into the other antenna, part of its information also gets misdirected, originating cross-talk. So, right in the transmission process, both arrays are already sending mixed information. Since space is a subject without much room for discussion when it comes to mobile phone form factor, it is important to study how close the arrays can be placed while preventing the coupling from being too high and ruining the link.

CST provides the coupling information between antenna elements of an array. However, the interest of this study lies in the coupling value between adjacent arrays. In order to model it correctly, the array feeding network must be defined, so that each array is represented by one single port (instead of the four element ports for each array). It is the coupling between the single port of each array that matters for the analysis. Modeling the feeding network together with the arrays in the 3D simulator consumes too much resources and time. To go around this, a circuit analysis tool from CST was used, in the Schematics tab. CT's Schematics tab is a feature that shows the circuit scheme of the dissertation developed in the 3D tab. This allows for circuitry manipulation, such as adding ideal microwave RF components, ideal transmission lines or even import S-parameter files.

After the circuit is designed, all there is left to do is to select the ports to be analyzed and the type of circuit task needed to be performed.

Figure 2.34 shows the Schematics tab of the dual polarized, four element linear PBS array implemented within the form factor. There is a single block with eight outputs, representing the eight feeding pins implemented in the 3D tab showed earlier in Figure 2.20. In order to get the coupling values between both arrays of these dual polarized patch, two power dividers are added to connect, respectively, the even and the odd pairs, to two single ports, to represent A_{UE1} and A_{UE2}, as seen in Figure 2.35.

However, because the coupling also depends on the beam that each array forms, there will be different values of coupling for the same array pair. Since each array has the ability to switch between 5 beams, there are twenty five coupling values between the arrays that must be assessed. In order to do so, the beam steering effect must be added in the Schematics tab. That can be accomplished using a Touchstone file generated manually outside of CST with the weights for each steering direction, similarly as it was done in the coverage study section. The different blocks are the phase shifts added to each antenna element of the array, as also displayed in Figure 2.35.

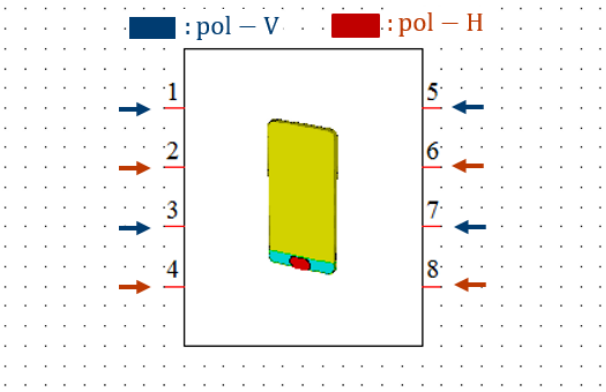

Figure 2.34: CST's default schematic of a file containing the PBS array in the smartphone.

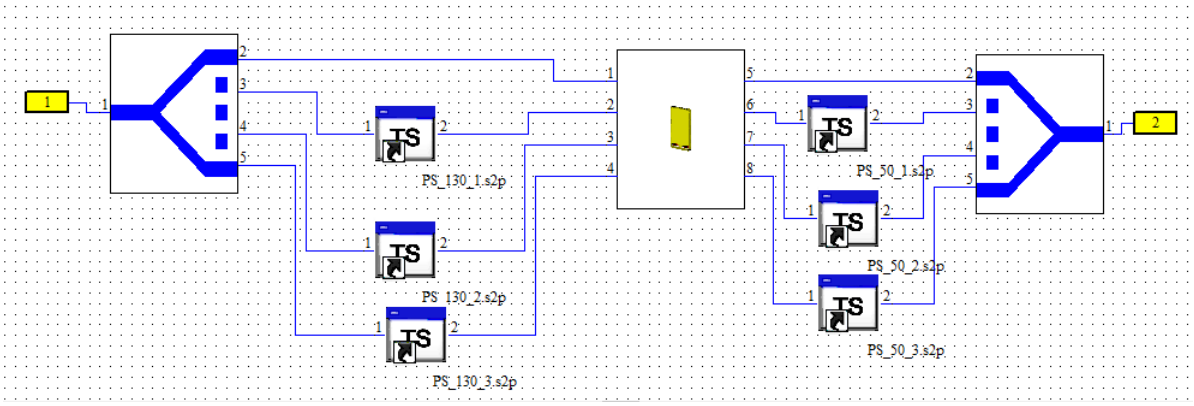

Figure 2.35: CST circuit analysis model for the two PBS arrays in the form factor. It shows the power splitters and phase shifters to perform BF for $\psi_{A_{UE1}} = 130^o$ and $\psi_{A_{UE2}} = 50^o$.

Using this process a 2x2 S-parameter matrix, S will be obtained, as can be seen from Equation 2.30. The diagonal elements are usually called reflection factors, because they reveal how much of the energy radiated from one array is reflected and needlessly delivered back to that same array, indicating how well matched the array actually is. The cross elements from the S matrix represent the mutual coupling between arrays, the information that is relevant here. Ideally, all entries of this S matrix should be small, but reality is that the tight space in the mobile phone and influence form the structure may increase the coupling, degrading the antenna's performance and ,therefore, the MIMO channel quality.

$$\left[S\right] = \begin{bmatrix} s_{11} & s_{12} \\ s_{21} & s_{22} \end{bmatrix} \tag{2.30}$$

Once S is calculated in CST, it is then extracted as an ASCII file as well and used to obtain the transmission matrix T. This matrix accounts for how much of a given signal is transmitted through the wrong antenna. The contributions from each array in the transmitted signal are described down in Equation 2.31 and Equation 2.32, where E_{T1} the signal transmitted from the first array and E_{T2} is the signal transmitted through the second array.

$$E_{T1} = \sqrt{1 - s_{11}^2} E_1 + s_{12} E_2; \tag{2.31}$$

$$E_{T2} = s_{21} E_1 + \sqrt{1 - s_{11}^2} E_2; \tag{2.32}$$

$$\left[T\right] = \begin{bmatrix} \sqrt{1 - s_{11}^2} & s_{12} \\ s_{21} & \sqrt{1 - s_{22}^2} \end{bmatrix} \tag{2.33}$$

If the arrays in the UE are too close, given the lack of space for hardware in the mobile phone, it might happen that the coupling values produce unacceptable cross-talk reducing MIMO gain.

However, fixing the spacing between arrays is only possible for the MBS, since the two PBS arrays are actually within a single structure, serving the dual polarization purpose.

2.3.5 Beam pair link selection

Once the H matrix is calculated and all antenna parameters are accounted for, it is time to evaluate the channel's performance using the channel matrix. As mentioned before, the H matrix has 3 dimensions in this numerical implementation, as seen inf Figure 2.36, where the first two are the 2×2 h_{ij} parameters and the third one belongs to the C=25 beam combinations that come from the A_{UEi}'s and the A_{BSi}'s available beams. As mentioned before, b=5, with the chosen beams of $\psi_{UE/BS} = 50^o$, $\psi_{UE/BS} = 70^o$, $\psi_{UE/BS} = 90^o$, $\psi_{UE/BS} = 110^o$, $\psi_{UE/BS} = 130^o$. No more beams were considered in this study to contain computation time.

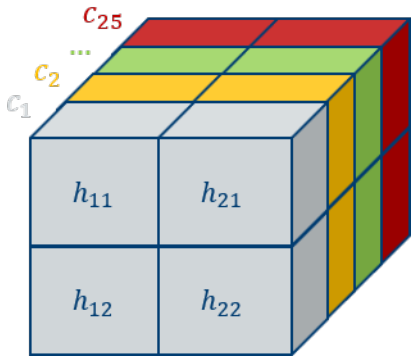

Figure 2.36: Schematic representation of the 3 dimensional H matriz.

In order to obtain the best achievable channel performance, a conscious choice must be made to select the most favorable beam from each array or, in other words, the best combination Ck between the UE arrays and the BS arrays. In this thesis, two different choice criteria were established according to the antenna family under evaluation. For the PBS, since it is a SM transmission technique, the beam selection is led through a compromise between the best received power criteria and the best channel's CN. For the MBS, if used as a SISO channel, a best received power choice criteria is sufficient.

For both approaches, four power matrices are needed to help narrow down the beam pairing for the UE and the BS for transmission. Because there are two arrays in each communication end, four power matrices are generated: $P11$ (power matrix for the communication link connecting A_{UE1} and A_{BS1}), $P12$ (power matrix for the communication link connecting A_{UE1} and A_{BS2}), $P21$ (power matrix for the communication link connecting A_{UE2} and A_{BS1}) and $P22$ (power matrix for the communication link connecting A_{UE2} and A_{BS2}), all represented in Figure 2.37.

Each of these is a 5×5 matrix that houses, for each time slot t, the power values of all twenty five beam combinations, Ck for that specific link, as displayed in Figure 2.38.

The $P21$ matrix for the linear, four element, PBS array is represented in Figure 2.39 as an example. The twenty five entries are the power levels that result from combining the five beams from $A_{UEi=2}$ with the 5 beams from $A_{BSj=1}$.

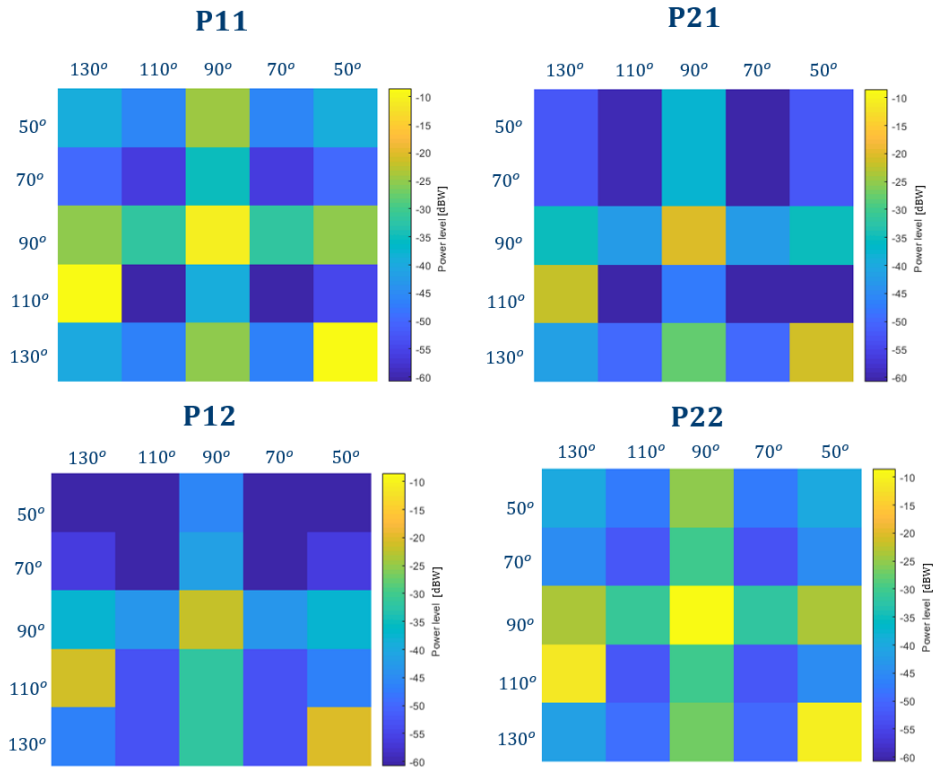

Figure 2.37: Power matrices for each channel: P11 for h_{11}, P21 for h_{21}, P12 for h_{12} and P22 for h_{22}.

2.3.5.1 Selection criteria for MIMO

As mentioned above, one of this transmission technique's main selection criteria, besides comparing received power, is the H matrix's CN. This is a key metric to evaluate a MIMO system's ability to perform SM and, therefore must be thoroughly explained. In a 2×2 SM system, as portrayed in Figure 2.20 and Figure 2.22 , s_1 and s_2 are two separate data streams, carrying different information, that are being transmitted by two arrays to later be received through two other arrays in the form of r_1 and r_2, each of them with their own noise sources n_1 and n_2. This process can then be described using linear equations, such as Equation 2.34 to Equation 2.36.

$$r_1 = h_{11}s_1 + h_{21}s_2 + n_1; \tag{2.34}$$

$$r_2 = h_{12}s_1 + h_{22}s_2 + n_2; \tag{2.35}$$

$$\begin{bmatrix} r_1 \\ r_2 \end{bmatrix} = \begin{bmatrix} h_{11} & h_{21} \\ h_{12} & h_{22} \end{bmatrix} \begin{bmatrix} s_1 \\ s_2 \end{bmatrix} + \begin{bmatrix} n_1 \\ n_2 \end{bmatrix} \tag{2.36}$$

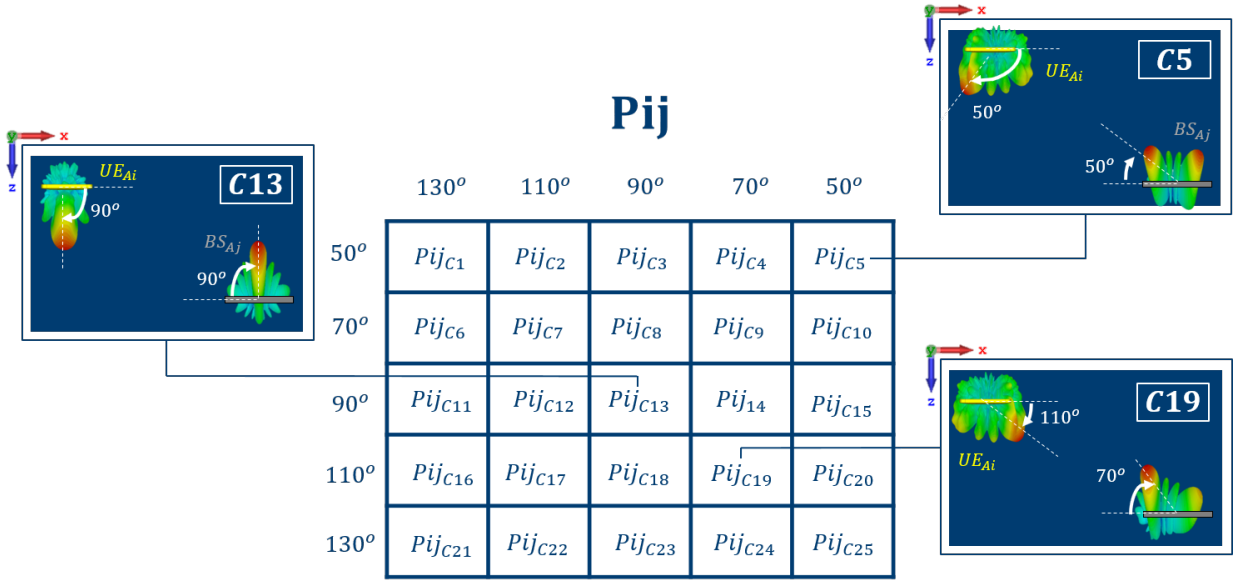

Figure 2.38: General representation of a power matrix. Each line represents one BS beam direction and each column represents on UE beam direction.

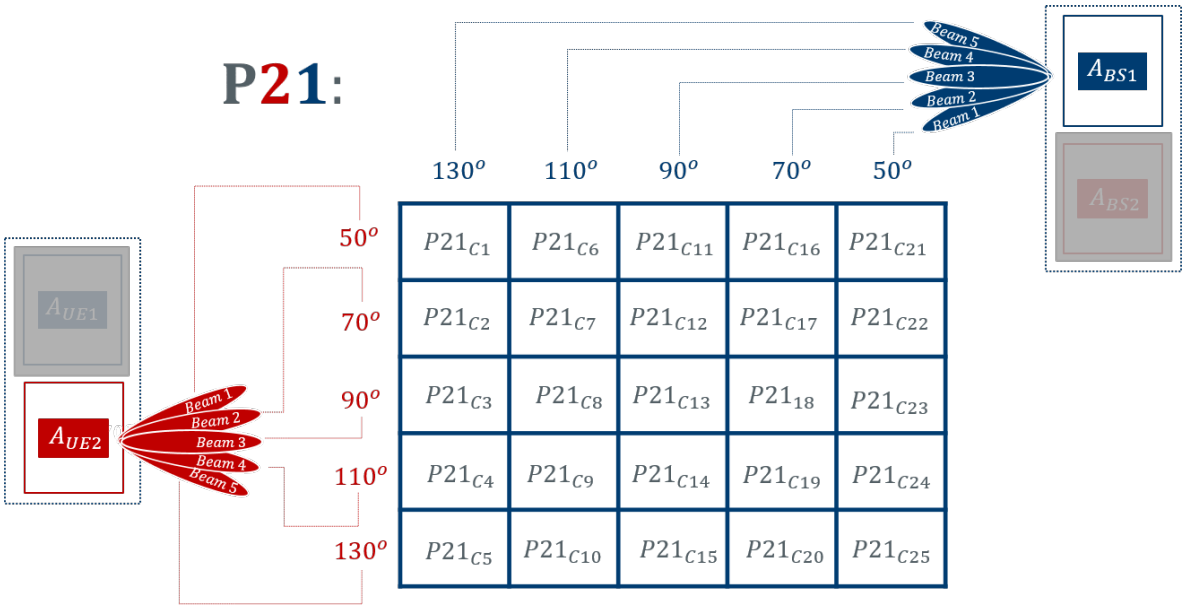

Figure 2.39: Example of a P21 power matrix for the linear, four element, PBS array.

The receiver end is responsible for solving the equation - it must find s while only knowing r. In order to do so, the H matrix has to be obtained using channel estimation techniques based on channel state information (CSI) that the signal carries. Once the H matrix is estimated, the evaluation process starts: if the equation is solvable, then SM can be used as a transmission technique. Otherwise, if the receiver cannot solve the equation, that means it can't tell both

signals apart and, therefore, there is no point in performing SM [40]. Indicators such as the H matrix's CN and rank will be the figures of merit for this problem.

The CN of a matrix describes how subject the solution of the equation is to errors in the data input (such as noise resulting from channel correlation) or, in other words, how well can the linear equation be solved. Equation 2.37 shows how to obtain the channel's CN using the H matrix's singular values, σ.

$$CN = \frac{\sigma_{max}}{\sigma_{min}} \geq 1; \tag{2.37}$$

Equation 2.38 describes how to obtain these singular values, where U is HH^H and V is HH^H. H^H is the hermitian operator applied to the H matrix and Σ is the singular value matrix, shown for a 2x2 system in Equation 2.39. Σ is a matrix containing the single values in the diagonal entries and 0 in the remaining entries. It is important to mention that, with this decomposition, the crosstalk does not disappear, rather gets stored away in the U and V matrices [41].

$$H = U\Sigma V^H; \tag{2.38}$$

$$\left[\Sigma\right] = \begin{bmatrix} \sigma_1 & 0 \\ 0 & \sigma_2 \end{bmatrix} \tag{2.39}$$

In other words, these equations translate the decomposition of the channel matrix into two separated crosstalk free transmissions (SISO) channels, with transmission coefficients σ_1 and σ_2. This process is called Singular Value Decomposition (SVD) of the channel matrix and its mechanism is described in Figure 2.40.

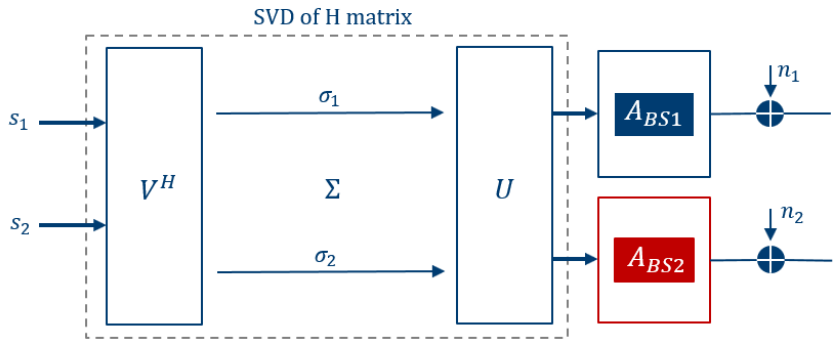

Figure 2.40: Illustration of the single value decomposition process of a matrix.

From equation 2.37 it is clear that the ideal scenario would be to have similar amplitude for both singular values. If one of them is significantly smaller, that means one of the signals is much weaker that the other, which would then make it hard to decode. The closer this ratio is to 1 (0 dB)

the better are the chances of the receiver being able to separate the two streams of information. Consequently, if this ratio is really high, there is really no point in using SM.

The reference values for the CN are between 0 to 10 dB, while anything above 20 dB is considered unusable for MIMO [40]. In linear units, this would mean that the matrix's CN should be somewhere between 1 and 3.2 in order for SM to be optimal and anything above 10 would be useless. This is the criteria that will be used to decide between SISO and MIMO for the MBS antenna solution. If $CN < 10$ then the MBS should proceed with the MIMO mode. Otherwise, it should shift for SISO.

Similarly, the rank of a matrix is measured by its number of non zero singular values. In this context, it dictates how many data streams can be spatially multiplexed on the MIMO channel being evaluated. Therefore, the rank can never be greater than the matrix's dimension and, for this example, only two option are possible: either $rank = 2$ and SM is a possibility, or $rank = 1$ and MIMO is out of question. However, even if CN is very large, as long as it has two different singular values, the rank will always be 2 and, therefore it is not a sensitive enough indicator of SM quality as the CN.

However, even if a channel CN is very good, if the signal intensity is not strong enough, then the transmission cannot be successfully carried out. Thus, it is also important to ensure a high enough received power level along with an adequate CN: whichever beam-pair, UE-BS, has the highest power and the CN has the biggest chance of providing the highest channel capacity and, therefore, successfully delivering the signal.

In the case of the 2×2 MIMO, the focus is on the channel rather than the transmission scheme. It is not relevant to determine which 2 transmission channels get picked to transmit the two signals. In fact, it is more useful to know which beam-pair combination, out of the 25 available, would provide the best conditions for SM. For this, all four power matrices are summed into one big 5x5 power matrix P, seen in Figure 2.41, that will give a general but accurate feel of the power distribution over the different beam combinations. Then, an algorithm based on power and the CN of the matrix is used to select the best entry Ck, indicating the beam pair link combination of choice for the communications.

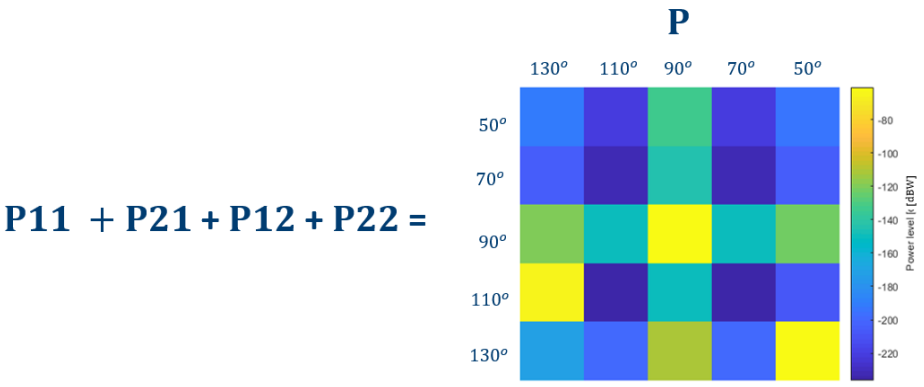

Figure 2.41: Creation of the P power matrix as the sum of all the channel's power matrices.

As depicted in Figure 2.42, this algorithm locates the entries that detain power values between

$P_{max} - 3dB < P_{ij} < P_{max}$, corresponding to the highest available power amongst all beam combinations. The pre-selected entries have their associated CN values that will be compared, in order to narrow the choice down to one of the entries. The chosen Ck entry will, thus be the one will the lowest CN value. In the case described in Figure 2.42, the maximum power registered is 134.3 dBW in the $110^o - 130^o$ entry. Besides that one, two more entries are selected based on their power level, $90^o - 90^o$ and $130^o - 50^o$. Finally, the beam-pair link that is chosen is the $90^0 - 90^o$, because it presents the CN value that is closest to 1. This beam-pair combination chosen will offer the best MIMO performance.

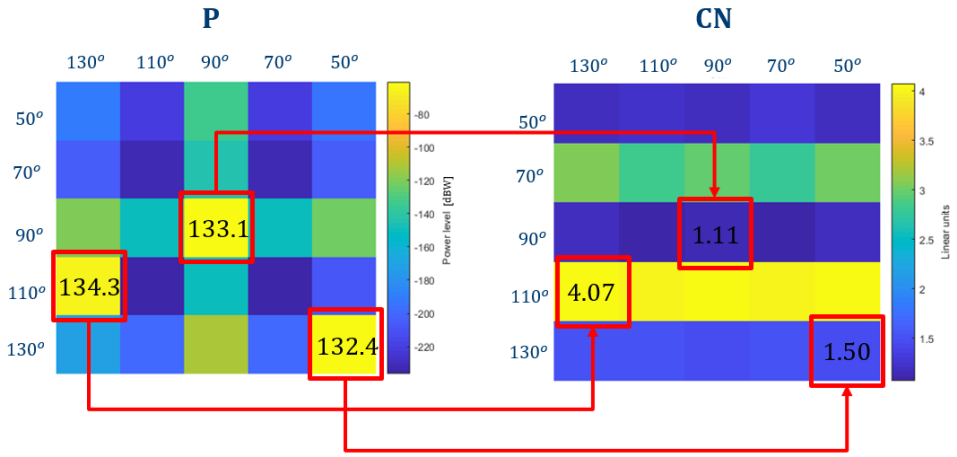

Figure 2.42: Beam selection criteria for the PBS: highest received power + lowest condition number combination.

2.3.5.2 Selection criteria for SISO

In the case of $CN < 10$ and or $r = 1$, the MBS will shift from MIMO mode to SISO mode. For SISO, the beam pair selection is simpler. There is only one stream s_1 to be delivered, so all that is need is to select which channel to carry out the transmission through and which beam combination will offer the best transmission conditions. This information can easily be obtained by choosing a single entry, the one with the highest power value, among the four power matrices, as indicated in Figure 2.43.

It is important to mentioned that the beam selection is affected by outside variables such as the location and orientation of the UE relative to the BS. In a LOS scenario, it is only natural that, if both the UE and the BS are front-to-front, the beam-pair with the best conditions for transmission will most likely be $\psi_{UEBS} = 90^o$. However, if the UE and BS are misaligned, the answer will probably lie in the beams further away form the center of the array. Once the beam pair is selected, follows the channel metric calculations.

2.3.6 MIMO channel capacity calculation

In order to evaluate the MIMO channel, and to enable a comparison process between antenna families one must define a metric for comparison. Since an important factor in communications is

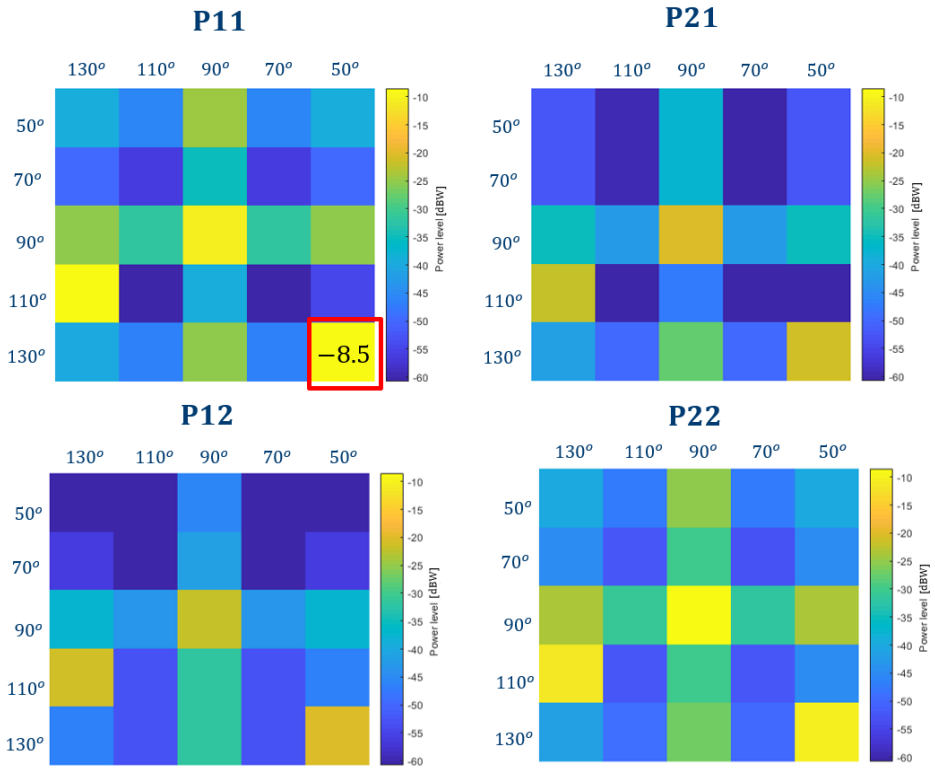

Figure 2.43: Beam selection criteria for the MBS: highest received power.

the amount of information that a channel can hold, calculating the channel capacity seems to be the most fitting metric that can be established. Equation 2.40 expresses Shannon's capacity theorem. N_r and N_t represent, respectively, the number of transmitting and receiving antenna arrays of the system, while I_{Nr} is a $N_r \times N_r$ identity matrix, H_n is the normalized channel matrix of the system, calculation in Equation 2.41, where T is the number of slots used, and SNR is the receiver's signal to noise ratio.

$$C = log_2(det\ [I_{Nr} + \frac{SNR}{N_t} H_n H_n^H])\ bit/s/Hz; \tag{2.40}$$

$$H_n = \frac{H}{\sqrt{\frac{1}{N_r N_t T} \sum_{N_r} \sum_{N_t} \sum_{T} H H^H}}; \tag{2.41}$$

It is important to mention that this calculation of C is the best case scenario value of capacity, since it only takes into consideration the channel conditions and not processes such as the modulation/demodulation and coding/decoding of the signal to be ideal.

Although Equation 2.40 can be applied for both MIMO and SISO channel capacity, the parameters are used differently. For a 2×2 MIMO scenario, N_t=N_r=2 and H is a 2×2 matrix. For a SISO scenario, N_t=N_r=1 and H matrix is reduced to a single h element.

Also something important is the way the SNR is calculated for both scenarios. SNR is the ratio between the signal's power and the noise in the receiver, as described in Equation 2.42.

$$SNR = P_{signal}/P_{noise}; \tag{2.42}$$

In a lot of MIMO studies the SNR is fixed at a reasonable value, generally 10 to 20 dB. However in this simulator, the SNR is calculated over time and is susceptible to the environment characteristics and distance between the antennas. For this SNR calculation, the noise power is considered to be the receiver's floor noise value. The floor power noise is the sum of all noise sources and unwanted signals within a system. It is the power reference value that an upcoming signal has to top in order to be detected by the receiver.

The source available noise power, N_{sa}, and the receiver's input referred noise define the receiver's noise floor. N_i in logarithmic scale, is given by the noise figure. The noise figure, NF, is a figure of merit for receiver noise performance and its value is usually placed between 2 to 10 dB. The N_{sa} calculation is described in Equation 2.43, where K is the Boltzmann constant, T is the equivalent noise temperature, that was considered 290 K, and B is the channel's bandwidth [42].

$$N_{sa}(dBm) = KTB = -174 + 10\log B; \tag{2.43}$$

Therefore, the receiver's noise floor, P_{noise}, is obtained with Equation 2.44, by performing the sum of N_{sa} and N_i.

$$P_{noise}(dBm) = N_{floor} = 10log(N_{sa} + N_i) = -174 + 10\log B + NF; \tag{2.44}$$

In respect to the signal's power calculation, P_{signal} is obtained from the H matrix by performing a link budget study. Using a variation of Friis's equation depicted in Equation 2.45, the received power, P_rij, is calculated for all h parameters in the form of Pij_{signal}. In this equation, P_t is the transmitter's power.

$$P_rij = Pij_{signal} = P_t|h_{ij}|^2\Big(\frac{\lambda}{4\pi}\Big)^2; \tag{2.45}$$

For MIMO the final value of Pr is the mean of the four $Prij$, as seen in Equation 2.46, while for SISO there is only one h parameter and thus only one value of P_r, as discriminated in Equation 2.47.

$$P_r = P_{signal|PBS} = \frac{1}{4}\sum_{i=1}^{2}\sum_{j=1}^{2} Pij_{signal}; \tag{2.46}$$

$$P_r = P_{signal|MBS} = Pij_{signal}; \tag{2.47}$$

From the calculations listed above, results a time distribution of CN, SNR and C, for each of the 18 smartphone rotation positions, along T time slots. By collecting the representative channel capacity values of each of the 18 positions, using the distribution's median value, one could construct a capacity Cumulative Distribution Function (CDF) that would express how much this channel metric is affected by the change in orientation of the smartphone in relation to the BS.

2.3.7 Summary

This chapter presented the overall methodology to evaluate the mm-Wave antennas and their contribution to MIMO performance for smartphones in the context of 5G at 39 GHz. Some important aspects of antenna design and implementation were pointed out and the evaluation process was described:

- An adequate mm-Wave antenna design method and implementation was established in CST, including a model of a smartphone form factor and the user's hand grip;
- A Matlab script was developed to obtain the codebook entries and reproducing any radiation pattern automatically using antennas ASCII files from CST. Some extra functionalities were also added, like the visualization of the codebook envelope and the tunable phase shifter characteristics.
- A function was idealized to evaluate each antenna's ability to provide coverage while maintaining an acceptable gain value.
- An graphic user interface for Antenna Pattern and Codebook Analysis was developed as a result of the work developed previously.
- A 3D geometric discrete scattering channel model was implemented to recreate any type of scenario for mm-Wave propagation using realistic antenna characteristics and implementing the studies made above regarding form factor influence, BF, user inherent body blockage, user induced phone rotation. It will be used to determine the channel's performance for each antenna type when the UE is subjected to different environment scenarios, orientations in space and hand grips.

The next two chapters use the methods proposed to perform actual studies.

Chapter 3

Antenna study

This chapter gathers all the results regarding the antenna families' analysis. First, reference results for the antenna families' radiation patterns are established, both in single and array form in free space. It is also studied the degree of influence that the form factor of the smartphone has on the original radiation patterns of the antenna, as well as the effects of the human body when in proximity of the radiating antennas for 39 GHz. Finally, a CS is performed to assess how much coverage can each of the antenna families provide without giving up a certain value of maximum gain.

3.1 Antenna disturbance factors

3.1.1 Free space reference

The PBS single antenna was implemented in CST with a size of 2.43×2.43 mm, on top of a square ground plane and a 0.5 mm thick Rogers RT 5880 substrate, with a loss tangent of 0.0009. The metallic ground and patch are made of copper with an electrical conductivity of 5.95 Sm^{-1}. The PBS has two discrete ports orthogonal to each other but only one of them is excited for this study, the one over the y axis.

Meanwhile, the MBS single antenna is a folded copper monopole with a height and length of 1.4×1.75 mm and its copper ground plane has dimensions 4.8×4.8 mm. However, this dimension will change once it is integrated in the phone, since the MBS uses the phone as a ground plane.

The free space radiation patterns for the PBS and the MBS antennas can be found, respectively, in Figure 3.1 a) and Figure 3.1 c). For more clarity, the see-through view of the same radiation patterns were added in Figure 3.1 b) and Figure 3.1 d), so that the antenna structure can be visible. Directivity was used, instead of gain, since the study isn't directed towards a model proposal of an antenna to be implemented, rather an antenna family. This is meant to rule out any effects of the antenna design that might interfere with the result interpretation.

For this particular ground plane dimension and antenna positioning, the Patch Based Solution (PBS) has a maximum gain of 7.72 dBi with a $\epsilon_T = 0.5103$ dB, while the PBS presents a maximum gain of 3.57 dBi and a $\epsilon_T = 0.1866$ dB. In free space these antennas have a bandwidth of, respectively, 3.758 GHz and 4.567 GHz , as can be seen in Figure 3.2 and Figure 3.3.

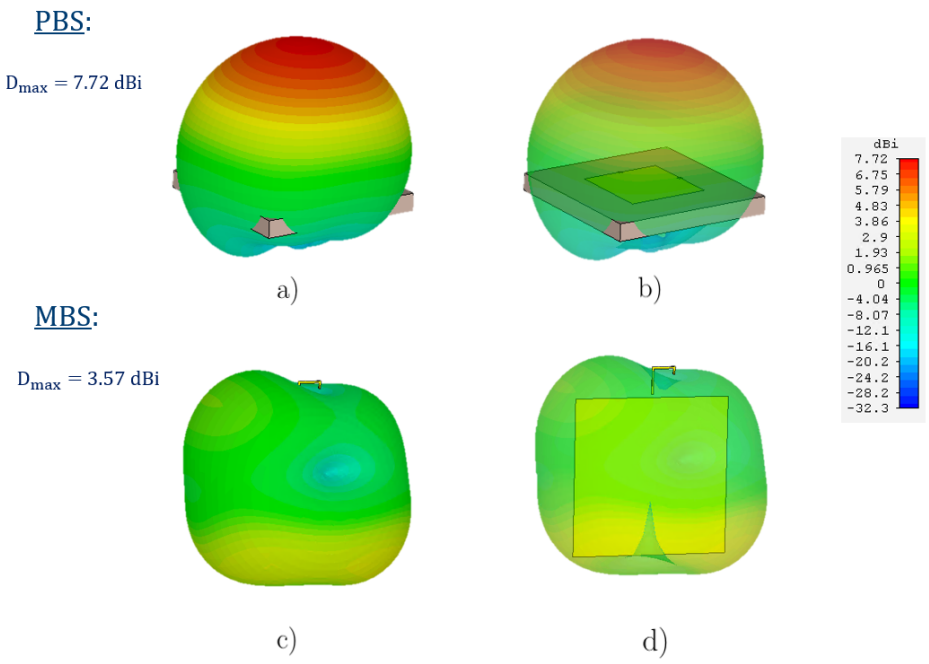

Figure 3.1: Single antennas radiation patterns; a) PBS antenna radiation pattern; b) see-through PBS antenna radiation pattern; c) MBS antenna radiation pattern; d) see-through MBS antenna radiation pattern.

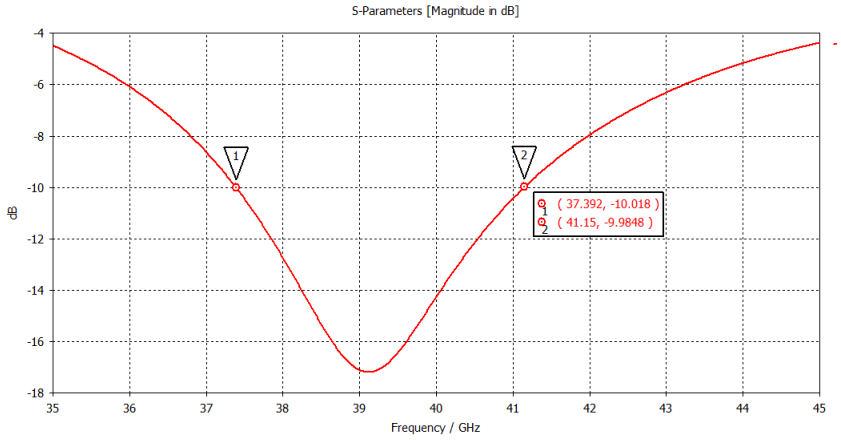

Figure 3.2: PBS antenna input reflection bandwidth.

The same antennas were used in a linear four element array configuration.

For the PBS, the array's dimensions are 24.5×6.09 mm with a spacing of 0.7λ and a mutual coupling of $s_{12|39GHz} = -10.24$ dB in free space.

For the MBS, the array's dimensions are 15.73×1.4 mm, also with a spacing of 0.7λ and a mutual coupling of $s_{12|39GHz} = -12.07$ dB in free space.

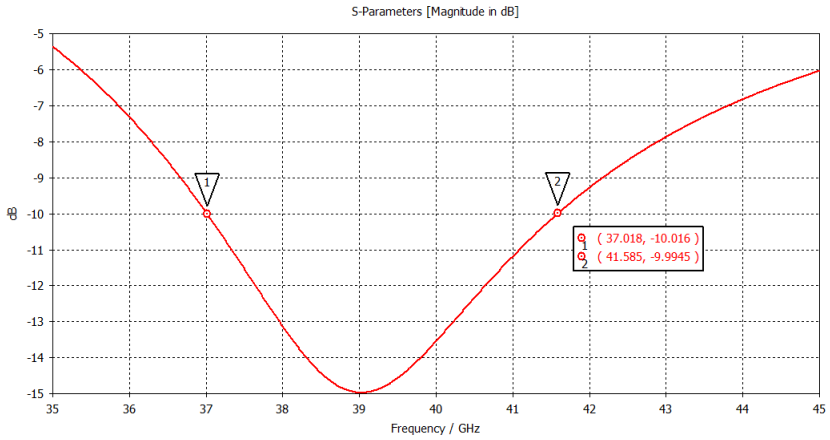

Figure 3.3: Monopole antenna input reflection bandwidth.

Figure 3.4 shows the beams are much more directive, with, approximately, $10\log_{10}(4) \approx 6$ dB increase in gain in the maximum gain direction, compared to the single antennas. With an array configuration, beam steering is possible, in the direction of the array's axis, without loosing beam shape between $\psi = 50$ to $\psi = 130^o$, with a small gain reduction of a few dBi when compared to the maximum gain at $\psi = 90^o$.

3.1.2 Smartphone influence

For the preliminary studies, to save computation time, the original form factor was truncated, remaining only its bottom half, where all the antennas are placed. As an example, Figure 3.5 represents the radiation pattern for the linear four element PBS array implemented in the phone for $\psi = 90^o$ for both the full form factor and for the truncated form factor. The plane cut was carefully chosen so that it wouldn't affect significantly the results obtained, while allowing for a smaller simulation time in a preliminary stage where a lot of the project moves forward using a trial and error approach.

Regarding the form factor's components, the metal structure of the form factor is copper, again with an electrical conductivity of 5.95 Sm^{-1}, while the substrate is an FR- 4 dielectric with a loss tangent of 0.025. The casing is made out of plastic with a tangent loss of 0.007.

The antenna arrays were implemented in the truncated form factor as seen in Figure 2.5. Figure 3.6 a) and Figure 3.6 c) show, respectively, the radiation patterns of the linear four element PBS array for $\psi = 90^o$ in the smartphone.

An important detail of the influence of the phone in the radiation patterns is that both antenna families have similar maximum gains now, with a small difference of around 1 dB, while securing a ϵ_T inferior to -1.5 dB, which is still a higher value compared to free space. This happens because the phone's chassis that encapsulates the antennas is made of metal. This material has electrical properties that influence significantly the behavior of the radiation patterns. Metals have close to infinite conductivity. Therefore the antenna's electromagnetic field won't penetrate through the metal chassis and will end up being reflected and ripple between the metal walls of the phone, hence the differences in the radiation pattern when compared to free space. For the same reasons,

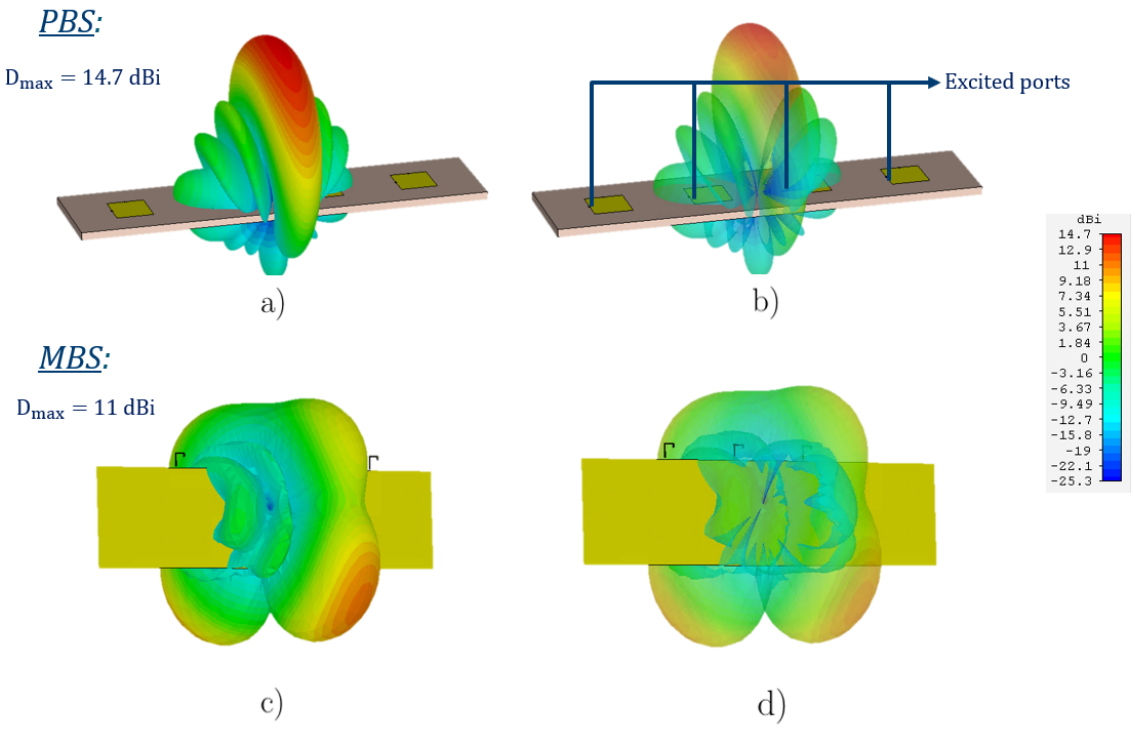

Figure 3.4: Radiation pattern of the array configurations for $\psi = 90^o$; a) PBS array radiation pattern; b) see-through PBS array radiation pattern; c) MBS array radiation pattern; d) see-through MBS array radiation pattern.

the coupling values of the antenna arrays changes. For the PBS, $s_{12|39GHz} = -10.651$ dB and for the MBS $s_{12|39GHz} = -19.22$ dB.

A representation of this propagation phenomenon can be found in Figure 3.7 for the PBS and Figure 3.8 for the MBS. These pictures portray the propagation of the E-fields over the form factor, to which a longitudinal and transversal cuts were applied so that the phenomenon can be visible. It is clear that the E-fields cannot penetrate the metal parts of the form factor, only propagating close to its surface or reflected, as expected.

In addition to the phone's chassis, more elements were added to the construction of the form factor to assess their influence on the antenna's radiation pattern. One of the chosen were Gorilla glass 5 with a loss tangent of 0.014 to add to the simulations a screen with 0.2 mm thickness. The other material was plastic for the phone's back cover, with a 0.0009 loss tangent. Before, only the bottom half of the phone had a plastic cover, the rest of the rear casing was all made out of metal. Therefore, the plastic material was used to cover the whole rear of the phone. That is why, in Figure 3.9 the phone's back is mostly blue, instead of the typical metallic bright yellow. These phone components were chosen for having a large area that could potentially cover the antennas and, ultimately, alter the radiation patterns.

Both were incorporated into the form factor, as can be seen in Figure 3.9, but didn't cause much

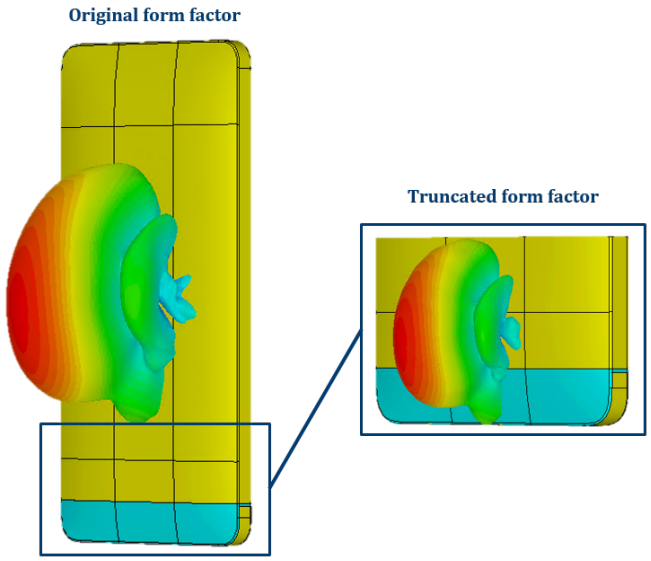

Figure 3.5: Full form factor vs. Truncated form factor: unchanged linear four element PBS array radiation pattern for $\psi = 90^o$ - phone's back side view.

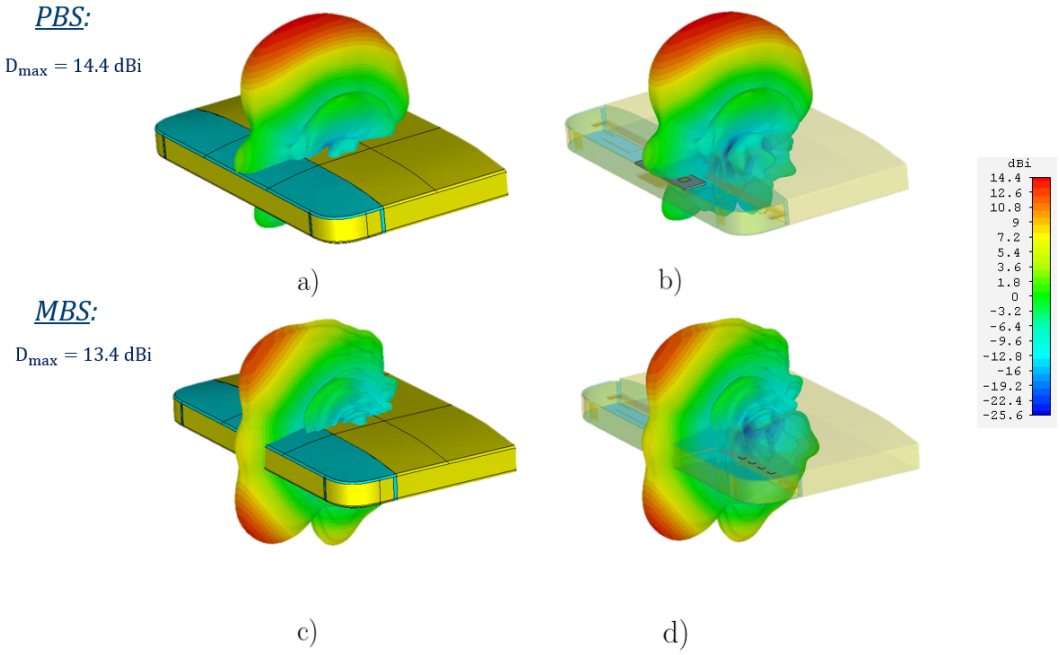

Figure 3.6: Radiation pattern for the array antennas implemented in the form factor.

disturbance to the antenna's gain or shape of the radiation pattern.This minimum disturbance is caused by a small interference between the energy that gets trapped in the material and the energy

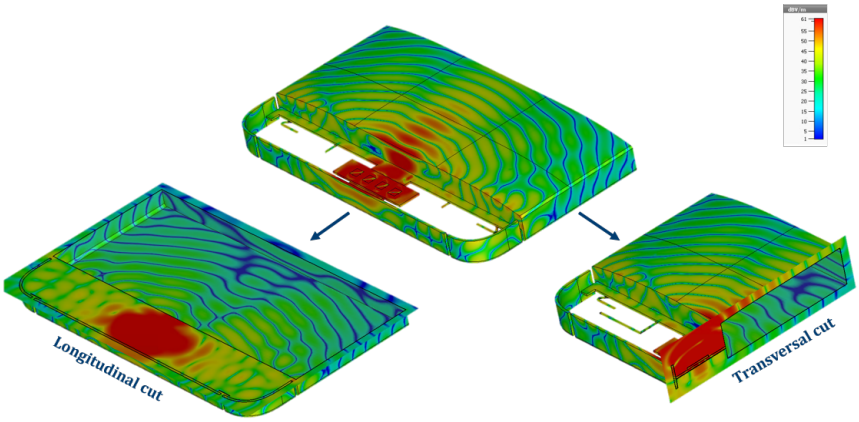

Figure 3.7: Longitudinal cut of the patch array E-field penetration in the mobile phone.

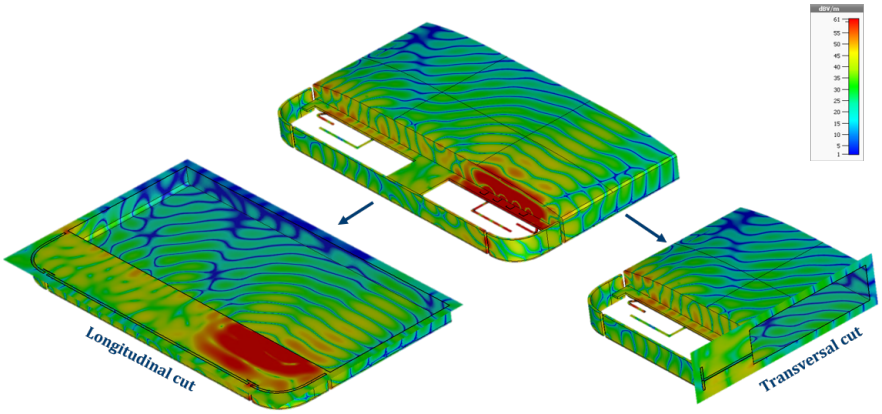

Figure 3.8: Cross cut of the monopole array E-field penetration in the mobile phone.

that radiates through that same material. This isn't so much the case for the glass, that is very thin, but more for the phone cover, as can be seen from the ripple effects of the radiation pattern on the phone's sides. Despite adding some components, the general steering property of the radiation patterns is still unaltered. This is due to the fact that the antennas were placed in the bottom of the phone. This area is characterized by a hollow metal structure encapsulated by a plastic casing that, as seen above, does not affect significantly the radiation patterns' shape.

However, if the phone structure sustains alterations that affect the amount of metal in it, the radiation pattern is likely to be modified. This is the case for bezel size reduction, a big trend in current smartphones in the market, to accommodate for bigger screens. A small bezel size, despite esthetically pleasing, requires that most of the plastic material in the bottom half of the phone be replaced with metal. Some test were conducted to see how much the PBS and MBS antenna arrays behavior would be affected. The bezel size was decrease from its original width of 14.6 mm to a mere 2.23 mm of bezel size, in order to resemble models such the Iphone X and the Samsung S9.

Figure 3.10 shows a side-by-side comparison of the PBS's radiation pattern for $\psi = 90^o$ with the original bezel size, Figure 3.10 a), and the new bezel size, Figure 3.10 b). Despite this alteration,

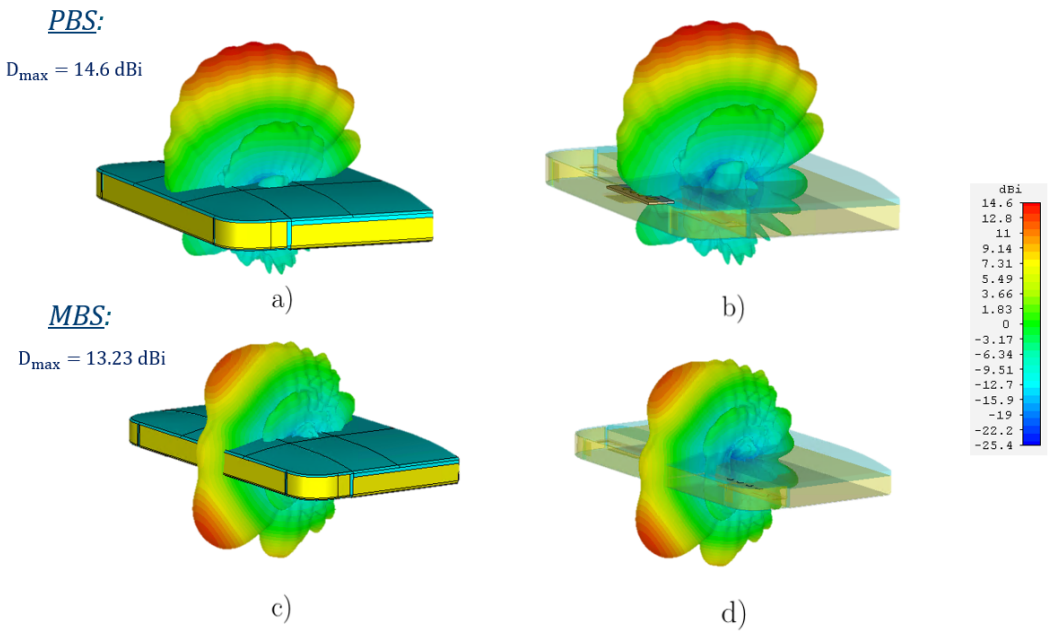

Figure 3.9: Radiation pattern for the form factor accounting glass and plastic rear cover; a) PBS array radiation pattern; b) see-through PBS array radiation pattern; c) MBS array radiation pattern; d) see-through MBS array radiation pattern.

the PBS does not seem to suffer any changes, which was to be expected. Because of the way it was implemented, the PBS radiates through the back of the phone, where the amount of metal has not changed from the original model. There was only metal added to the front of the phone, to support a bigger screen. In contrast, the MBS's radiation pattern is directed towards the bottom of the phone, radiating around it. Therefore, as shown in Figure 3.10 c), the MBS suffers from this metal addition, since it is not able able to radiate through the front phone as before, in Figure 3.10 d) loosing its main lobe.

It is worth mentioning that these bezel size tests are not meant to prove that the PBS is a better option than the MBS when considering a bezel size reduction. This statement is true for this particular antenna configuration. However, there are multiple other repositioning options for both the PBS and the MBS to avoid any of them being blocked by the screen's metal. This only goes to prove that the assessment of antenna performance is heavily dependent on the form factor used and, therefore, no antenna evaluation for mobile phone should be performed without considering the form factor. Moreover, from this analysis we can conclude that the most important smartphone material to consider when studying the form factor influence on the antenna's behavior is, in fact, the smartphone's metal chassis. The influence of the other form factor materials on the antenna's performance was minimal, suggesting that these are not relevant enough to be included in the study, since they would only increase the computation time without actually bringing significant results. Therefore, the rest of the study will be carried out with the original, full sized, form factor in Figure 2.1.

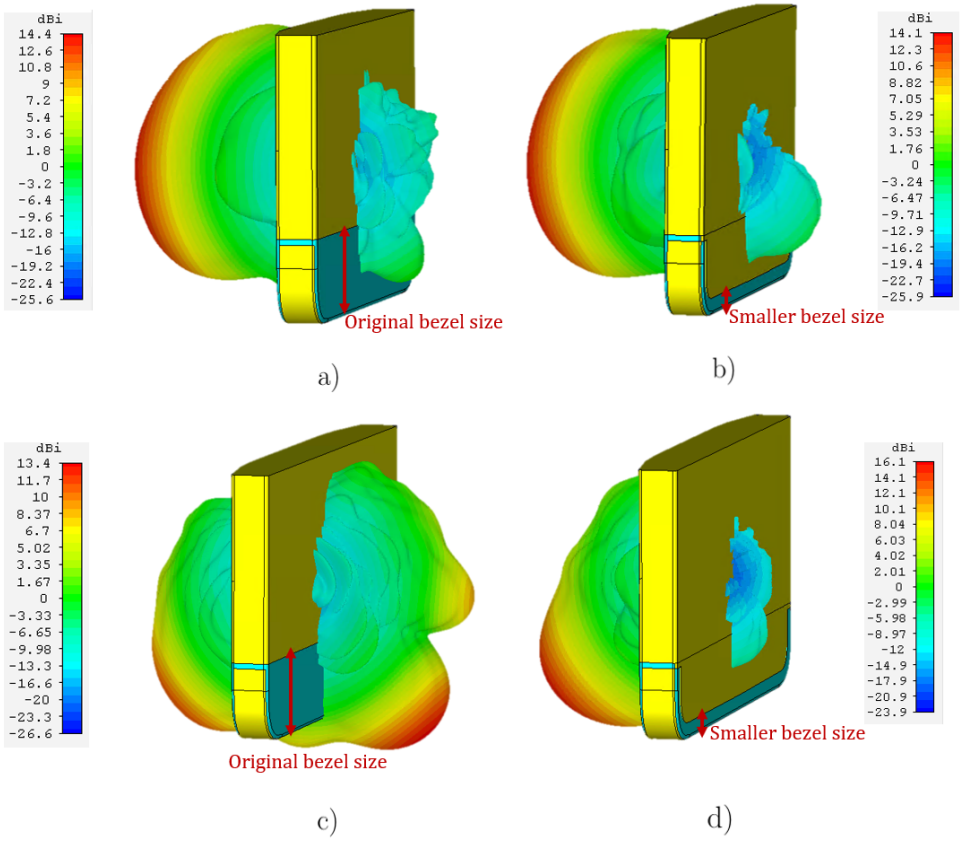

Figure 3.10: Array radiation pattern in a standard vs. smaller bezel size; a) PBS linear 4 element array implemented in a FF with a standard bezel size; b) PBS linear 4 element array implemented in a FF with a smaller bezel size; a) MBS linear 4 element array implemented in a FF with a standard bezel size; b) MBS linear 4 element array implemented in a FF with a smaller bezel size

3.1.3 User's hand influence

The introduction of the user's hand into the simulation provokes a drastic change in behavior of the radiation patterns. Figure 3.11 displays the radiation patterns for three different test cases.

In the first one, working as a reference, is the radiation pattern for the PBS and the MBS arrays implemented in the form factor, evaluated in free space. In the second test case the user's hand grip was added, specifically the TM grip, that resembles the stance of talking on the phone. Also for this test case, a second column was added with the beam $\psi = 70^o$, to assess the BF ability status. The third one also includes one of the user's hands, but in a BM grip, to mimic the stance adopted when browsing the Internet or playing a game on the smartphone. It is presented from two different perspectives, front and top, for better understanding.

By analyzing these radiation patterns it is clear that, despite of the hand grip used, all radiation pattern suffer the same effects when in close proximity with the hand. The once narrow and

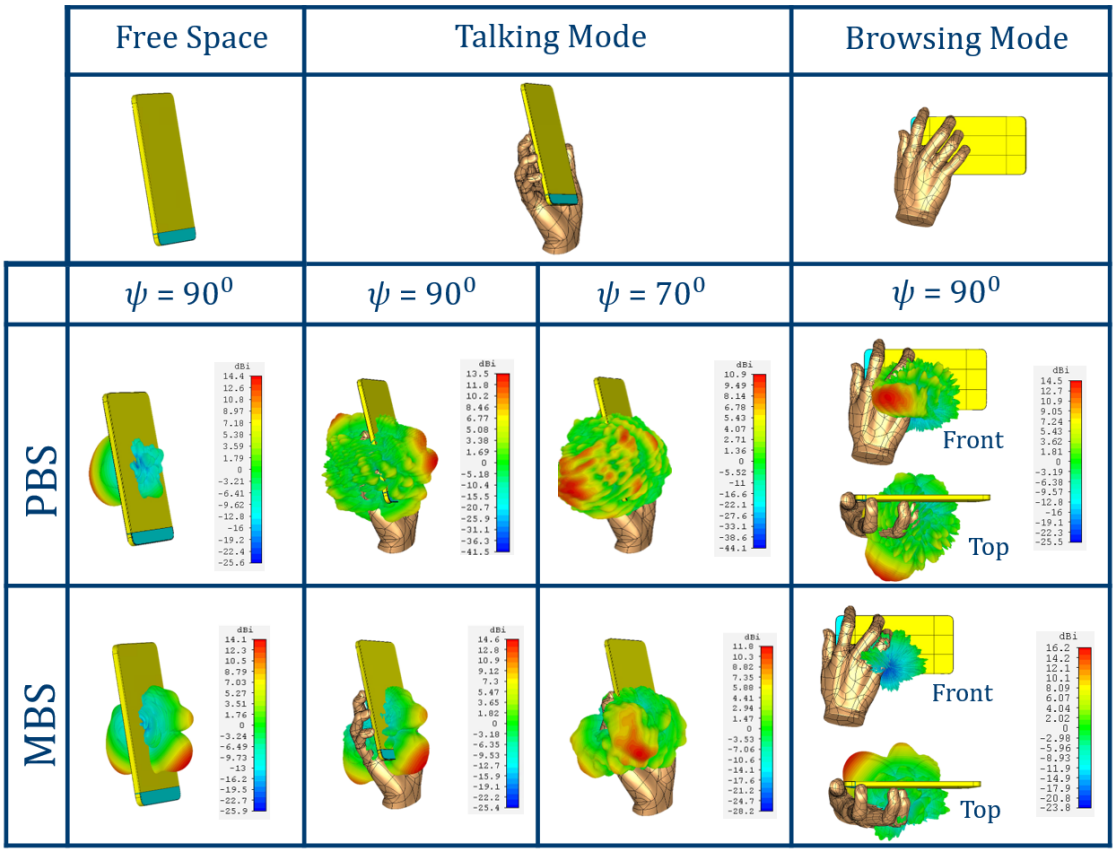

Figure 3.11: TM and BM hand grip effects on the arrays' radiation patterns implemented in the smartphone vs. the arrays' radiation patterns implemented in the smartphone for free space.

directive beams now take a random and unpredictable shape for their radiation pattern. For the TM Mode, considering the transition from the $\psi = 90^o$ beam to the $\psi = 70^o$ beam, it is noticeable that beam steering ability is also affected since all the beams lose shape when the user is involuntary covering the antennas, loosing its directivity.

This happens because of the human body's dielectric properties for the mm-Wave band. Besides UE-BS polarization mismatch caused by rotating the phone, the user influence on the antennas extends to three major aspects: impedance mismatch, energy absorption (in the near-field) and propagation body shadowing (in the farfield). However, for such high frequencies, the electric field does not penetrate the human body too deeply and the energy gets absorbed in the near-field very quickly, at the epidermis level.

The muscle was chosen as the main material to characterize the hand. At 39 GHz, it has an electrical conductivity of 42.5 Sm^{-1} [37] and its penetration depth is, approximately, 0.6 mm, which is not very significant. This can be seen from Figure 3.12 and Figure 3.13, which are a representation of the E-field propagation for, respectively, the PBS and the MBS over the phone and the user's hand for the TM grip. A transversal cut to the hand + form factor set reveal what was to be expected. The big dark blue area corresponding to the user's hand shows that, in fact, the electric

field is not able to propagate through the user himself. It ends up either reflected in the user's hand or escaping from gaps in between the user's fingers.

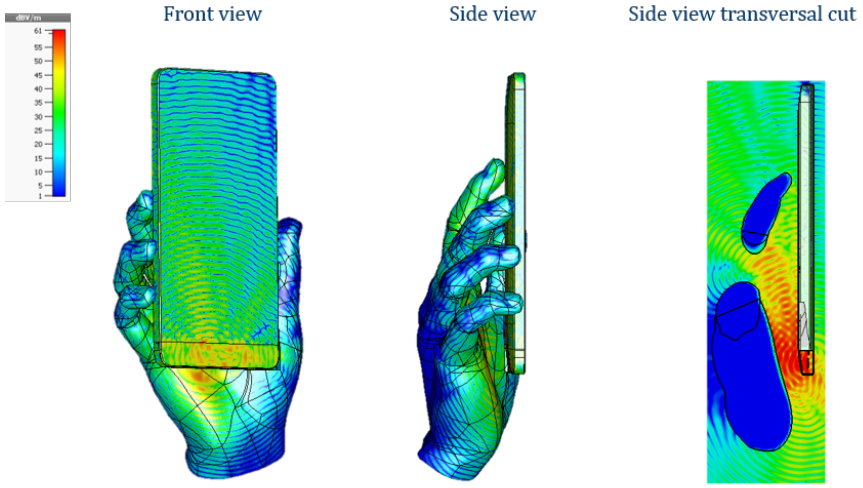

Figure 3.12: PBS array electric field propagation for the near field with a TM hand grip.

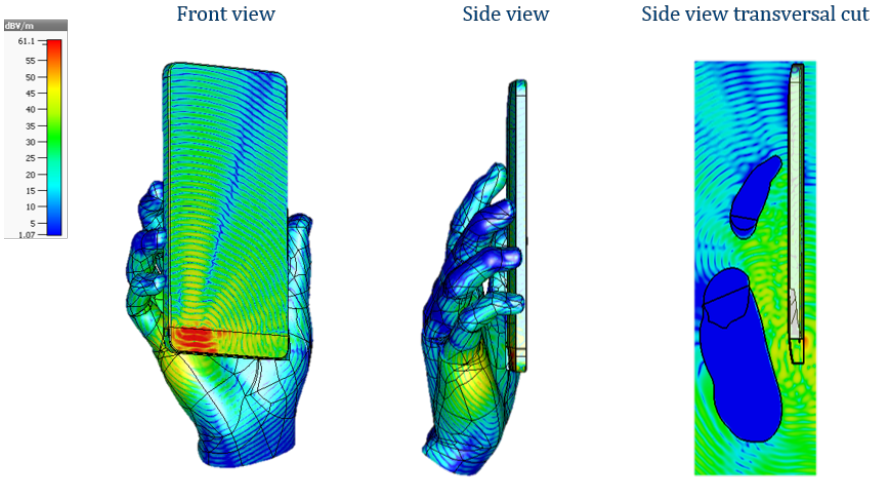

Figure 3.13: MBS array electric field propagation for the near field with a TM hand grip.

For this particular antenna positioning, the PBS is severely affected since it radiates through the back of the phone that is completely cupped by the user's grip. This is an unavoidable but recurrent challenge that mm-Wave propagation faces and it must be diverted through resourceful techniques such as the process of beam switching, for example. This is also a reason why the antenna dimensions should be small, to maximize the number of arrays within the phone, and consequently, minimize the user's body blockage. It is, therefore, very important to consider, besides the form factor, the user's body in the propagation studies of the antennas, to achieve the most realistic results.

3.1.4 Coverage study

As a validation of this CDF, the first CS is dedicated to a comparison between a single PBS antenna and a four element linear PBS array. Since the single antenna does not have BF ability, the PBS array was subjected to the comparison process using only the $\psi = 90^o$ beam. The phase shifter bit resolution was set at 5 bits and its range at 360^o. These values were chosen in order to increase the probability that the phases available in the phase shifter will match the one's necessary for the desired beam generation, minimizing the beam deviation obtained. In this case there are $2^5 = 32$ phase values from 0 to 360^o, to characterize the beam's phase shifts, which is enough to successfully create the $\psi = 90^o$ beam.

Figure 3.14 a) shows the CS curves, for the PBS antenna and the linear, four element PBS array. The two radiation patterns being compared are represented in Figure 3.14 b) and also in Figure 3.14 c).

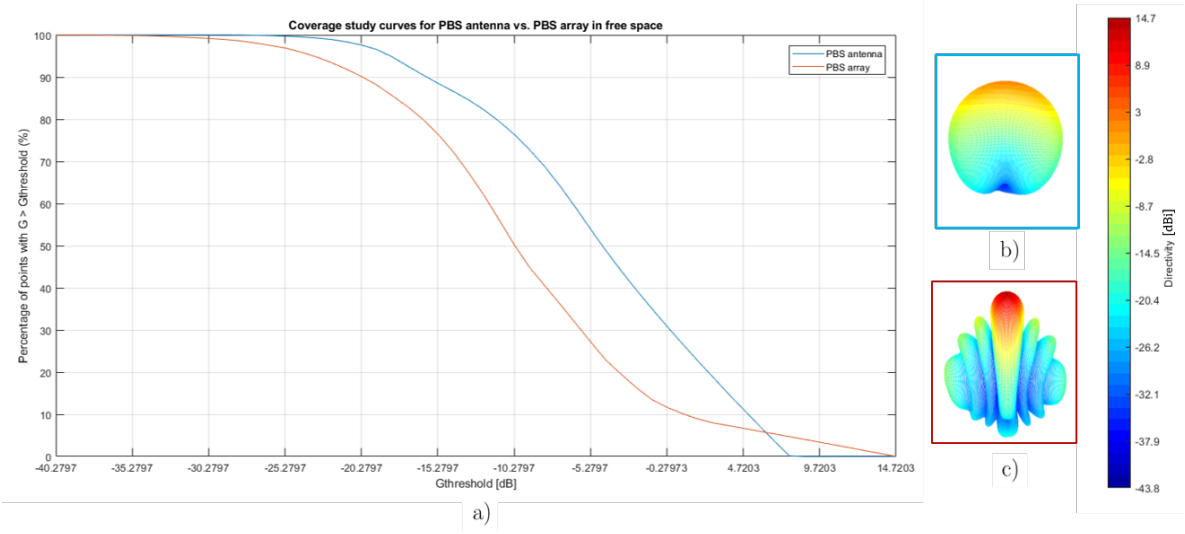

Figure 3.14: Coverage cuves for a single PBS antenna vs. a linear PBS array for various levels of gain threshold; a) Single PBS radiation Pattern; b) PBS array radiation pattern for $\psi = 90^0$.

At first, for a gain tolerance value lower than about 7 dB, the PBS array appears to present a higher coverage area percentage than the single PBS antenna, which makes sense. For these conditions, the single antenna cannot provide such coverage values, since it's maximum gain is 7.76 dB, 7 dB lower than the array's maximum gain value.The PBS array's gain is 14.7 dB, so as long as its gain is superior to the single PBS's gain, its coverage percentage will be higher.

The single PBS's radiation pattern is wider than the PBS array's, extending its reach to more directions than the array (despite having lower gain values). These results make it clear that, in these type of coverage studies, there is a certain balance between coverage and gain. There is usually a crossing point in the graphic, that is translated to comparing a wider radiation pattern to a narrower and possibly higher gain one.

This same method is used to compare the coverage provided by the PBS and the one from MBS, when implemented in a linear four element array in the smartphone. A 17 codebook entry, from

$\psi_d = 50^o$ to $\psi_d = 130^o$ was created for both the PBS and the MBS implemented in the smartphone to be evaluated for gain coverage in space. The phase shifter has, once again, 5 bit resolution and a 360^o range.

Figure 3.15 shows the PBS and MBS's respective codebook envelopes in the truncated coverage sphere, where two different threshold gains were indicated, $G_{threshold_1}$ and $G_{threshold_2}$.

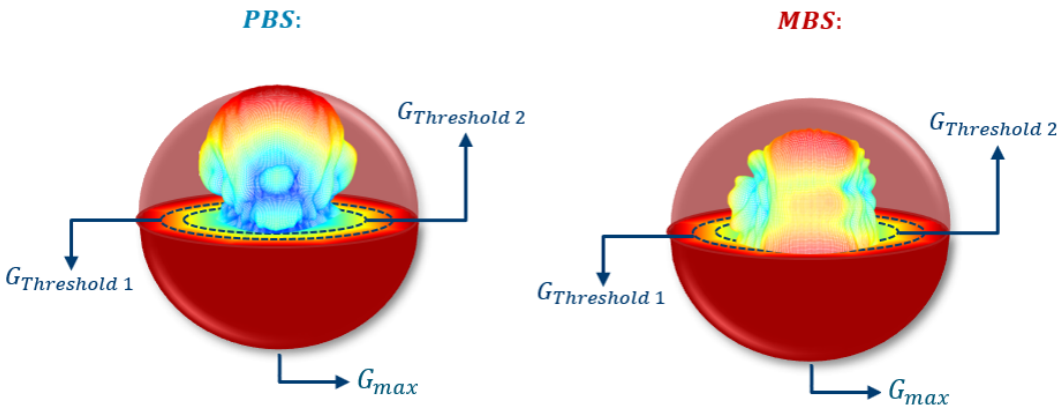

Figure 3.15: Patch vs. Monopole 17-codebook entry envelope within the coverage sphere.

For a CS comparison, the G_{max} of the sphere takes the form of the highest gain value out of the two codebooks. In this case, where the form factor is not truncated, $G_{max_{PBS}} = 14.33$ dB and $G_{max_{MBS}} = 14.08$ dB. Figure 3.16 shows the two coverage curves for the PBS and MBS throughout several values of $G_{threshold}$, including $G_{threshold_1}$ and $G_{threshold_2}$.

The curve starts at 100% because, naturally, all the gain values evaluated will be higher than G_{min}. The coverage percentage gets worse for higher values of the $G_{threshold}$, which are rarer. Therefore, for smaller values of threshold gain, at the sphere's core, the MBS array has the biggest coverage percentage. To cover 50% of the analyzed solid angle values, the PBS has to forfeit $G_{max} - G_{Threshold|50\%} = 14.84$ dB, while the MBS would have to forfeit, under the same principle, 11.96 dB. This is because, despite having similar maximum gain values, the MBS array has a wider codebook envelope shape, that extends in all directions. The PBS, on the other hand, radiates in a slightly more concentrated number of directions.

A more detailed analysis is done regarding the crossing point. When the crossing point is reached, at around $G_{threshold} = 6.33$ dB, there is a shift in the curves behavior. For $G_{threshold_1}$, which translates into a smaller gain value, the coverage performance is best performed with the MBS (coverage dominated area). But when going over the crossing point, the set of results from collected at $G_{threshold_2}$ show otherwise (gain dominated area). These examples reiterate the delicate balance between coverage and gain argument mentioned above. Nonetheless, the curves are relatively similar, and the difference between them ends up being just a few dB. This reinforces the idea that the MBS would do just as good as the PBS when implemented in a smartphone.

The same tests were performed but for different additions of components to the form factor, more specifically the glass screen, the plastic rear case and the change in bezel size. The 50% coverage values are gathered in Table 3.1.

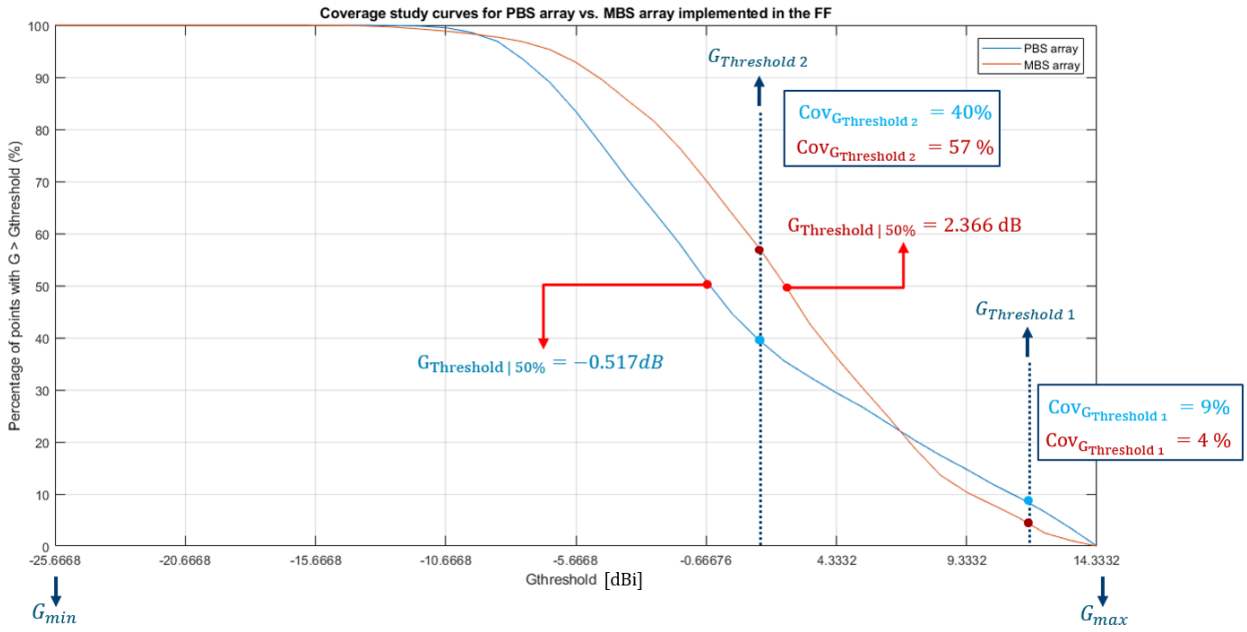

Figure 3.16: CDF curves for patch vs. Monopole in coverage area for various levels of gain thresholds.

Table 3.1: 50% coverage $G_{threshold}$ values for the original form factor, form factor with plastic back rear cover and screen added and form factor with an altered bezel size.

	FF [dBi]	FF + Cover + Screen [dBi]	new FF (bezel size) [dBi]
PBS	-0.52	3	-1.4
MBS	2.37	-0.93	-3.94

These coverage results confirm the conclusions drawn from the radiation pattern analysis previously made that translates into a coverage curve very similar to the one from the original form factor.

The last step of these tests is adding the user's body blockage effect. In order to do so, the same exact simulation parameters were taken from Figure 3.16 but the hand grip was also added to the simulations. The TM grip was chosen for its popularity and its influence on the curves is displayed in Figure 3.17.

A quick look into this plot reveals a crucial aspect of this investigation. When adding the user's hand, the coverage curves get closer to each other. This happens because, as seen above, the hand completely destroys the radiation patterns, rendering them to a random shape with a certain gain value. This further validates the hypothesis that there is really no difference in using PBS and MBS when all environment components are taken into account. The PBS might appear to have better qualities in free space. However, with the introduction of the form factor and the user's hand the PBS's performance turns out to be very similar to the MBS.

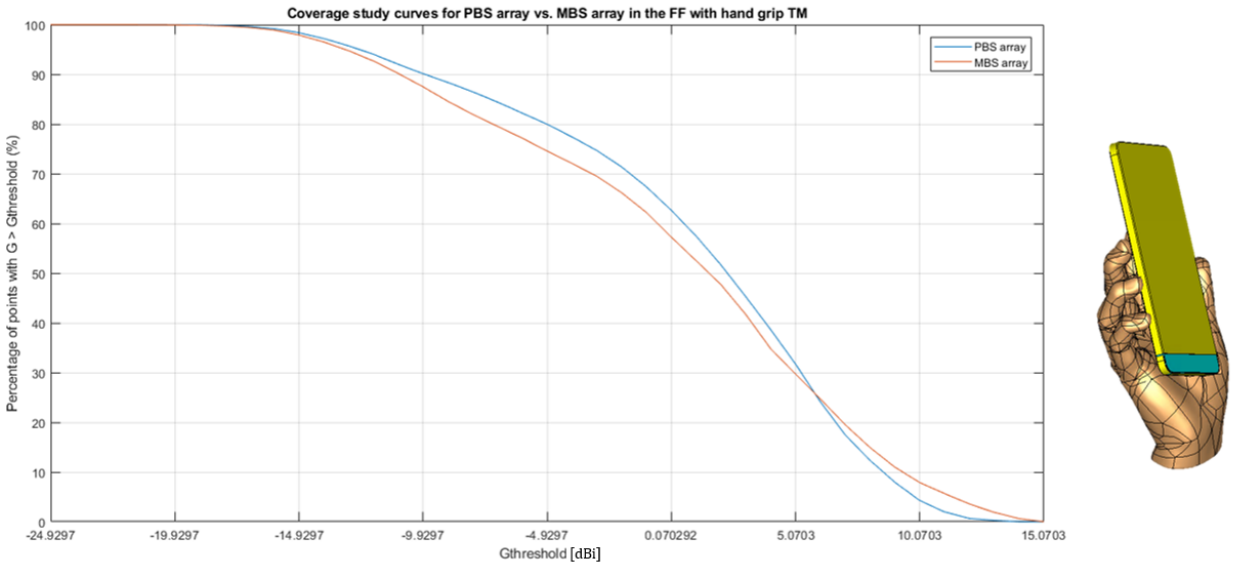

a) b)

Figure 3.17: Coverage study for user influence; a) Coverage percentage for the linear four element PBS and MBS arrays for a seventeen-entry codebook with smartphone implementation and hand grip; b) Hand grip in use, TM.

3.2 Summary

This chapter contains the results that characterize the behavior of the PBS and MBS antennas used for the dissertation in the context of smartphone implementation. The main considerations drawn from these simulations can be summarized in the following bullet points:

- For the free space scenario: the results showed that the PBS array displayed a higher gain value than the MBS array when performing BF.
- Smartphone Influence: the material that most affects the performance of the antennas is the phone's metal structure. The antennas' electromagnetic waves can not penetrate through metal, which results in the alteration of their radiation patterns. The closer it is to the antenna the more deformed the radiation pattern becomes. Also, once implemented into the form factor, the PBS and MBS gain values become very similar.
- User's hand influence: adding the human hand grip to the simulations changed drastically the antennas radiation pattern and efficiency. At 39 GHz the human body behaves like an obstacle, blocking any electromagnetic wave that is radiated in its proximity. Because of this, when the user holds the phone the array beams lose their shape and the ability to perform BF is compromised.
- CS: after implementing the antennas into the smartphone's form factor, two scenarios were considered - with and without user influence. If the user contribution is not included in the simulations, then the MBS shows a slightly better coverage curve than the PBS, despite them

being pretty similar. When the hand grip is included the two coverage curves get even closer (because the hand influence turns the once narrow radiation patterns into deformed shapes). This supports the argument that there is not much difference between using a complex patch array or a more simple monopole array, when realistic environment conditions are included in the tests performed.

Chapter 4

Antenna influence on MIMO channel performance

This chapter deals with the results regarding the PBS and the MBS's influence on the MIMO channel. It is divided into three sections:

- Simulator validation: Before interpreting the results it is necessary to verify if they match the theoretical expectations. This will be done for two different UE orientations, position 1 and position 3, in three different test scenarios, LOS, LOS + MP and NLOS, thus covering the full range of functionalities of this simulator. The parameters evaluated will be the beam pair selection, CN, SNR and C. Once the MIMO channel simulator is validated, it can be used to conduct the rest of the study.
- MBS transmission technique: its important to establish what is the best transmission technique for the MBS. It can either be solely confined to SISO or it may be able to perform well as MIMO if the environment characteristics are right. The same test conditions used in the validation section, will be used here in the simulator to evaluate the CN, which is the metric that defines whether or not to use MIMO, and also C, since data rate is the end goal of any link communication.
- Finally, the second stage of the mm-Wave comparison process will take place. It consists of evaluating how susceptible both antenna families are to the phone's rotation in space. This is achieved through a thorough analysis considering the same three test scenarios mentioned before, using the MIMO channel simulator. The results obtained contain the answer to which of the antennas can assure a stable and high enough data rate in all directions in space for the mobile phone in a typical dynamic environment.

Similarly to the CS, this study requires that both antenna families are analyzed under the same conditions in hopes of establishing a fair and reliable comparison than can be used in other projects, under a different context, to weigh in on the decision of which type of antenna should be implemented for a 5G smartphone.

4.1 Simulator validation

As mentioned before, there are three main test scenarios that can be set up, simply by changing the scatterer reflection coefficient amplitudes. These three scenarios are LOS, LOS with MP component and NLOS with MP component, all represented in Figure 4.1 and described in detail below.

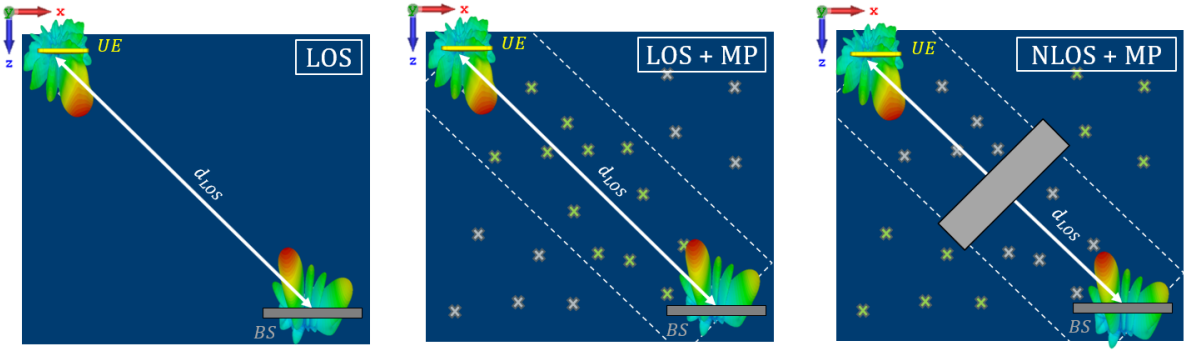

Figure 4.1: Representation of the three test scenarios for validation in the xy plane.

- LOS: It is the reference scenario where there is solely the unobstructed direct path without any source of MP. It can be accomplished by setting the reflection coefficient to zero for all scatterers, killing any MP components in the H matrix calculations.
- LOS with MP: The scatterers within the scatterer rectangular limit will increase the MP needed to create a MP rich MIMO channel. This is the most common scenario for an urban area, so it must be thoroughly studied. It is obtained by placing $S = 15$ scatterers within a 140×12 meter rectangle evolving the UE and the BS. The scatterers reflection coefficient follows a Gaussian distribution with a null median value and a standard deviation of 0.55. The scatterer's movement over the x axis is uniform with a total range of motion of two meter (one meter to $-x$ or one meter to $+x$).
- NLOS: For this scenario, the LOS component is expected to be almost null, due to the obstruction of the LOS path between the UE and the BS by an obstacle. However, adding MP to the environment would give the signal alternative paths to the one that is blocked and communications would be possible again. Therefore, in the third scenario, NLOS + MP, the channel must rely on further placed scatterers, beyond the main rectangle, to perform communications. Therefore, the LOS component is suppressed in the calculations and the scatterers will lead to higher values of d_{NLOS}. They are distributed within 6 to 12 meters away from the center of the original scatterer rectangle. In order to obtain this reference value for the scatterer location, several scatterer distributions were tested using the simulator in order to find the limit area where their influence would become almost insignificant. The 6 to 12 meters resulted as a compromise between all the simulations performed.

These three test scenarios will be launched for both the PBS and the MBS in two different phone positions: position 1, where the UE's back is facing the BS's arrays and position 3 where the UE is rotated by 90^o in the xy plane, both represented in Figure 4.2. For this particular set of tests, the UE and the BS are aligned with each other at $x = 0$, and have a distance between them of

120 meters. The BS is at 10 m height and the UE is at a reference height of 0 meters. These values were based of several simulations performed with the simulator to recreate the most realistic environment conditions according to reference values found in the literature.

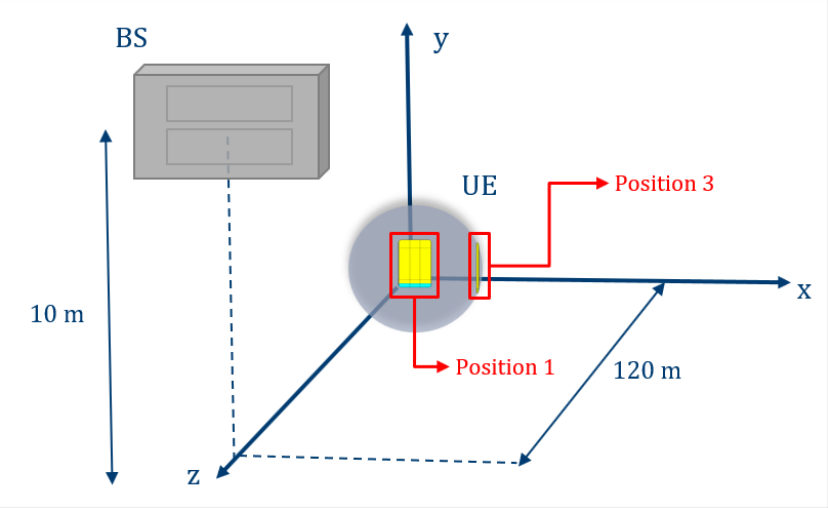

Figure 4.2: Test scenarios used for validation of the MIMO channel simulator.

Figure 4.3 represents the scatterer distribution used in the validation process, for all test scenarios with MP. The scatterers are represented by the blue circles. The blue arrows over the scatterers indicate their range of motion over T time slots. For this project the scatterers could move along the x axis either one meter to $+x$ or one meter to $-x$, so the full range of motion is two meters. Some of the scatterers were placed behind the UE to ensure the existence of scattering paths when the UE's arrays are completely turned away form the BS.

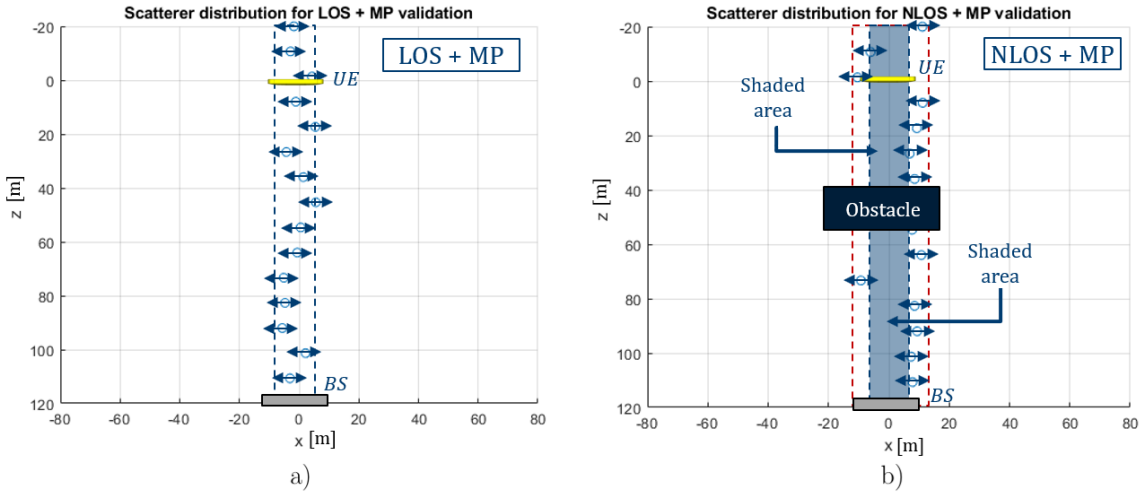

Figure 4.3: Scatterers distribution for LOS + MP and NLOS + MP validation test scenarios.

Also, some parameters of the receiver and transmitter are also defined for link budget and SNR calculations. Therefore, the power transmitted by the UE is considered to be $P_t = 0.1$W and the BS's receiver has a $NF = 6$ dB and a channel bandwidth $BW = 100$ MHz. For LOS there are no moving scatterers and, therefore, the values of capacity, SNR and CN are constant throughout the $T = 1000$ time slots. This is not the case with LOS + MP and the NLOS + MP, where the MP component changes over time due to a highly dynamic environment caused by moving scatterers. This means that, instead of one single constant value, like in the LOS, there will be, per time slot, a value to describe the capacity, SNR and CN. As an example, Figure 4.4 a) shows the scatterer placement and its motion over time for the UE in position 1. Figure 4.4 b), Figure 4.4 c) and Figure 4.4 d) show, respectively, the corresponding CDF's of the CN, SNR and C for the PBS in the LOS + MP scenario. In this stage of evaluation it is important to include in the analysis all the channel metrics and not just C, since both the CN and the SNR affect significantly C. Without these two, it is not possible to know the cause of a a high or low distribution of C.

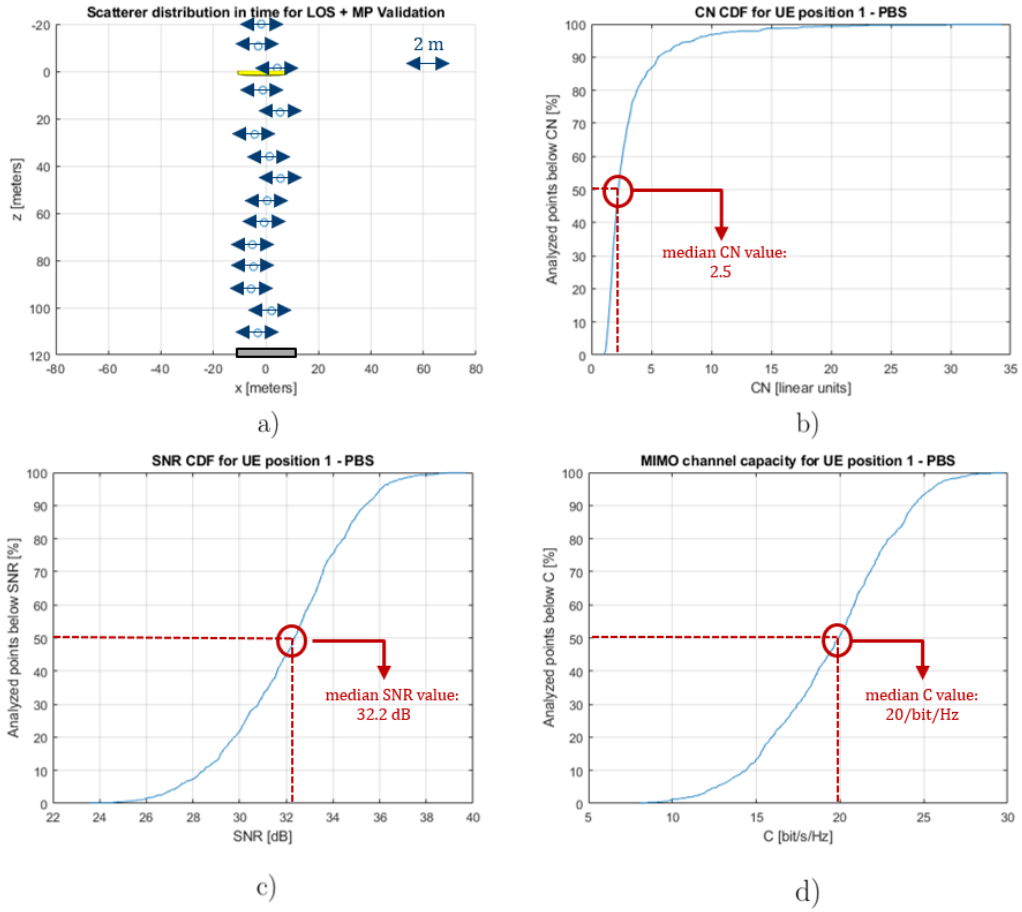

Figure 4.4: Scatterer distribution for UE's position 1 (using PBS) and its corresponding capacity CDF.

One of these curve points must be chosen to represent this particular scenario's capacity as a measure of comparison with other scenarios. A good enough indicator would be the CDF's median

Table 4.1: LOS, LOS+MP and NLOS+MP channel metrics for positions 1 and 3 - PBS MIMO

PBS (MIMO)	SC1		SC2		SC3	
	pos 1	pos 3	pos 1	pos 3	pos 1	pos 3
beam choice (UE-BS)	$90^o - 90^o$	$130^o - 90^o$	$90^o - 90^o$	$130^o - 90^o$	$90^o - 110^o$	$130^o - 90^o$
CN	1.11	12.64	2.25	3.85	2.7	3.31
SNR [dB]	28.17	11.93	32.34	17.67	25.3	17.68
Capacity [bit/s/Hz]	18.71	5.26	19.92	9.07	14.58	9.17

value. By definition, using the median ensures that half of the samples analyzed from that scenario will have a capacity higher than that value. In conclusion, all channel metrics (beam choice, CN , SNR and beam choice) in LOS + MP and NLOS + MP scenarios will be represented by their CDF's median values.

The tests described above, named as SC1 (LOS), SC2 (LOS + MP) and SC3 (NLOS + MP), are conducted for both the PBS and the MBS to test the validity of the results.

4.1.1 PBS

Starting from the beam selection process in the UE, for all three scenarios, it seems to match expectations. Figure 4.5 a) shows the notation for each UE and BS beam in space for position 1 and Figure 4.5 b) presents the same for position 3, so that the beam criteria analysis is clear.

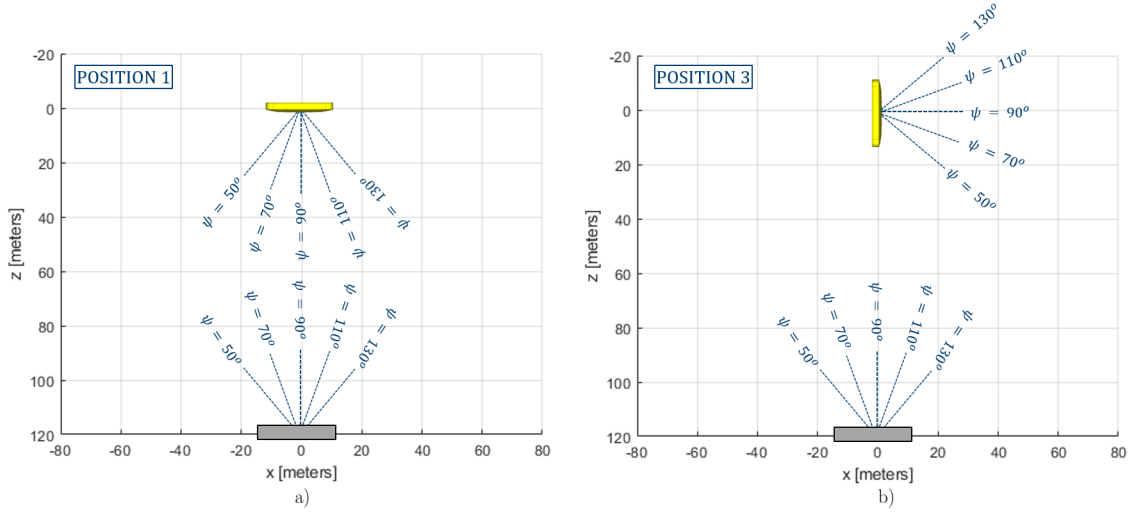

Figure 4.5: Beam notation for UE and BS for ψ_{UE} beams ψ_{BS} beams; a) UE Position 1; b) Position 3.

Therefore, for position 1, in LOS scenario, the central beams are selected because the UE and the BS arrays are aligned in space. Therefore in position 1, the UE chooses $\psi = 90^o$ and the BS also chooses $\psi = 90^o$. For position 3, the UE is rotated and the $\psi = 90^o$ beams previously chosen are now in orthogonal directions, which means a new beam pair will be chosen. The beam for the BS shouldn't change, because the UE did not move, just rotated. Therefore, it is the UE's beam

choice that will vary with its rotation. Table 4.1 reveals that, in fact, the UE changed its beam choice from $\psi = 90^o$ to $\psi = 130^o$ while the BS's choice remained the same.

At first, one could presume that the beam picked for the UE would be $\psi_d = 50^o$ since it is the beam closer to the BS when the UE is in position 3, producing the strongest link. However the results show otherwise. As explained previously, for the PBS, the beam pair link is selected from a group of entries within the power matrix that abide the condition $P_{max} - 3dB < P_{ij} < P_{max}$. The entry with the lowest CN value will be selected to perform communications. For this particular case, the two highest power values belong to the matrix entry $\psi_{dUE} = 50^o$ - $\psi_{dBS} = 90^o$ and the entry $\psi_{dUE} = 130^o$ - $\psi_{dBS} = 90^o$) but the latter is indubitably the winner in terms of power of connection, as can be seen from Figure 4.6.

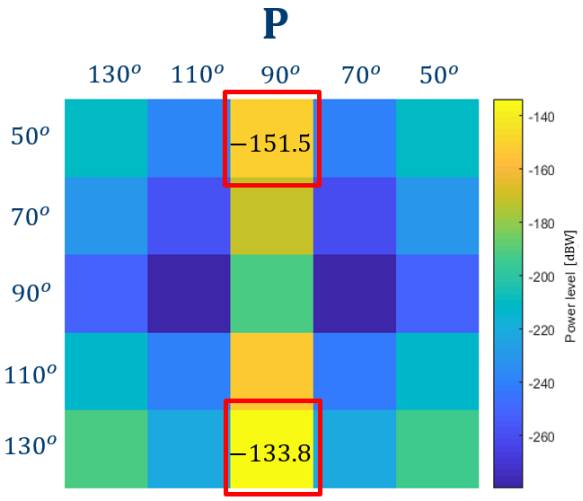

Figure 4.6: Power matrix P for UE's position 3 using PBS array.

There is not even the need to continue the process of calculating the CN, since only one of the entries meets the power condition required, making the choice a final decision. This situation can be explained by the fact that the beam $\psi_d = 130^o$ has a significantly large secondary lobe in the opposite direction of the main lobe, as can be seen from Figure 4.7.

This side lobe will rival the main lobe from the $\psi_d = 50^o$ beam in terms of gain in the direction of observation. Figure 4.8 shows the gain distribution in space using PBS for both $\psi_d = 50^o$ and $\psi_d = 130^o$. A quick check for the gain values of the direction in which the UE sees the BS, $(\theta^{UE}, \varphi^{UE})$=$(4^o, 90^o)$, confirms that the secundary lobe from $\psi_d = 130^o$ has a higher gain value than $\psi_d = 50^o$ $(G_{\psi_{dUE}=50^o} = -5.95dBi < G_{\psi_{dUE}=130^o} = -1.70dB)$, generating a higher power link.

It is difficult to assess if the beam selection process is correct in a scenario with MP because there are too many reflections caused by the scatterers, not to mention the scatterers move in each time slot so it is very challenging to track down the exact scatterer that led to the beam pair presented in Table 4.1. However, a second exaggerated scenario can be created, in a NLOS scenario, to confirm that the simulator is capable of tracking the best beam pair selection in the presence of scatterers. Therefore, for positions 1 and 3 of the UE, all scatterers were placed on the right side

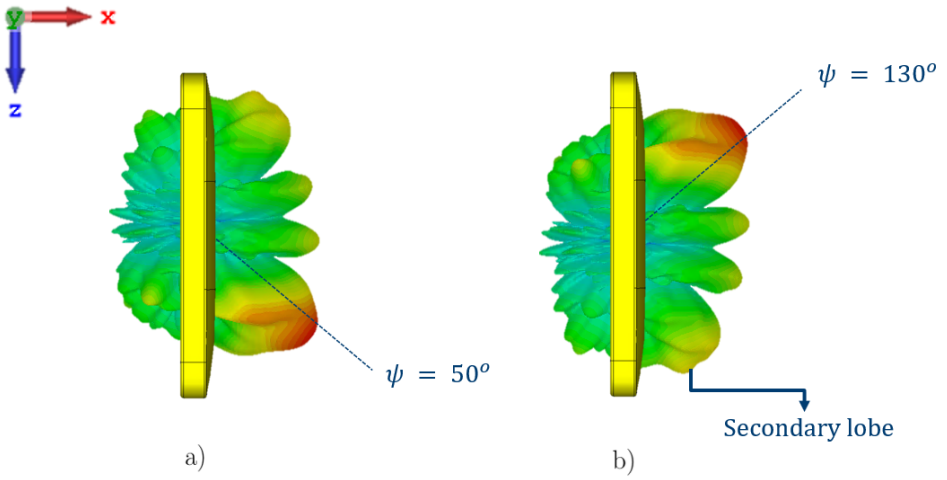

Figure 4.7: ψ_{50} beam vs ψ_{130} beam; a) ψ_{50} beam; b) ψ_{50} beam.

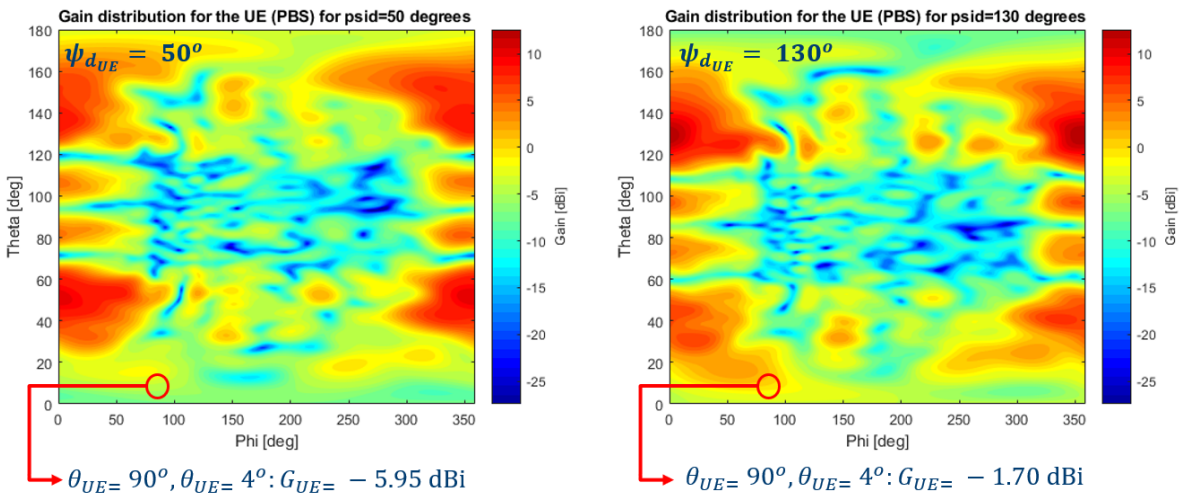

Figure 4.8: Gain distribution of the UE (PBS) for $\psi_d = 50^o$ and $\psi_d = 130^o$.

of the rectangular limit, far away, so that the scatterers would be placed between 10 meter to 17 meter away from the center of the rectangle, as seen in Figure 4.9. This extreme situation further validates the simulator since both the UE and the BS chose the same beam, for position 1, leading to the beam pair $\psi_{dUE} = 110^o$ - $\psi_{dBS} = 110^o$. This is an ideal choice for this situation, where the LOS path is interrupted. The ψ beam pair would only direct the signal against an impenetrable obstacle, therefore, the only option would be the beam right next to it in space, $\psi_d = 110^o$, that is deviated from the origin just enough to allow the signal to go around the obstacle. Naturally, if

a bigger number of beams was available, the step between them would be lower than 20^o and the beam choice process would be much more sensitive to the position of the close-by scatterers.

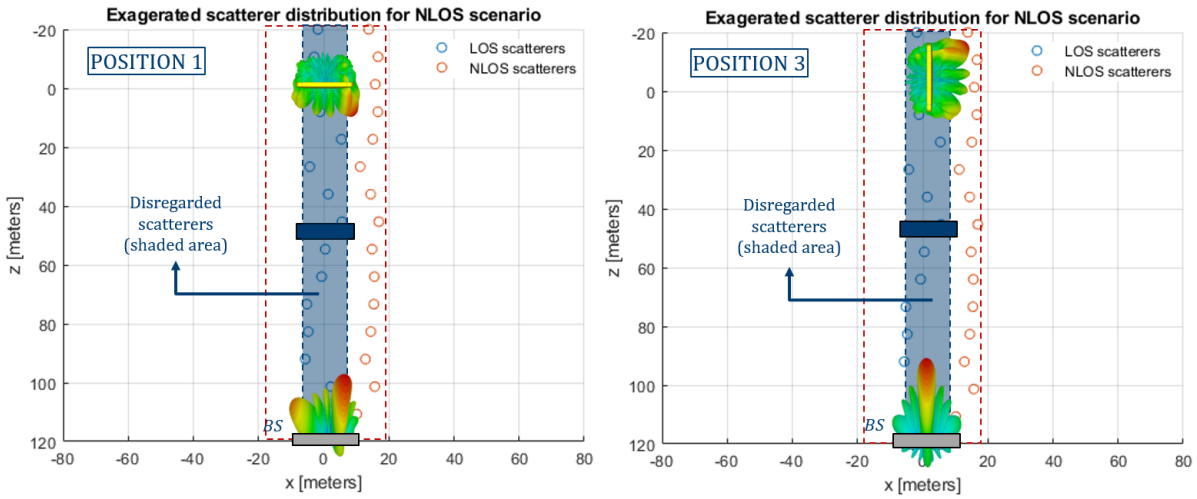

Figure 4.9: Beam pair choice for exagerated NLOS scatterer distribution for PBS; a) UE in position 1; b) UE in position 3.

For the PBS in LOS, in Table 4.1, the capacity plummets from 18.71 bit/s/Hz to 5 bit/s/Hz. This is to be expected since position 1 is the best possible UE orientation for the PBS. In position 1 the UE and the BS arrays are almost completely aligned, and the polarizations match perfectly, whereas position 3 disturbs that balance by introducing a 45^o misalignment in the xy plane. This causes a significant power loss that manifests into a lower SNR value, 11.93 dB, when compared to position 1's value, 28.17 dB. This is also corroborated by the CN value that, from position 1 to position 3, increases 12 times as a result of misaligning the once perfect array polarization between the UE and the BS.

Regarding the PBS, when adding the MP contribution, LOS + MP, the capacity and SNR values increase, for both positions, which corresponds to the expectations. As mentioned before, MP is very beneficial to MIMO transmission schemes. A reflection rich environment will provide the signal with multiple uncorrelated paths to propagate through, which ultimately will result in more signals being transmitted simultaneously in the same bandwidth without risking high correlation values and increasing the channel's capacity. MP also increases the signal's power gain from the scattering signal's contributions. For this scenario, the CN value for position 1 increased and for the position 3 it decreased. Both these results can be explained by the depolarization caused by the MP. When the signal hits an obstacle, it gets scattered while losing its original polarization. This is advantageous for position 3, since this effect brings the transmission signal's polarization closer the BS's. However for position 1 this is an inconvenience, since the polarization alignment was perfect to begin with, and MP will only disturb it.

The next set of results to be analysed is NLOS + MP. Despite not having a clear and direct view from the UE to the BS the capacity and SNR values are still far from being zero. This wouldn't be possible without such a rich MP environment. However, the clear tendency is for the capacity and

Table 4.2: LOS, LOS+MP and NLOS+MP channel metrics for positions 1 and 3 - MBS SISO

MBS (SISO)	SC1		SC2		SC3	
	pos 1	pos 3	pos 1	pos 3	pos 1	pos 3
beam choice (UE-BS)	$90^o - 90^o$	$130^o - 90^o$	$90^o - 90^o$	$130^o - 90^o$	$110^o - 90^o$	$130^o - 90^o$
SNR [dB]	18.31	18.72	21.78	22.11	14.3	17.05
Capacity [bit/s/Hz]	6.10	6.24	6.75	6.83	4.16	5.13

SNR values to be lower than the LOS + MP, which is understandable. Because there is no LOS component and the scatterers are further away (from the direct path and the obstacle), so it is only natural for the signal to arrive with less stregth, having a smaller SNR value and, therefore, lower capacity value. However it is worth mentioning that the CN values are better than the LOS + MP ones, but the signal strength is too weak to achieve higher capacity values, because the distance increases.

4.1.2 MBS

Regarding the MBS, since the right transmission technique hasn't been defined yet, for the sake of validation, SISO is going to be assumed. Therefore, the channel metrics evaluated are the beam pair, SNR and C, as can be seen from Table 4.2.

The analysis of the MBS SISO results, displayed in Table 4.2, is very similar to the one performed for Table 4.1. The capacity and SNR values increase from LOS to LOS+ MP but drop from LOS to NLOS + MP. Despite the overall tendency for the channel metric results to follow the PBS's behavior, there are some aspects that are worth pointing out.

First of all, contrary to the PBS, there is not much of a difference between capacity and SNR values within the three test scenarios. Also, for the MBS, position 3 seems to be more advantageous that position 1 since the highest capacity and SNR are accomplished for position 3. Finally, the MBS's NLOS + MP scenario, because it is supported by far away scatterers, does not have enough signal strength (the NLOS + MP SNR value is between 14.30 dB to 17.05 dB, while the LOS + MP SNR is between 21.78 dB and 22.11 dB) to surpass the LOS + MP capacity values. Applying the same type of interpretation, the beam choice process also appears to be working perfectly for the MBS.

However, it cannot be helped but noticed that the capacity values achieved with the MBS are much lower than the ones obtained with the PBS. This was also to be expected, since this is a comparison between a MIMO and a SISO system with BF. Therefore, more tests must be made to inquire whether or not the MBS can support MIMO and achieve C results comparable with the PBS.

4.2 MBS transmission technique

The choice of using SISO with the MBS was purely intuitive, since both MBS arrays were placed in the smartphones in the same polarization in a tight enclosed space. However, the assumption that the MBS will not be suited for MIMO must be either verified or disproved, and that is done by evaluating the CN values. If CN is higher than 10, in linear units, this means that MIMO can't

Table 4.3: LOS channel metrics for MBS SISO vs MIMO

LOS Position	CN	Capacity	
		SISO	MIMO
1	13.4	6.10	7.02
2	2.93	6.38	10.02
3	4.21	6.24	7.20
4	3.68	5.97	8.35
5	36.7	7.34	7.94
6	8.52	6.93	8.56
7	4.43	6.66	7.02
8	7.62	6.77	8.97
9	344.7	9.27	9.45
10	226.1	8.01	7.96
11	61.51	9.94	10.31
12	6.54	5.07	6.73
13	19.82	3.62	3.49
14	6.28	3.42	3.53
15	4.93	5.99	7.62
16	3.69	5.61	6.95
17	2.34	7.41	11.96
18	2.27	6.98	11.37

be properly performed and the MBS would then change its transmission scheme from MIMO to SISO.

Table 4.3 list the CN values, as well as the SISO capacity and MIMO capacity for all 18 UE positions in LOS.

As expected, for CN values below 10, MIMO increases the channel capacity when compared to SISO. Surprisingly, for very high CN values, such as in positions 5,9, 10 or 11, the MIMO capacity values don't stray too far from the SISO capacity. This shows that there is no advantage in implementing SISO in the phone as a transmission technique. Overall, MIMO will always provide a better channel capacity and, in the worst case scenario, it will deteriorate to SISO capacity values, but never below. Therefore, from now one, the transmission technique considered for the MBS will the the same as the PBS, 2×2 MIMO.

Also, some consideration on the array coupling calculations for this thesis can be found in Annex A.

4.3 Channel performance's sensitivity to Phone Rotation

In this section, the study performed for the validation of the simulator will be extended to the 18 UE positions defined and represented in Figure 4.10. The channel metrics for all 18 positions will be evaluated for a numerous test scenarios such as LOS, LOS + MP and NLOS + MP, presented

previously, with addition of the user's hand influence in TM, which will provide the simulations with the maximum achievable level of realism for the test scenarios.

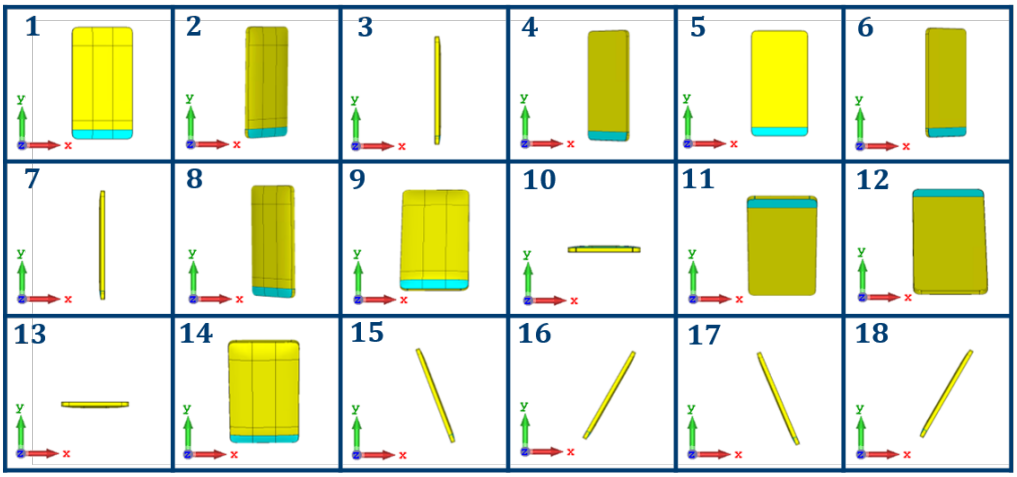

Figure 4.10: Identification of the 18 UE possible orientations in space.

The first antenna type to be analyzed is the PBS family. Table 4.4 summarizes the channel metrics parameters for all 18 UE positions that contain the PBS array implemented. These results are separated in three different columns, for each environment scenario, SC1, SC2 and SC3.

In LOS, the maximum capacity value obtained with the PBS is 18.71 bit/s/Hz for position 1, which, as discussed before is the most favorable position for the PBS family. Its lowest value of capacity, 2.21 bit/s/Hz, occurs for position 13, where the PBS array in the UE is facing the floor. Although the capacity values are high there is a steep drop between consecutive UE positions such as from position 2 (15.85 bit/s/Hz) to position 3 (5.26 bit/s/Hz). While some low capacity values are justified by high CN values, like positions 3 and 13, others are simply caused by low power values (that are reflected in the smaller SNR values), such as positions 4, 5, 6, 7, 10, 11, 12. The latter source of low data rate could be fixed by, besides shortening the UE-BS distance, boosting the power in the UE, which would incur in serious battery drainage on the UE side. Although, for the PBS, there are certain symmetrical positions from the BS point of view (pairs position 3 - position 7, position 15 - position 18 and position 16 - position 17) that would be expected to have similar channel metrics. In fact, the capacity and SNR are very similar for all these pairs but the CN values on the right side of the sphere (positions 3, 15, and 16) are much higher that the ones on the left side of the sphere (positions 7, 17 and 18). This is probably due to polarization mismatch effects. The PBS is placed in the center of the UE and, at first sight, it appears to be perceived by the BS in the same way for all these pairs of positions. However, the truth is that the PBS feeding is not symmetrical when the phone is rotated from position 3 to position 7, for example. This will cause for the feeding pins to radiate in opposite directions, for position 3 the feeding pins radiate away from the BS and in position 7 they will radiate towards the BS, justifying the discrepancy in the CN values. The beam choice values remain concordant with what was seen during the simulator validation.

The introduction of MP will smooth out these abrupt channel metric changes between UE po-

Table 4.4: LOS (SC1), LOS + MP (SC2) and NLOS + MP (SC3) channel metrics for PBS MIMO

	Capacity [bit/s/Hz]			SNR [dB]			CN			beam choice (UE-BS)		
Position	SC1	SC2	SC3	SC1	SC2	SC3	SC1	SC2	SC3	SC1	SC2	SC3
1	18.71	19.92	14.58	28.17	32.35	24.86	1.11	2.25	2.69	$90^o - 90^o$	$90^o - 90^o$	$90^o - 110^o$
2	15.85	17.14	14.19	24.24	27.83	22.55	1.55	2.43	2.79	$50^o - 90^o$	$50^o - 90^o$	$70^o - 90^o$
3	5.26	9.07	9.18	11.93	14.59	15.61	12.64	3.94	3.32	$130^o - 90^o$	$130^o - 90^o$	$130^o - 90^o$
4	4.59	9.74	8.16	7.11	16.20	9.75	2.48	3.06	3.14	$70^o - 90^o$	$130^o - 90^o$	$110^o - 90^o$
5	2.74	11.03	7.90	3.25	15.87	9.31	3.15	3.00	3.09	$70^o - 90^o$	$110^o - 90^o$	$70^o - 90^o$
6	4.87	10.42	8.90	8.39	16.94	9.43	3.34	2.79	3.00	$130^o - 90^o$	$50^o - 90^o$	$70^o - 90^o$
7	6.40	9.19	7.30	11.76	14.75	10.25	3.83	3.61	3.61	$50^o - 90^o$	$50^o - 90^o$	$50^o - 90^o$
8	16.22	17.39	11.63	24.53	28.54	19.20	1.28	2.47	3.07	$130^o - 90^o$	$130^o - 90^o$	$130^o - 90^o$
9	15.01	16.22	10.34	22.63	25.94	17.35	1.17	2.34	2.87	$50^o - 90^o$	$90^o - 90^o$	$110^o - 90^o$
10	7.93	9.02	4.56	13.14	14.68	4.53	2.50	3.13	3.97	$90^o - 90^o$	$90^o - 90^o$	$110^o - 90^o$
11	7.04	9.66	6.88	11.20	15.68	8.37	2.11	2.86	2.88	$90^o - 90^o$	$90^o - 90^o$	$70^o - 90^o$
12	2.49	6.66	5.54	2.53	8.90	5.47	3.22	3.20	3.39	$70^o - 90^o$	$70^o - 90^o$	$110^o - 90^o$
13	2.21	4.48	4.04	2.50	4.38	0.50	12.97	4.91	4.40	$50^o - 90^o$	$50^o - 90^o$	$130^o - 90^o$
14	13.12	14.76	9.56	20.06	23.10	14.53	1.52	2.40	3.06	$90^o - 90^o$	$90^o - 90^o$	$110^o - 90^o$
15	5.62	9.70	7.92	12.10	15.90	11.89	8.05	3.65	3.94	$130^o - 90^o$	$130^o - 90^o$	$130^o - 90^o$
16	5.58	9.26	8.50	12.01	15.22	14.11	8.09	3.90	3.59	$130^o - 90^o$	$130^o - 90^o$	$130^o - 90^o$
17	5.98	8.76	6.02	11.48	14.30	4.90	4.59	3.59	3.84	$50^o - 90^o$	$50^o - 90^o$	$50^o - 90^o$
18	7.06	10.28	9.83	3.10	17.70	9.83	3.10	3.16	3.32	$150^o - 90^o$	$50^o - 90^o$	$130^o - 90^o$

sitions. As can be seen from Table 4.4, the channel capacity values increased, when compared to SC1, for both SC2 (LOS + MP) and SC3 (NLOS + MP), despite SC3 relying on further away scatterers. Also, some changes to the CN values can be observed with the contributions of MP. As discussed previously in the validation section, there is an improvement in the CN values for the UE positions where the CN was too high, such as position 3 and position 13, bringing it well below the MIMO communication threshold of $CN = 10$. On the contrary, for the UE positions where the CN values were close to ideal, the MP contributes negatively, increasing the CN. This can be seen for UE positions 1, 2, 8 and 9, for example. However this increase in CN value is not so significant as to prevent MIMO communications, since these values are all below 5 and, therefore, can be disregarded. The beam pair selections also appear to be congruent with the introduction of MP.

Considering the results from Section 4.2, a MIMO study was performed for the MBS antenna and summarized in Table 4.5.

The analysis of this table is similar to the PBS's. The introduction of MP reduces the CN to acceptable values thus increasing the channel capacity. Overall, both the capacity and the SNR values for the MBS are a lot less sensitive to rotation, compared to the previously displayed PBS results. This is an advantage towards the MBS, since a more stable data rate would be guaranteed despite the interference of the user that involuntarily rotates the phone around.

Finally, there is one more layer of user influence that needs to be taken into consideration in the simulations. Besides rotating the UE around, the user also holds the phone, potentially covering the antennas with his hand. It is important to assess how big the impact of adding a hand to the form factor is for the simulations. Therefore, the hand model TM was chosen to be added to the 18 UE phone orientations, as represented in Figure 4.11. As mentioned earlier TM was chosen because it is one of the most common hand position when using a mobile phone. Adding the user's

Table 4.5: LOS (SC1), LOS + MP (SC2) and NLOS + MP (SC3) channel metrics for MBS MIMO

	Capacity [bit/s/Hz]			SNR [dB]			CN			beam choice (UE-BS)		
Position	SC1	SC2	SC3	SC1	SC2	SC3	SC1	SC2	SC3	SC1	SC2	SC3
1	7.02	11.56	8.08	16.38	20.07	13.45	13.4	3.92	3.38	$90^o - 90^o$	$90^o - 90^o$	$110^o - 90^o$
2	10.02	11.80	8.86	17.00	19.56	14.52	2.93	3.83	3.26	$50^o - 90^o$	$50^o - 90^o$	$50^o - 90^o$
3	7.20	10.53	8.68	13.48	18.15	12.51	4.21	3.61	3.33	$50^o - 90^o$	$50^o - 90^o$	$50^o - 90^o$
4	8.35	11.60	9.75	15.05	19.74	16.00	3.68	3.10	3.34	$50^o - 90^o$	$50^o - 90^o$	$50^o - 90^o$
5	7.94	13.88	9.60	20.23	23.24	15.73	36.7	3.39	3.45	$90^o - 90^o$	$90^o - 90^o$	$70^o - 90^o$
6	8.56	13.52	8.07	18.27	22.61	13.45	8.52	3.10	3.47	$130^o - 90^o$	$130^o - 90^o$	$130^o - 90^o$
7	7.02	10.64	6.61	13.32	18.69	9.30	4.43	3.36	3.36	$50^o - 90^o$	$50^o - 90^o$	$130^o - 90^o$
8	8.97	12.76	9.18	18.63	22.03	14.8	7.62	2.47	3.23	$130^o - 90^o$	$130^o - 90^o$	$130^o - 110^o$
9	9.45	16.42	12.27	25.41	28.62	20.7	344.7	2.34	3.62	$90^o - 90^o$	$90^o - 90^o$	$90^o - 110^o$
10	7.96	12.74	9.12	20.90	23.47	13.75	226.1	3.13	4.67	$90^o - 90^o$	$90^o - 90^o$	$90^o - 110^o$
11	10.31	16.36	12.72	27.00	29.73	20.98	61.52	2.86	4.21	$90^o - 90^o$	$90^o - 90^o$	$90^o - 110^o$
12	6.73	11.28	7.16	13.95	18.82	9.56	6.54	3.17	3.26	$90^o - 90^o$	$90^o - 90^o$	$110^o - 90^o$
13	3.49	7.51	4.57	6.98	12.08	2.77	19.82	3.22	4.30	$90^o - 90^o$	$90^o - 90^o$	$70^o - 90^o$
14	3.54	8.45	6.95	6.41	13.67	11.11	6.28	4.38	4.12	$90^o - 90^o$	$110^o - 90^o$	$110^o - 90^o$
15	7.62	10.12	7.42	14.76	17.49	12.42	4.93	4.22	3.57	$50^o - 90^o$	$130^o - 90^o$	$50^o - 90^o$
16	6.96	11.62	8.91	12.66	19.23	13.85	3.70	3.21	3.36	$50^o - 90^o$	$50^o - 90^o$	$130^o - 90^o$
17	11.97	13.48	11.50	19.33	23.41	20.35	2.34	3.65	3.77	$50^o - 90^o$	$50^o - 90^o$	$50^o - 90^o$
18	11.37	13.13	9.22	18.32	22.79	14.89	2.27	3.56	3.17	$50^o - 90^o$	$50^o - 90^o$	$50^o - 90^o$

hand influence, along with the form factor and the MP component, provides the maximum level of realism for this MIMO simulator.

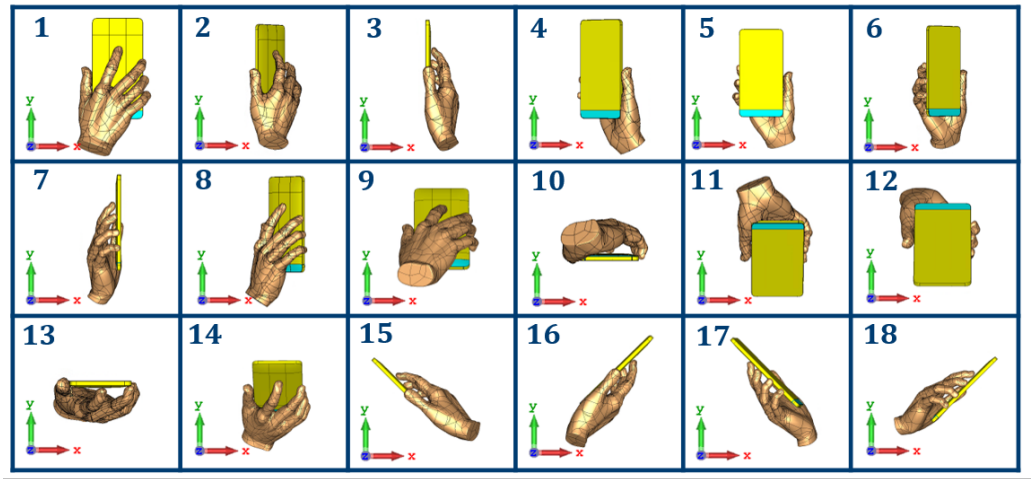

Figure 4.11: Identification of the 18 UE possible orientations in space.

This time, instead of using the usual Table form, the results will be displayed in a more intuitive way, using a CDF of the channel capacity over the 18 positions. Although it is clear that 18 positions are not enough to build a CDF, it still shows better the trend than tabular data displayed Table 4.4 or Table 4.5. This is an alternative that makes it easier to assess the influence of the phone's rotation in the channel's performance. Only the capacity will be represented since this

is the criteria with most meaning for assessing MIMO performance, while the others, although important for result interpretation, end up being redundant for channel performance evaluation.

Within the three environment scenarios created, SC1, SC2 and SC3, four test cases will be considered. The first two are the PBS arrays implemented in the form factor and the MBS implemented in the form factor. The second pair of test cases are similar to the first two but with the addition of a hand model in TM. The test cases will then be represented in the form of a channel capacity CDF in respect to the UE's 18 positions of rotation. Figure 4.12 displays the curves for the first environment scenario, SC1, while Figures 4.13 and 4.14 present, respectively, the curves for SC2 and SC3.

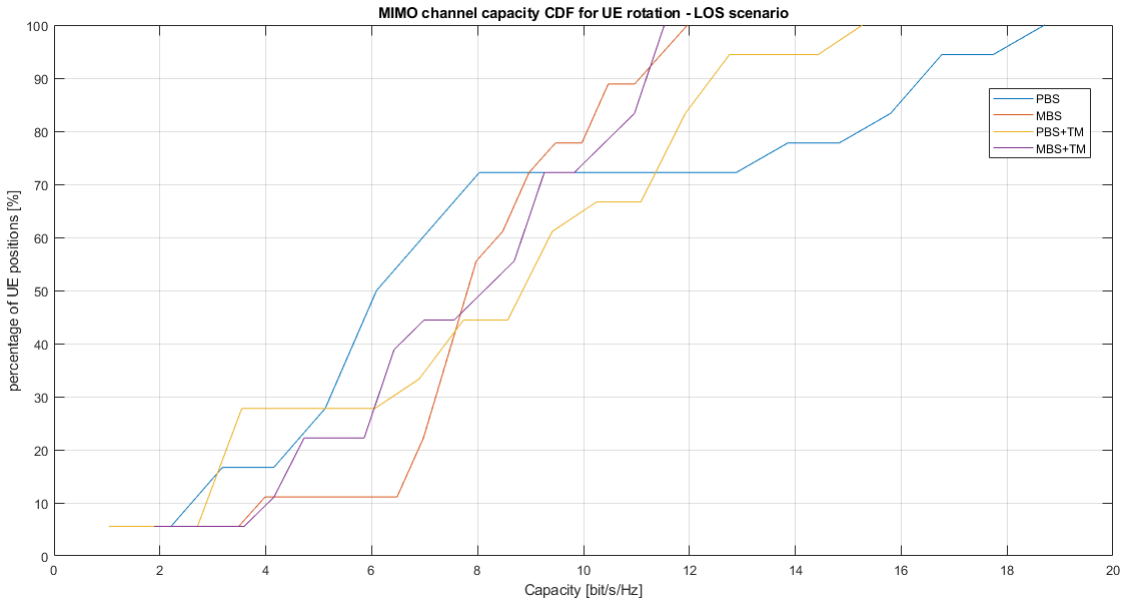

Figure 4.12: Capacity CDF for UE rotation in SC1 (LOS scenario) - PBS, MBS, PBS + TM and MBS + TM.

As previously referred, the median value of the capacity will be taken as a gross figure-of-merit of the channel performance, $C_{50\%}$. A high $C_{50\%}$ translates into a good channel performance, since it indicates the maximum capacity achievable among half of the UE positions available. Similarly, $C_{70\%}$ would be the maximum capacity value found when assessing 70% of the UE positions. Ultimately, $C_{100\%}$ would be the maximum channel capacity that can be accomplished within this particular environment scenario, for the specific transmitted power and distance conditions.

The effects of MP can be felt by comparing the average $C_{50\%}$ of the curves for each scenario. In SC1, that shows the results for LOS, the values of $C_{50\%}$ range between 6 bit/s/Hz and 9 bit/s/Hz. On the other hand, for SC2 and SC3, that comprise MP, this reference increases in value. For SC2, where LOS + MP is characterized, the $C_{50\%}$ values go from 9.5 bit/s/Hz to almost 12 bit/s/Hz. For SC3, with respect to NLOS with MP, the values are between 8 and 9.5 bit/s/Hz. This lower value is understandable, since, as mentioned before, the scatterers are further away. In fact, when comparing all three environment scenarios, a trend is evident regarding the overall channel capacity that can be described as $C_{SC1} < C_{SC3} < C_{SC2}$, regardless of the case study being considered. This reinforces the importance of MP to obtain a good MIMO channel performance.

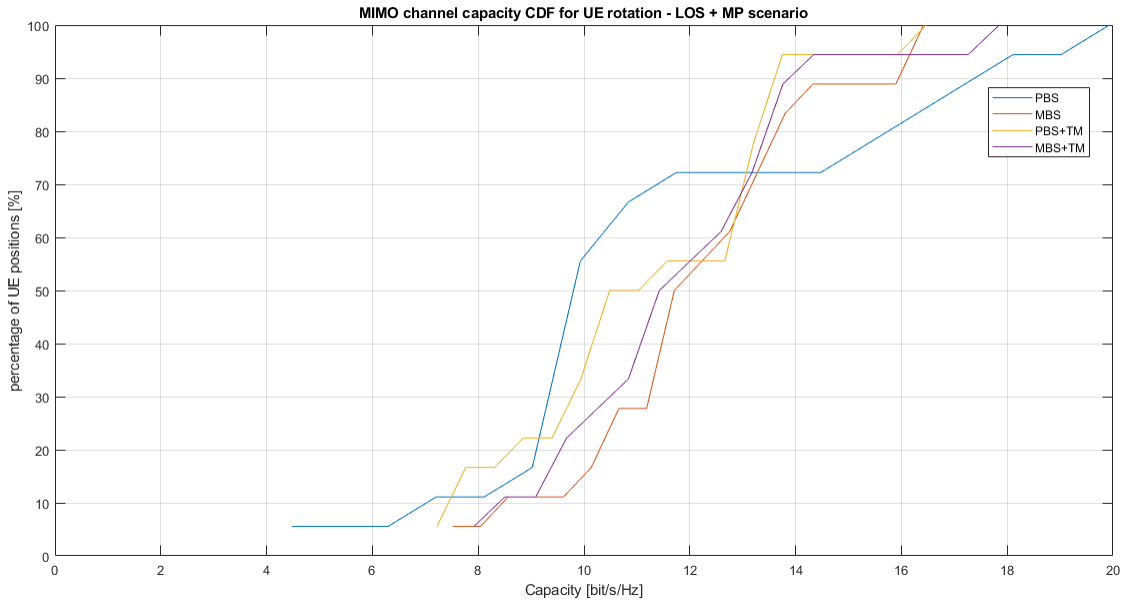

Figure 4.13: Capacity CDF for UE rotation in SC2 (LOS + MP scenario) - PBS, MBS, PBS + TM and MBS + TM.

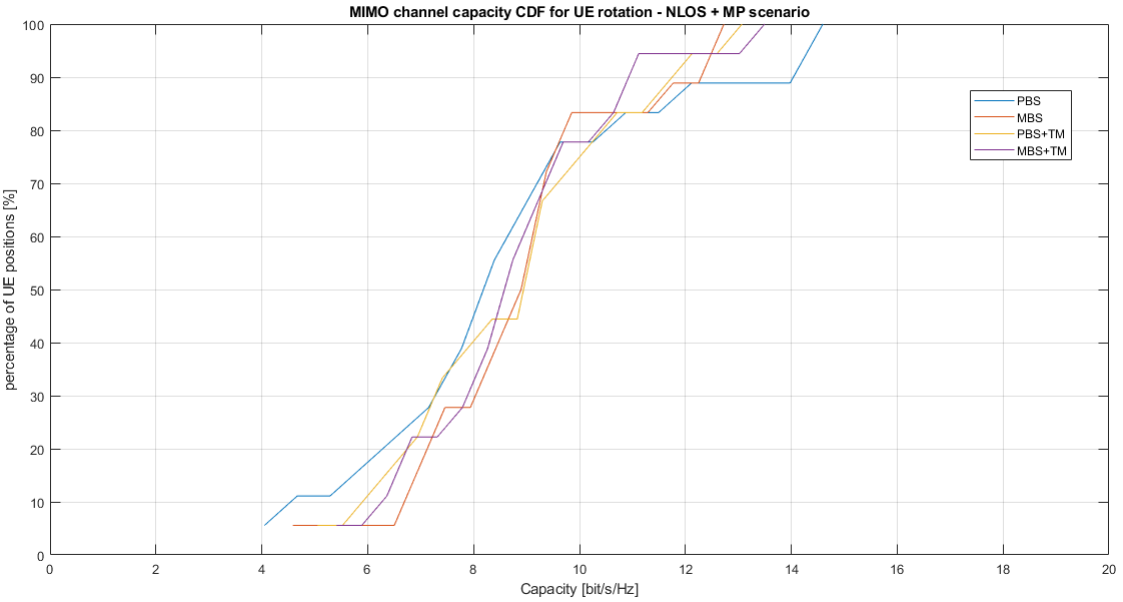

Figure 4.14: Capacity CDF for UE rotation in SC3 (NLOS + MP scenario) - PBS, MBS, PBS + TM and MBS + TM.

There is also a lot of information to be collected from comparing the four test case scenarios. These can be grouped into pairs for two categories of analysis, while still comparing PBS with MBS. In the first category, the antennas are implemented into the form factor and evaluated in free

space (corresponding to te blue and red curves, respectively). In the second category, the antennas are implemented within the form factor and there is also a form if body blockage, a hand in TM configuration (yellow curve belongs to the PBS and the purple curve to the MBS).

Using $C_{50\%}$ as a criteria, it is evident that, for free space, the MBS presents a better channel performance than the PBS. It is not a dramatic difference between the two but, considering that the MBS was expected to do poorly in a MIMO configuration, these results are a bit unexpected and exciting. Also something that is worth mentioning is the stability of the data rate provided by the PBS and the MBS. Although the PBS reaches higher channel capacity values than the MBS, it is not able to maintain that channel performance through all movements of rotation of the UE. Taking SC2 as an example (since all environment scenarios present the same channel behavior), represented in Figure 4.13, throughout all 18 UE positions, the PBS channel capacity varies from around 5 bit/s/Hz to 20 bit/s/Hz. The monopole, on the other hand, varies from around 8 bit/s/Hz to around 16 bit/s/Hz. This gives the MBS the upper hand that manifest in the CDF curves for the UE rotation, where the MBS has a clear advantage over the PBS.

Moving on to the adding the human body blockage, which is the most relevant and realistic set of test cases (because it represents the most frequent situation of mobile phone usage) it is difficult to assess the actual values of channel performance when compared to the free space test cases. This is simply because there are numerous ways that the user can hold the phone that would have more or less influence on the antennas' performance. A certain hand position might uncover the PBS antennas but cover the MBS and vice versa. The important thing to keep in mind is the tendency of the CDF curves, for a specific hand grip, when compared to each other. And, in fact, the introduction of the TM hand in the simulations causes the PBS and MBS CDF curves from Figure 4.12, Figure 4.13 and Figure 4.14 to come closer together, straightening the capacity gap seen between the PBS and MBS in free space. This corroborates even further the conclusions reached in the previous chapters regarding the CS. In fact, when all environment condition come to play, such as realistic radiation patterns, inclusion of the smartphone chassis, phone rotation, the user's body blockage and MP, there is not that much difference in channel performance using the PBS or the MBS. And, if that is the case, then the MBS antenna is a good alternative to the use of PBS for mm-Wave antenna smartphone implementation. The MBS presents itself as a smaller, less complex alternative to the PBS that is easier to produce and implement and offers similar gain coverage and MIMO channel performance as the PBS antenna.

It is important to mention that, ideally, the number of UE positions considered should be very high in order to recreate all the ways the user can place the phone. Due to simulation time contrictions, a compromise was established at 18 positions to cover the UE's full range of motion in space. This is noticeable in the slight curve jumps seen in the Figures above. Decreasing the rotation angle between consecutive UE positions from 45^o to, for example, 10^o, would raise the simulation time significantly but would also provide a lot more data for evaluation. This would lead to smoother and more representative CDF curves, despite the information displayed being essentially the same as what is presented now. This study is meant to portray the overall tendency of MIMO channel performance for each antenna type, so 18 position is a good enough number of positions to use. A more rigorous study, where the focus is placed on the actual capacity values would, in fact, require a higher number of positions for the UE.

4.4 Summary

This Chapter described the study conducted to quantify the antennas' influence on the MIMO channel performance. After several steps of result validation and different scenario simulations, some important findings should be emphasized:

- SISO vs. MIMO for MBS: the idea was for the MBS to operate with MIMO and, for high CN values, where MIMO is useless, switch to SISO. However, the LOS tests performed for each of the 18 UE positions revealed that there is no advantage in implementing SISO as a transmission technique, since for high CN values there is not much difference in channel capacity. MIMO will provide the best channel capacity and, in the worst case cenario, will deteriorate to values close to SISO.
- Channel sensitivity to phone rotation: the channel's capacity should be stable and independent of the phone's orientation. However this is not always possible because the phone's rotation and the presence of scatterers will alter the signal's polarization before reaching the BS. The antenna type that is less sensitive to these changes would be indicated to be used in 5G smartphones. The results for multiple test cenarios (LOS, LOS + MP and NLOS + MP) revealed that, with the MBS, despite the channel's maximum capacity being smaller, it is less volatile than with the PBS. However, when considering the hand grip mentioned in Chapter 2, once again, the PBS and MBS curves in the MIMO chanel capacity CDF for UE rotation become really close. This concludes that, in fact, there is no use in using an intricate antenna solution when, in the end, both the form factor and the user will alter the antennas behavior, making them unpredictable.

Chapter 5

Conclusions and future work

5.1 Conclusions

5G is the new wireless technology being currently developed as the successor of the soon to be strained 4G network. New tecnhnologies like HD streaming, augmented reality, mass patient monitoring and smart houses, along with the continuously increasing number of users and devices, require unprecedented values of data rate, bandwidth, and low latency that only 5G can provide. This new generation of wireless system will entail a concept drift regarding the design and implementation of millimeter wave antennas for 5G smartphones.

Therefore, this project aims to evaluate the implementation of mm-Wave antennas in 5G smartphones. In order to do so, it is key to identify the environment parameters that impact the antennas' performance and incorporate them into the antenna analysis in order to obtain the most realistic study possible.

An underlying goal for this project is also to establish a comparison process for mm-Wave antennas that can assess their potential and limitations when implemented in the smartphone, subjected to real life environment scenarios under 5G requirements. This process is used to consciously choose the type of antenna for 5G that best fits the implementation for that specific form factor, hand grip and environment parameters. The comparison is done through two fronts of antenna evaluation: CDF and a MIMO channel performance evaluation, using the PBS and the MBS antennas as a basis for comparison.

In the CDF, for each antenna type, a scan of the radiation pattern is conducted in all directions of observation. This radiation pattern is obtained from CST for free space, in a first analysis, implemented in the form factor, with or without the hand grip. In other words, any radiation pattern can be evaluated in terms of coverage. Using that information, the algorithm identifies the antenna type that provides the best gain distribution over space, while still maintaining a high enough gain value for communications. Using this process, the MBS and PBS's coverage percentage was compared for the scenario with smartphone implementation and hand grip.

In the MIMO channel performance evaluation, the MIMO's channel sensitivity is assessed according to 13 UE orientation positions, user body blockage and antenna depolarization, for each antenna type. In order to accomplish this, a channel simulator is created based on a geomet-

ric discrete scattering model, that, unlike the usual statistical channel models, recreates realistic channel conditions for any given input environment from real antenna characteristics and scatterer placement. The channel conditions obtained from the simulator are used to compute the channel performance metrics that allow to classify the quality of MIMO achieved with a certain antenna type, for the environment under study. For this study three environments were considered. The first one is a LOS scenario where the conditions of the environment are static in time. The second presents a LOS scenario with MP, where scatterers are placed randomly within a confined within an area of interest between the UE and the BS. And, at last, the third scenario describes a NLOS with MP scenario, where the line-of-sight scatterers are blocked by a big obstacle and the MIMO channel performance relies on further placed scatterers. The tests were performed for the PBS and MBS implemented in the form factor and, in a second stage, also with a common hand grip model covering the antennas.

These studies led to very interesting and surprising conclusions that contribute for a deeper understanding of not only the limitations of using mm-Wave arrays in smartphone implementations but also the advantages of doing so.

This study showed the deep implications that the mobile phone's metallic chassis has on the performance of the antennas. Not only does it affect the shape of their radiation pattern, but also deteriorates their coupling values, according to where the antennas are located. The proximity to metal is not beneficial especially for mm-Wave antennas, since it causes the electromagnetic field to propagate in a different direction (that is not obstructed with metal), which results in the altered radiation pattern shape. Therefore, antenna placement is of utmost importance to minimize the antennas' exposure to the metal components of the phone, preserving their performance as much as possible. The CDF for the antennas implemented in the form factor revealed that the PBS, despite having a higher gain value, has an overall lower coverage percentage than the MBS that has a wider radiation pattern.

Similarly, at mm-Wave the user behaves as a big obstacle to the antenna's radiation pattern. This is explained by the dielectric properties of the human body for such high frequencies. Whatever part of the electromagnetic field that is not reflect by the body's surface is quickly absorbed at the level of the epidermis. This results in the complete distortion of the radiation patterns, to a point where the BF ability is lost and the antennas' radiation efficiency is affected. In order to avoid this, it is crucial to have a redundant number of strategically placed MIMO antenna arrays that can take over the communications whenever the user is unvoluntarily blocking one of the other arrays. Moreover, when the hand grip is taken into consideration in the CDF of the PBS vs. the MBS, the small difference between the antennas' coverage curves fades away, which shows that, when the user is involved, there is no use in having too complicated antennas, since everything will be ruined by its grip anyways.

It was verified that, for mm-Wave frequencies, the path loss experience by the signal is, in fact, extremely high. A small increase in distance causes a steep drop in the the data rate values of the MIMO channel. In this project, the power supplied to the phone was considered to be constant so the only way to fix this would be to use, instead of single antenas, antenna arrays with an adequate number of antennas. Too few antennas would not provide high enough gain and too many antennas in the array would be too complex and energy consuming. An alternative approach would be to just boost the power of the mobile phone, so that the signal has enough strength to propagate further in space.

It was also confirmed that the presence of obstacles in the environment resulted in an increased MIMO channel performance. From the three environments tested, the one that presented the highest data rate values was the SC2, LOS + MP, followed by SC3, NLOS + MP, and finally SC1, LOS. This is because MIMO strives in MP rich environments, since there are multiple paths created for the signals to propagate through.

Also, when considering the MIMO channel performance evaluation, the orthogonal arrays strategy is, after all, not as good as claimed in the literature. Despite being able to be implemented as a dual polarized antenna, thus proving themselves to be a space efficient solution, the orthogonal arrays do not double the spectral efficiency for all orientations of the mobile phone. It is true that, for an ideal orientation where the UE is perfectly aligned with the BS, or suffers a rotation of 90^o, this approach is unbeatable. However this orientation is not an accurate depiction of the usual position of the UE in real life, since the user is constantly moving and positioning it differently. Once the phone rotates away from the BS, which happens often, none of the UE polarizations are aligned with the BS and the orthogonal arrays do not offer any advantages. This was one of the main arguments for the use of PBS for antenna implementation in 5G smartphones, that is now weakened using this project's MIMO performance study. The MBS arrays, on the other hand, are implemented in the smartphone with the same orientation, due to space constrictions. And, against all odds, they provide a more stable data rate throughout the 13 UE positions than the PBS, although at the cost of a slightly worst maximum channel capacity value. However, as to be expected by now, when the effects of the hand grip come into play, the performance of the antennas is equally affected and the results of the PBS become closer to the ones from the MBS.

In conclusion, the two stage comparison process between the PBS and MBS reveals that, despite the MBS being the winner, they are actually quite similar when it comes to gain coverage and MIMO channel performance. It was discussed already that the MBS is a smaller, easier to implement, less complex and cheaper solution when compared to the PBS.

The Occam's razor is a principle of problem solving that states that the correct answer tends to the the simplest one. In that sense, between the PBS and MBS, the MBS seems to be the answer to the problem of mm-Wave antenna implementation in 5G smartphones.

5.2 Future Work

This section is dedicated to presenting the next steps idealized for the thesis that were left unexplored due to a lack of time, resources or merely because they were out of the scope of the thesis. Overall, this thesis accomplished what it set out to investigate. A comparison process was successfully established and an antenna solution was deemed the winner for smartphone implementation regarding gain coverage and MIMO channel performance.

However, having experimental results would provide some added value to the project's conclusions, since it would further validate the results obtained. Therefore, initially, the PBS and MBS antenna arrays would have to be produced with its digital phasing circuit, integrated to a real smartphone and measured in an anechoic chamber, both with and without the user's a gripping hand phantom, in order to compare the measured radiation patterns with the simulated ones. The mobile phone and the hand phantom would then be used in real life measurements in a MIMO performance setting.

One of the next steps would be to implement in the simulator the possibility of adopting more than one frequency. This project was conducted for a single value of frequency, 39 GHz, but a transmission is usually performed over a certain bandwidth. Also, some additional features could be included in the MIMO simulator such as, for example, implementing more arrays along the UE (so that the effects of beam/array switching would be more pronounced) and number of equally distributed BS over space, instead of having just one.

Other than that, an interesting approach that was not pursued was the implementation of the rest of the MIMO system in the project's channel simulator. Currently, the simulator addresses the link level MIMO performance, which provides a good estimate of the overall MIMO system performance. However, the platform is prepared to be integrated as a part of a system level simulator that would include coding, modulation and channel estimation modules for an even more accurate MIMO performance evaluation. For the LOS scenario, SC1, the measurement anechoic chamber would be appropriate since it would replicate well a steady environment with no variation over time. For LOS + MP and NLOS + MP, respectively SC2 and SC3, any busy area of town would do, except for the fact that, for SC3, a big building or obstacle must block the direct path between the UE and the BS.

Annex A

Array coupling evaluation

As previously mentioned, the array coupling matrix is dependent on the beam chosen by each array of the UE. There are two arrays implemented in the UE for the MIMO channel performance study and the coupling values for each beam combination were computed in CST.

Since the PBS is a dual polarized array, the coupling values between the arrays were similar. The representative case of $\psi_{UE_{A1}=90^0}$-$\psi_{UE_{A2}=90^0}$ was chosen to reveal a coupling matrix presented in Equation 5.1.

$$\left[S_{PBS|90^o-90^o}\right] = \begin{bmatrix} -23.97 & -11.035 \\ -11.35 & -11.035 \end{bmatrix} dB \tag{5.1}$$

For the MBS, since the two arrays were placed side by side in the form factors dielectric, the worst case of coupling would be for the beams from the two arrays are pointing at each other. The first array from the UE is placed on the right side of the back of the phone an the second array on the left. Therefore, the coupling should be maximum for $\psi_{UE_{A1}=50^0}$-$\psi_{UE_{A2}=130^0}$. This leads to a coupling matrix displayed in Equation 5.2.

$$\left[S_{MBS|130^o-50^o}\right] = \begin{bmatrix} -11.35 & -36.15 \\ -36.15 & -15.17 \end{bmatrix} dB \tag{5.2}$$

Both these coupling matrices will lead to transmission T matrices where the diagonal entries are close to one and the rest close to 0, as can be seen by Equation 5.3 and Equation 5.4. This means that both signal get transmitted independently and, therefore, the transmission matrix for this particular antenna configuration and placement in the mobile phone won't affect the MIMO channel performance results.

$$\left[T_{PBS|90^o-90^o}\right] = \begin{bmatrix} 0.9980 & 0.2807 \\ 0.2807 & 0.9598 \end{bmatrix} \tag{5.3}$$

$$\left[T_{MBS|130^o-50^o}\right] = \begin{bmatrix} 0.9627 & 0.0156 \\ 0.0156 & 0.99 \end{bmatrix} \tag{5.4}$$

Bibliography

[1] Wonbin Hong. Solving the 5G Mobile Antenna Puzzle. *IEEE Microwave Magazine*, 18(7):86 – 102, 2017.

[2] Heejung Yu, Howon Lee, and Hongbeom Jeon. What is 5G? Emerging 5G mobile services and network requirements. *Sustainability (Switzerland)*, 9(10):1–22, 2017.

[3] Simon Svendsen and Ole Jagielski. Dual Resonance Self-Matched Indirect Fed Antenna Array for 5G. Technical report, INTEL, 2017.

[4] Global mobile Suppliers Association. The Road to 5G: Drivers, Applications, Requirements and Technical Development. Technical report, Global mobile Suppliers Association (GSA), 2015.

[5] Huawei White Paper. 5G New Air Interface and Radio Access Virtualization. Technical Report April, 2015.

[6] J.G. Jeffrey G. Andrews, Stefano Buzzi, Wan Choi, Stephen V. S.V. Hanly, Angel Lozano, A.C.K. Anthony C K Soong, and J.C. Jianzhong Charlie Zhang. What will 5G be? *IEEE Journal on Selected Areas in Communications*, 32(6):1065–1082, 2014.

[7] Huawei. 5G : A Technology Vision. Technical report, Huawei, 2014.

[8] Qualcomm Technologies. Spectrum for 4G and 5G. Technical report, Qualcom, 2017.

[9] Electronic Communications Committee (ECC) within the European Conference of Postal (CEPT), Telecommunications Administrations, and THE. The European Table of Frequency Allocations and Applications in the frequency in the frequency range 8 . 3 kHz to 3000 GHz (ECA Table). Technical Report October, 2017.

[10] L I Lianming, N I U Xiaokang, Chai Yuan, Chen Linhui, Zhang Tao, and Cheng Depeng. The path to 5G : mmWave aspects. *Journal of Communications and Information Networks*, 1(2):1–18, 2016.

[11] Theodore S. Rappaport, Shu Sun, Rimma Mayzus, Hang Zhao, Yaniv Azar, Kevin Wang, George N. Wong, Jocelyn K. Schulz, Mathew Samimi, and Felix Gutierrez. Millimeter wave mobile communications for 5G cellular: It will work! *IEEE Access*, 1:335–349, 2013.

[12] Elias Yaacoub, Mohammed Husseini, and Hassan Ghaziri. An overview of research topics and challenges for 5G massive MIMO antennas. *2016 IEEE Middle East Conference on Antennas and Propagation, MECAP 2016*, 2016.

[13] Schulz Schindler. Introduction to MIMO Application Note. Technical report, Rohde & Schwarz, 2009.

[14] Federico Boccardi, Robert Heath, Angel Lozano, Thomas L. Marzetta, and Petar Popovski. Five disruptive technology directions for 5G. *IEEE Communications Magazine*, 52(2):74–80, 2014.

[15] Shu Sun, Theodore S. Rappaport, Robert W. Heath, Andrew Nix, and Sundeep Rangan. MIMO for millimeter-wave wireless communications: Beamforming, spatial multiplexing, or both? *IEEE Communications Magazine*, 52(12):110–121, 2014.

[16] Wonil Roh, Ji Yun Seol, Jeong Ho Park, Byunghwan Lee, Jaekon Lee, Yungsoo Kim, Jaeweon Cho, Kyungwhoon Cheun, and Farshid Aryanfar. Millimeter-wave beamforming as an enabling technology for 5G cellular communications: Theoretical feasibility and prototype results. *IEEE Communications Magazine*, 52(2):106–113, 2014.

[17] Andy Sutton. 5G network architecture. Technical report, Huawei, 2018.

[18] Huawei. 5G Spectrum. Technical report, Huawei.

[19] Cisco. Cisco Visual Networking Index: Global Mobile Data Traffic Forecast Update, 2011–2016 [Visual Networking Index (VNI)]. Technical report, 2017.

[20] Wonbin Hong, Senior Member, Kwang-hyun Baek, Seungtae Ko, and Invited Paper. Millimeter-Wave 5G Antennas for Smartphones : Overview and Experimental Demonstration. *IEEE Transactions on Antennas and Propagation*, 65(12):6250–6261, 2017.

[21] Wonbin Hong, Kwanghun Baek, Youngju Lee, and Yoon Geon Kim. Design and analysis of a low-profile 28 GHz beam steering antenna solution for Future 5G cellular applications. In *IEEE MTT-S International Microwave Symposium Digest*, 2014.

[22] Yiming Huo, Xiaodai Dong, and Wei Xu. 5G Cellular User Equipment: From Theory to Practical Hardware Design. *IEEE Access*, 5:13992 – 14010, 2017.

[23] Ohyun Jo, Jung Ju Kim, Jungmin Yoon, Dooseok Choi, and Wonbin Hong. Exploitation of Dual-Polarization Diversity for 5G Millimeter-Wave MIMO Beamforming Systems. *IEEE Transactions on Antennas and Propagation*, 65(12):6646–6655, 2017.

[24] Wonbin Hong, Kwang Hyun Baek, Youngju Lee, Yoongeon Kim, and Seung Tae Ko. Study and prototyping of practically large-scale mmWave antenna systems for 5G cellular devices. *IEEE Communications Magazine*, 52(9):63 – 69, 2014.

[25] Vinko Erceg, Hemanth Sampath, and Severine Catreux-Erceg. Dual-polarization versus single-polarization MIMO channel measurement results and modeling. *IEEE Transactions on Wireless Communications*, 5(1):28–33, 2006.

[26] Bin Yu, Kang Yang, Chow-yen-desmond Sim, and Guangli Yang. Communication With Metallic Casing Application. *IEEE Transactions on Antennas and Propagation*, 66(1):462–466, 2018.

[27] Manoj Stanley, Manoj Stanley, Yi Huang, Tian Loh, Qian Xu, Hanyang Wang, and Hai Zhou. A High Gain Steerable Millimeter-Wave Antenna Array for 5G Smartphone Applications A High Gain Steerable Millimeter-Wave Antenna Array for 5G Smartphone Applications. *2017 11th European Conference on Antennas and Propagation (EUCAP)*, 2017.

[28] Kun Zhao, Jakob Helander, Daniel Sjöberg, Sailing He, Thomas Bolin, and Zhinong Ying. User Body Effect on Phased Array in User Equipment for the 5G mmWave Communication System. *IEEE Antennas and Wireless Propagation Letters*, 16:864–867, 2017.

[29] Ting Wu and Christopher M. Rappaport, Theodore S., Collins. Safe for Generations to Come. *IEEE Microwave Magazine*, 16(2):65–84, 2015.

[30] M.A. Jensen and J.W. Wallace. MIMO wireless channel modeling and experimental characterization. In A. B. Gershman N. D. Sidiropoulos, editor, *Space-Time Processing for MIMO Communications*, chapter 1, pages 1–35. John Wiley & Sons, Ltd, 1 edition, 2005.

[31] Yaniv Azar, George N. Wong, Kevin Wang, Rimma Mayzus, Jocelyn K. Schulz, Hang Zhao, Felix Gutierrez, Duckdong Hwang, and Theodore S. Rappaport. 28 GHz propagation measurements for outdoor cellular communications using steerable beam antennas in New York city. *IEEE International Conference on Communications*, pages 5143–5147, 2013.

[32] University of Southern California Aalto University, BUPT,CMCC, Ericson, Huawei, INTEL, KT Corporation, Nokia, NTT DOCOMO, Qualcomm, Samsung, University of Bristol. 5G Channel Model for bands up to 100 GHz. Technical Report May, 2016.

[33] Katsuyuki Haneda, Jianhua Zhang, Lei Tan, Guangyi Liu, Yi Zheng, Henrik Asplund, Jian Li, Yi Wang, David Steer, Clara Li, Tommaso Balercia, Sunguk Lee, Youngsuk Kim, Amitava Ghosh, Timothy Thomas, Takehiro Nakamura, Yuichi Kakishima, Tetsuro Imai, Haralabos Papadopoulos, Theodore S. Rappaport, George R. Maccartney, Mathew K. Samimi, Shu Sun, Ozge Koymen, Sooyoung Hur, Jeongho Park, Charlie Zhang, Evangelos Mellios, Andreas F. Molisch, Saeed S. Ghassamzadeh, and Arun Ghosh. 5G 3GPP-like channel models for outdoor urban microcellular and macrocellular environments. *IEEE Vehicular Technology Conference*, 2016-July, 2016.

[34] ETSI. TR 138 901 - V14.0.0 - 5G; Study on channel model for frequencies from 0.5 to 100 GHz (3GPP TR 38.901 version 14.0.0 Release 14). Technical report, ETSI, 2018.

[35] C S T Microwave Studio. CST MWS Workflow and Solver Overview. Technical report, CST, 2010.

[36] Corning. Corning Gorilla Glass 5 PI Sheet. Technical report, Corning, 2016.

[37] D.Andreuccettia and R.Fossi. Dielectric Properties of Body Tissues in the frequency range 10 Hz - 100 GHz. http://niremf.ifac.cnr.it/tissprop/.

[38] Junyi Wang, Zhou Lan, Chin Sean Sum, Chang Woo Pyo, Jing Gao, Tuncer Baykas, Azizur Rahman, Ryuhei Funada, Fumihide Kojima, Ismail Lakkis, Hiroshi Harada, and Shuzo Kato. Beamforming codebook design and performance evaluation for 60GHz wideband WPANs. *IEEE Vehicular Technology Conference*, pages 0–5, 2009.

[39] Constantine A. Balanis. *Antenna Theory Analysis and Design*. John Wiley & Sons, Ltd, third edition, 2005.

[40] Keysight Technologies. MIMO Performance and Condition Number in LTE Test. http://literature.cdn.keysight.com/litweb/pdf/5990-4759EN.pdf, 2014.

[41] Stefan Schindler and Heinz Mellein. Assessing a MIMO Channel. Technical report, Rhode&Schwarz, 2011.

[42] Kevin Faison. Understanding noise figures in radio receivers. https://www.eetimes.com/document.asp?doc_id=1272302.